The Astrophysical Journal, 832:12 (39pp), 2016 November 20 doi:10.3847/0004-637X/832/1/12

ANALYSIS OF THE *HERSCHEL*/HEXOS SPECTRAL SURVEY TOWARD ORION SOUTH: A MASSIVE PROTOSTELLAR ENVELOPE WITH STRONG EXTERNAL IRRADIATION

K. Tahani[1], R. Plume[1], E. A. Bergin[2], V. Tolls[3], T. G. Phillips[4], E. Caux[5,6], S. Cabrit[7], J. R. Goicoechea[8], P. F. Goldsmith[9], D. Johnstone[10], D. C. Lis[4,7], L. Pagani[7], K. M. Menten[11], H. S. P. Müller[12], V. Ossenkopf-Okada[12], J. C. Pearson[9], and F. F. S. van der Tak[13,14]

[1] Department of Physics & Astronomy, University of Calgary, Calgary, AB T2N 1N4, Canada; ktahani@ucalgary.ca
[2] Department of Astronomy, University of Michigan, 500 Church Street, Ann Arbor, MI 48109, USA
[3] Harvard-Smithsonian Center for Astrophysics, 60 Garden Street, Cambridge, MA 02138, USA
[4] California Institute of Technology, Cahill Center for Astronomy and Astrophysics 301-17, Pasadena, CA 91125, USA
[5] Université de Toulouse, UPS-OMP, IRAP, F-31028 Toulouse, France
[6] CNRS, IRAP, 9 Av. Colonel Roche, BP 44346, F-31028 Toulouse Cedex 4, France
[7] LERMA, Observatoire de Paris, PSL Research University, CNRS, Sorbonne Universités, UPMC Univ. Paris 06, F-75014, Paris, France
[8] Instituto de Ciencia de Materiales de Madrid (ICMM-CSIC). Sor Juana Ines de la Cruz 3, E-28049 Cantoblanco, Madrid, Spain
[9] Jet Propulsion Laboratory, Caltech, Pasadena, CA 91109, USA
[10] National Research Council Canada, Herzberg Institute of Astrophysics, 5071 West Saanich Road, Victoria, BC V9E 2E7, Canada
[11] Max-Planck-Institut für Radioastronomie, Auf dem Hügel 69, D-53121 Bonn, Germany
[12] I. Physikalisches Institut, Universität zu Köln, Zülpicher Strasse 77, D-50937 Köln, Germany
[13] SRON Netherlands Institute for Space Research, P.O. Box 800, 9700 AV, Groningen, The Netherlands
[14] Kapteyn Astronomical Institute, Groningen, The Netherlands
Received 2016 May 30; revised 2016 August 8; accepted 2016 August 16; published 2016 November 11

ABSTRACT

We present results from a comprehensive submillimeter spectral survey toward the source Orion South, based on data obtained with the Heterodyne Instrument for the Far-Infrared instrument on board the *Herschel Space Observatory*, covering the frequency range of 480 to 1900 GHz. We detect 685 spectral lines with signal-to-noise ratios (S/Ns) $> 3\sigma$, originating from 52 different molecular and atomic species. We model each of the detected species assuming conditions of Local Thermodynamic Equilibrium. This analysis provides an estimate of the physical conditions of Orion South (column density, temperature, source size, and $V_{\rm LSR}$). We find evidence for three different cloud components: a cool ($T_{\rm ex} \sim 20$–40 K), spatially extended ($>60''$), and quiescent ($\Delta V_{\rm FWHM} \sim 4$ km s^{-1}) component; a warmer ($T_{\rm ex} \sim 80$–100 K), less spatially extended ($\sim 30''$), and dynamic ($\Delta V_{\rm FWHM} \sim 8$ km s^{-1}) component, which is likely affected by embedded outflows; and a kinematically distinct region ($T_{\rm ex} > 100$ K; $V_{\rm LSR} \sim 8$ km s^{-1}), dominated by emission from species that trace ultraviolet irradiation, likely at the surface of the cloud. We find little evidence for the existence of a chemically distinct "hot-core" component, likely due to the small filling factor of the hot core or hot cores within the *Herschel* beam. We find that the chemical composition of the gas in the cooler, quiescent component of Orion South more closely resembles that of the quiescent ridge in Orion-KL. The gas in the warmer, dynamic component, however, more closely resembles that of the Compact Ridge and Plateau regions of Orion-KL, suggesting that higher temperatures and shocks also have an influence on the overall chemistry of Orion South.

Key words: ISM: abundances – ISM: individual objects (Orion South) – ISM: kinematics and dynamics – ISM: lines and bands – ISM: molecules

1. INTRODUCTION

To date, about 200 different molecular species have been detected in the interstellar medium (Menten & Wyrowski 2011).[15] However, our understanding of the total molecular inventory of individual sources is poor, since few sources have been systematically surveyed in any frequency band due to the large amount of observing time required to perform unbiased spectral surveys (e.g., Blake et al. 1987; Schilke et al. 1997a, 2001; Nummelin et al. 1998; Comito et al. 2005; Furlan et al. 2006; Tercero et al. 2010; Neill et al. 2014). Therefore, we do not truly understand the origin of the chemical complexity observed in interstellar space. Understanding this complexity is important to comprehend details of the formation of stars, planets, and life.

Regardless of how complex chemistry arises in interstellar space, the chemical composition (and subsequent chemical evolution) can, in turn, affect the physical conditions (and subsequent dynamical evolution) of a star-forming region (e.g., see Garrod & Herbst 2006; Garrod et al. 2008; Herbst & van Dishoeck 2009). For example, the overall molecular (and to some degree atomic) content can play an important role in regulating the gas pressure by changing the temperature of the gas via the process of heating and cooling through line-absorption and emission (Goldsmith & Langer 1978; Ceccarelli et al. 1996). In addition, molecular ions can affect the strength of coupling between the gas and the magnetic fields (which is related to magnetic turbulent support, e.g., Williams et al. 1998). Thus, there is a complex feedback between the physical and chemical conditions in an interstellar gas cloud that either helps drive the star-formation process, or hinders it, and which may help determine the masses of the newly formed stars.

In order to understand the origin of chemical complexity in interstellar space and how this chemistry evolves and affects the process of star formation in the universe (as well as the formation of planets and pre-biotic chemical species), we

[15] Also see http://www.astro.uni-koeln.de/cdms/molecules and http://www.astrochymist.org/astrochymist_ism.html.

require unbiased and complete surveys of spectral lines that span a broad range of wavelengths. These types of data sets are needed so that we can sample a wide variety of molecular and atomic species, as well as obtain multiple emission lines from each of the species, in order to extract the physical conditions in the gas. Fortunately, with the advent of sensitive, high-resolution spectrometers for millimeter/submillimeter wavelengths, especially those developed for space-based observatories, it is now possible to obtain such surveys and to begin to address these issues (e.g., Zernickel et al. 2012; Kama et al. 2013; Crockett et al. 2014; Kaźmierczak-Barthel et al. 2015).

The key project *Herschel* observations of EXtraOrdinary Sources (HEXOS; Bergin et al. 2010) was designed to address issues related to the chemical composition of massive star-forming regions. HEXOS has obtained spectral line surveys of the Orion-KL, Orion South (hereafter Orion-S), and Orion Bar (Z. Nagy et al. 2016, in preparation) regions within the Orion A Molecular Cloud, at high frequencies that are not easily accessible from ground-based observatories (480–1900 GHz). Both Orion-KL and Orion-S are relatively nearby (420 pc; Menten et al. 2007) massive star-forming regions close to the Orion Nebula. The nearby Trapezium OB stars are the source of high energy photons, which produce Photon Dominated Regions (PDRs) throughout the region. The UV flux ($6 < E < 13.6$ eV) in the vicinity of Orion-S is $\chi = 1.1 \times 10^5 \chi_0$ (Herrmann et al. 1997; Goicoechea et al. 2015), where $\chi_0 = 2.7 \times 10^{-4}$ erg s^{-1} cm^{-2} sr^{-1} (Draine & Bertoldi 1996). Observations of Goicoechea et al. (2015) and O'Dell & Harris (2010) suggest that the H II region lies mostly in front of the molecular material, but may wrap behind, at least part of, the Orion-S molecular cloud. Thus at least some of the Orion-S molecular gas is located in front of ionized material has been convincingly demonstrated by Very Large Array absorption measurements of the H_2CO 6 cm 1_{10}–1_{11} transition (Mangum et al. 1993).

Despite the fact that the far-infrared luminosity of Orion-S ($8.5 \times 10^3\ L_\odot$; Mezger et al. 1990) is more than an order of magnitude below that of KL, a number of energetic outflows associated with Orion-S suggest ongoing star formation. For example, CO $J = 2$–1 SMA observations (Zapata et al. 2005) revealed a highly collimated bipolar outflow extending ~30″ over the velocity range ~−80 to ~−26 km s^{-1} and ~22 to ~82 km s^{-1} oriented NW–SE. The submillimeter continuum source with a deconvolved size ⩽0.″6 and an integrated flux of 116.2 ± 9.0 mJy at 1.3 mm is well centered on the bipolar outflow axis, $\alpha_{2000} = 05^h35^m13\overset{s}{.}550$, $\delta_{2000} = -05°23'59\overset{''}{.}14$. In addition, another quite extended, collimated, low-velocity (5 km s^{-1}) CO outflow has been observed, oriented NE–SW (Schmid-Burgk et al. 1990), and a low-velocity (10 km s^{-1}) bipolar SiO (5–4) outflow with a length of ~30″ (oriented NE–SW) has been reported by Ziurys et al. (1990). Four other SiO outflows are also listed by Zapata et al. (2006).

Despite the presence of star-formation activity, as indicated by the IR luminosity and molecular outflows, BIMA observations of a few selected species by McMullin et al. (1993) suggest that the chemistry of Orion-S resembles that of the Orion-KL quiescent ridge and has fewer, narrower, and weaker lines than KL. These observations may imply that Orion-S is a more quiescent and younger star-forming region in which the star formation activity has not had time to significantly alter the dynamics and chemistry of the region. This idea is also consistent with dynamical ages from outflow observations in Orion-S (i.e., Schmid-Burgk et al. 1990; Bally et al. 2000; Zapata et al. 2005). Assuming no projection effects, the maximum corresponding dynamical age for the largest outflow is found to be less than 45,000 years, which is still remarkably young (Schmid-Burgk et al. 1990). The dynamical age for all the other outflows can be shown to be less than 5000 years (Bally et al. 2000; Zapata et al. 2005). A more detailed comparison between Orion-S and Orion-KL is, therefore, of great interest, since the two regions presumably formed under similar conditions, but could have very different chemical abundances, possibly based on differences in their ages, densities, temperatures, radiation fields, etc.

In this paper, we present a comprehensive study of the *Herschel*/Heterodyne Instrument for the Far-Infrared (HIFI) spectral survey toward Orion-S. The observations presented here were obtained as part of HEXOS and span over 1.2 THz of frequencies, mostly not accessible from the ground. In Section 2, we present our observations and data reduction methods, including the removal of off-position contamination, line identification, and Gaussian fitting of the spectral features. Our results (including LTE modeling of each individual species) together with a chemical comparison of Orion-S are presented in Section 3. The conclusions are provided in Section 4.

2. OBSERVATIONS AND DATA REDUCTION

The data presented in this paper were taken with HIFI (de Graauw et al. 2010), one of three instruments on board the *Herschel Space Observatory* (Pilbratt et al. 2010). HIFI operated over the frequency range of 480–1900 GHz (with two gaps: one at 1280–1430 GHz, due to the switch between SIS and HEB detectors (Roelfsema et al. 2012), and one at 1540–1570 GHz, which was an observational time saving strategy since this frequency range was expected to have few transitions). HIFI was separated into 14 different bands (1a, 1b, ..., 7b). Each receiver band had independent channels for horizontal (H) and vertical (V) polarizations, each with its dedicated Wide Band Spectrometer (WBS) having a native spectral resolution of 1.1 MHz (Roelfsema et al. 2012). Bands 1–5 were observed with an LO redundancy of 6, whereas Bands 6 and 7 used a redundancy of 2. Redundancy refers to the number of observations of each sky frequency with different LO settings. For example, a redundancy of 6 means that each frequency in the band was observed with 6 different LO settings. This redundancy was necessary in order to distinguish lines originating from the upper and the lower sidebands (Comito & Schilke 2002). A redundancy of 2 was sufficient for bands 6 and 7 due to the relatively lower density of transitions at these high frequencies. The central position of Orion-S was $\alpha_{2000} = 5^h35^m13\overset{s}{.}44$, $\delta_{2000} = -5°24'08\overset{''}{.}1$. All observations were taken in Dual Beam Switch (DBS) mode using the Fast Chop option (>0.5 Hz chop frequency).

We used the hifiPipeline task in HIPE 9.0 for all data reduction. The hifiPipeline task is a pre-compiled script in HIPE used to process level 0 data to any higher level (e.g., 0.5, 1.0, etc.). See Ott (2010) for a description of the various data products. Spurious spectral features were removed and fully calibrated, double side band (DSB) spectra were deconvolved into single side band spectra (e.g., level 2.5). Additional details on data reduction and observational parameters can be found in Bergin et al. (2010) and Crockett et al. (2010). After processing by HIPE 9.0, the H and V polarizations were co-added (except

Table 1
Data Smoothing and Noise Characteristics

	Smoothing Channels	Freq. Res. (MHz)	Vel. Res. (km s^{-1})	T_{sys} (K)	1σ rms (K)
Band 1	2	2.2	1.0–1.4	~100	~0.02–0.05
Band 2	4	4.4	1.6–2.1	~150	~0.03–0.07
Band 3	4	4.4	1.4–1.7	~200	~0.04–0.09
Band 4	8	8.8	2.4–2.8	~400	~0.1–0.2
Band 5	8	8.8	2.1–2.4	~1000	~0.1–0.3
Band 6	16	17.6	3.1–3.7	~1300	~0.3–2.0
Band 7	16	17.6	2.8–3.1	~1300	~0.4–4.0

for Band 4a, which, due to processing errors specific to this band, had much noisier V polarization data that were excluded) and then the spectra were Hanning smoothed by 2 to 16 channels (see Table 1) to improve the signal-to-noise ratio. Results are provided in Table 1, which shows typical values for the 1σ rms noise, system temperature, velocity, and frequency resolutions after smoothing, and the number of channels smoothed for each band. The 1σ rms noise is calculated from line-free regions of the spectrum immediately adjacent to the lines. A noise range is provided since the noise is not uniform across the bands.

All of the data in this paper are presented on the T_A temperature scale and, for subsequent analyses, were converted to T_{mb} using the main beam efficiencies in Müeller et al. (2014).[16] The final data after deconvolution and spectral smoothing (bands 1a–7b) are shown in Figures 1–4, in which the T_A range is in Kelvin and frequency is in MHz. The strongest lines are labeled in each band, and in order to make the residual noise recognizable and comparable from one band to another the intensity is fixed to 15 K for all bands. Note that certain broad features, like the one near 790 GHz, are most likely due to excess noise, since individual observations show quite a few noise spikes in these spectral ranges.

2.1. Removal of Off-position Contamination

As described in the previous section, the HEXOS Orion-S spectral survey was observed in DBS mode. Since the observations used the chopper in this mode, the reference positions were fixed to ~3 arcmin from the target position, with an angle set by observatory constraint. In a crowded field like the Orion Molecular Cloud region, it is very likely that the reference position is not free of emission or absorption for some or all of the molecular lines detected. Typically, emission (absorption) in the reference position appears as an absorption-(emission-)like feature in the final spectrum. Since the case of absorption in the reference beam is rare, due to a low continuum flux, we will consider only emission. Figure 5 provides an image of the dust emission at a wavelength of 250 μm obtained with the *Herschel*/SPIRE instrument. The positions of the Orion-S observations and the two reference observations for each of the 14 HIFI bands are overlaid. The diameters of the circles shown represent the FWHM of the individual beams for the center frequencies of each HIFI band. It is apparent that a few of the reference observations (on the east side) were located near the Orion Bar region, making reference beam line contamination very likely. In addition, we

[16] http://herschel.esac.esa.int/twiki/bin/view/Public/HifiCalibrationWeb#HIFI_performance_and_calibration

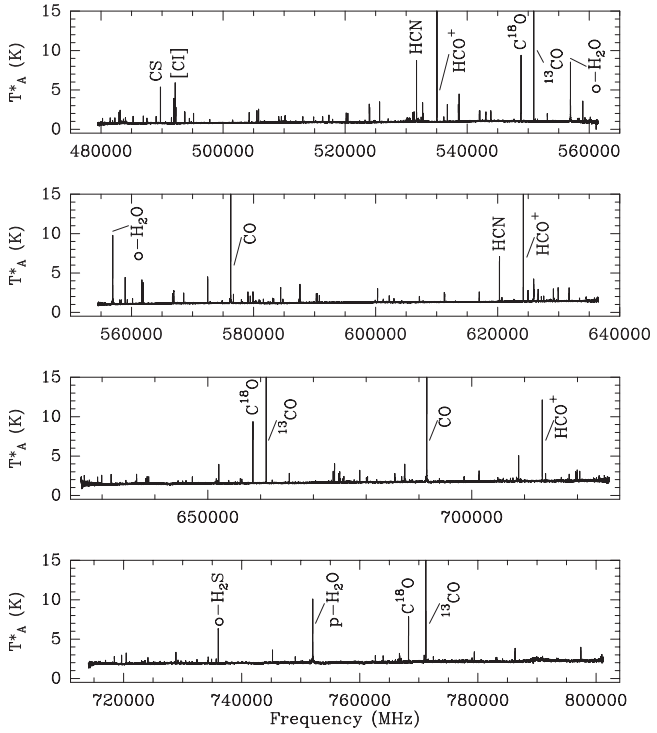

Figure 1. HEXOS/HIFI spectral scans of (from top to bottom) band 1a, band 1b, band 2a, and band 2b after Hanning smoothing. Resolutions, noise levels, and smoothing factors for each band are listed in Table 1. Baselines are not subtracted and some of the strongest lines are labelled.

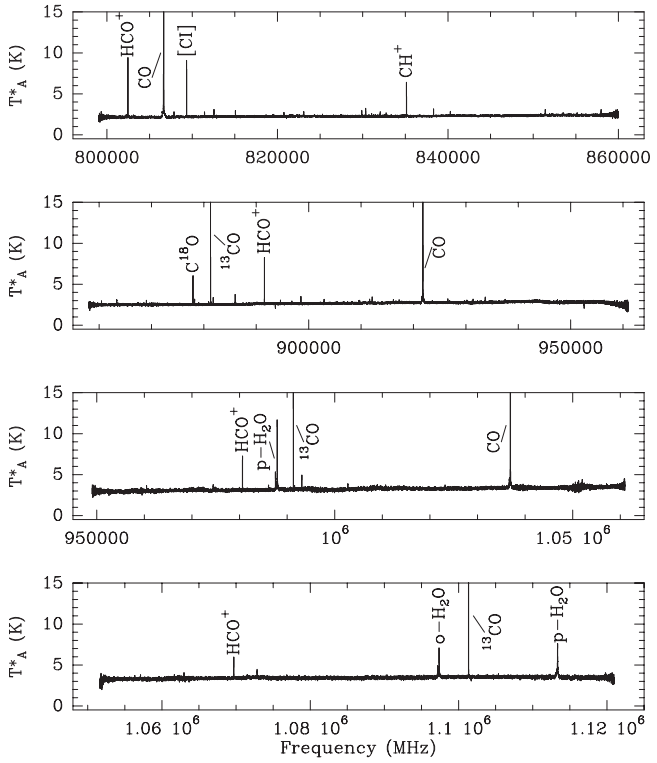

Figure 2. Same as Figure 1 except for band 3a, band 3b, band 4a, and band 4b.

even captured emission in the lower-J ^{12}CO transitions in the opposite chopping direction.

The identification of potentially contaminated lines was first performed after the deconvolution by checking the line profile

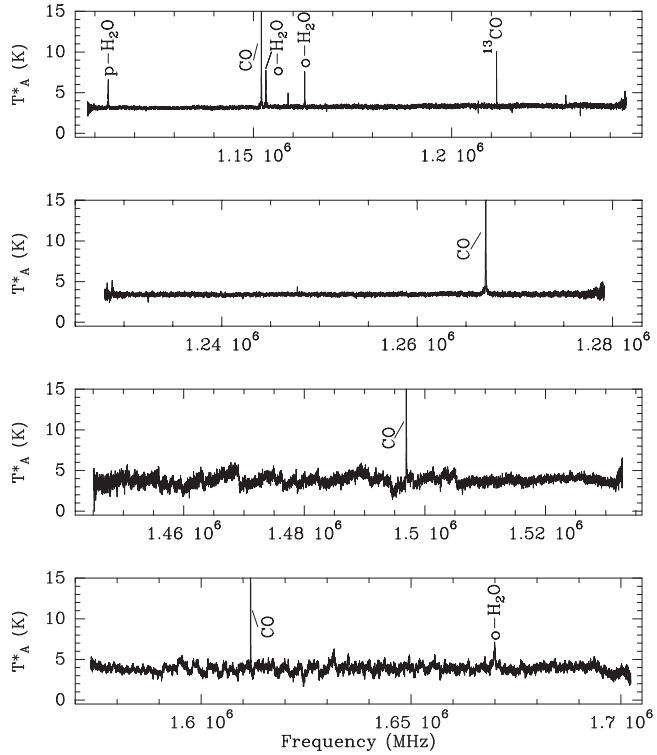

Figure 3. Same as Figure 1 except for band 5a, band 5b, band 6a, and band 6b. The higher noise level in band 6 is due to the HEB mixers, which produce higher noise in comparison with the SIS mixers used in the first five bands.

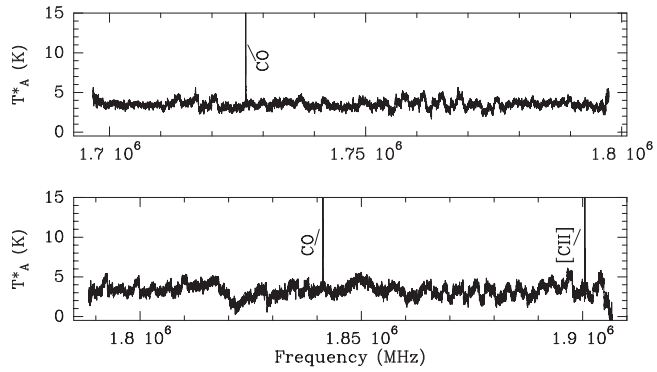

Figure 4. Same as Figure 1 except for band 7a and band 7b. The higher noise level in band 7 is due to the HEB mixers, which produce higher noise in comparison with the SIS mixers used in the first five bands.

of the detected lines. Once lines were identified, we performed additional tests by subtracting the Level 0.5 nod2 reference spectrum from the associated nod1 reference spectrum of the scans that cover the frequency ranges of these lines. If the resulting spectrum showed only noise, we assumed no emission in the reference spectra (we never experienced the case that emission in both reference beams cancelled out perfectly, which would hide this problem). If the resulting spectrum showed an emission line, there was emission in the nod1 reference beam; and if the spectrum showed an absorption feature, there was emission in the nod2 reference beam.

In order to remove the emission in the reference beams, we used the *Herschel*/HIPE hifiPipeline task to create the Level 0.5 product, in which the reference observations are still separated from the target observations. A custom HIPE script

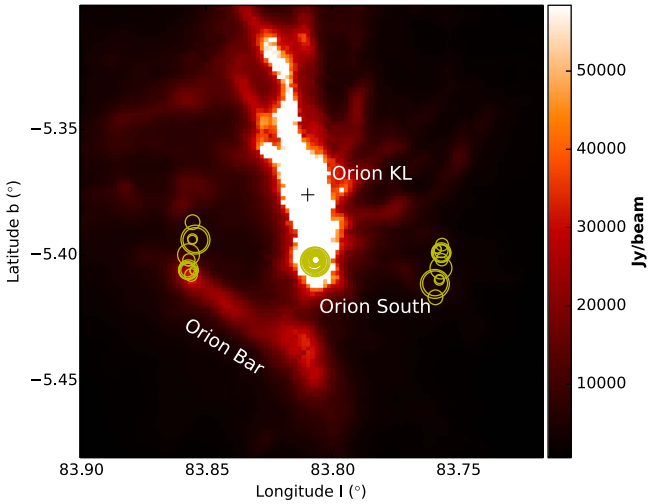

Figure 5. HEXOS Orion-S Observations: the circles indicate the beam positions with diameters corresponding to the FWHM at the center frequency of the HIFI bands. Circles near the center of the image (at $l \sim 83.81°$) indicate the position of the spectral scan observations of Orion-S. Circles to the left and to the right (at $l \sim 83.^{\circ}86$ and $83.^{\circ}76$ respectively) indicate the off-position observations. The background shows the *Herschel*/SPIRE 250 μm dust emission in the Orion-KL region (white regions indicate saturated pixels). From the location of the beam circles near the Orion Bar, it is apparent that some of the observations see emission in at least one reference beam.

then extracted all affected reference scans and the neighboring scans taken before and after the affected scans that have slightly changed LO settings such that the contaminating emission is at sufficiently different intermediate frequencies (IF). The repair is based on the assumption that the bandpass of all observations changes only very little with small changes in the LO-setting. The primary change is in the amplitude, while the shape of the bandpass changes negligibly. Thus, we could use the neighboring reference scans to repair the contaminated reference flux.

The first step of the repair was to determine the IF-frequency interval $[f_l, f_h]$, covering the reference beam emission and two smaller, abutting intervals $[f_l - \Delta_l, f_l]$ and $[f_h, f_h + \Delta_h]$, indicated by the green areas in Figure 6, for scaling. The next step included extracting and averaging the flux of the neighboring scans over the frequency range $[f_l - \Delta_l, f_h + \Delta_h]$ (Ref 1 and Ref 2 in Figure 6). Then, to properly scale the averaged flux to replace the contaminated flux, we determined the ratios of the original reference flux to the averaged flux over the two green intervals, interpolated the corresponding values over the interval containing the contaminated flux (the white area in Figure 6), and calculated the new reference flux by multiplying the averaged flux with the just determined ratio over the entire frequency range $[f_l - \Delta_l, f_h + \Delta_h]$. This new reference flux (New Ref) now replaced the original reference flux (Orig Ref). From here on, we continued to use the *Herschel*/HIPE hifiPipeline task to create the Level 1.0 and higher products.

The lines that needed repairs are B1a ([C I]), B2b (H_2S, $C^{18}O$, ^{13}CO, $C^{17}O$), B3a (CO, [C I], CH^+), B3b ($C^{18}O$, ^{13}CO, $C^{17}O$, CO), B4b (H_2S, $C^{18}O$, ^{13}CO), B5a ($C^{17}O$, CO, $C^{18}O$, ^{13}CO), B7a (CO), and B7b (CO, [C II]). Figure 7 shows an example of how the repair recovered the true line profile of the [C II] 158 μm line.

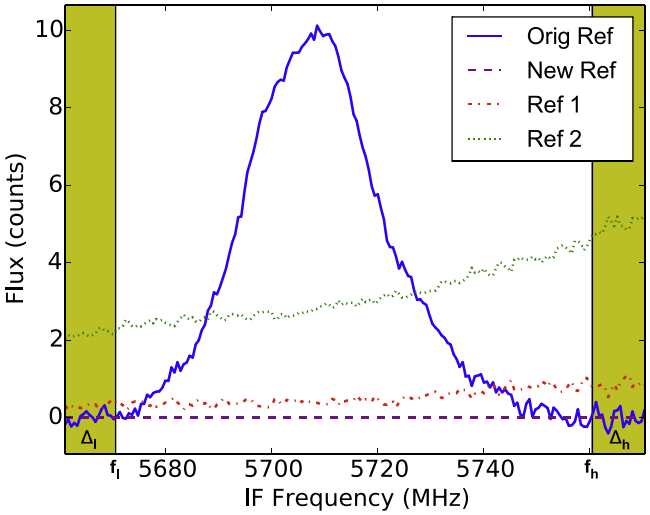

Figure 6. Removing the reference beam emission in the HEXOS Orion-S spectral scan: the blue solid line shows the emission in a reference beam. The red dashed and the green dotted lines show the references for an earlier scan and a later scan with slightly changed LO settings, but covering the same IF interval. Averaging and scaling these reference scans using just the frequency ranges marked with green background results in the new reference spectrum, which replaces the old reference spectrum only in the frequency range shown (the total spectrum is still 4 GHz wide or ~1 GHz for each of the 4 HIFI WBS sub-bands). For display purposes, we subtracted the new reference from all scans, causing it to appear as a straight line.

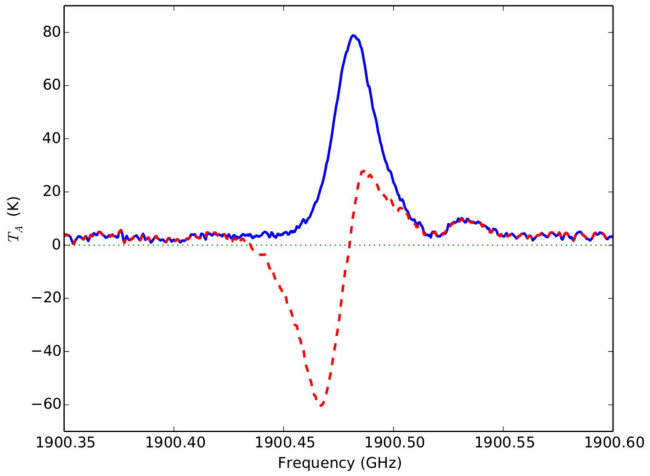

Figure 7. Example of the repaired [C II] line at 1900.526 GHz. The red dashed line shows the original result with emission in both reference beams and the blue solid line shows the result with the emission in the reference beams removed.

2.2. Line Identification

We used CASSIS,[17] a Java based software package designed to analyze astrophysical spectroscopic data to perform the line identification and modeling. Our line identification procedure involved two main steps. First, we visually identified the strongest (well above 5σ signal-to-noise) and best known emission lines in the spectrum (e.g., from CO, CS, HCO^+, HCN, H_2O, etc.) and some of their isotopologues utilizing the JPL[18] (Pearson et al. 2005) and CDMS[19] (Müller et al. 2005) spectral line databases. These databases include tabulated values of the central frequency error for each transition. Although, in some cases, the difference between the listed centroid frequency of a particular transition from these two catalogs is larger than their given error bars, the observed line width of the transition usually compensates for this ambiguity and makes the identification robust. Many of the strongest identified species are shown in Figures 1–4. In these cases, line blending (e.g., the appearance of more than one transition/species at a single frequency) is not considered a problem since the emission from the well-known species will invariably overwhelm the weak emission from a less well-known and, presumably, lower abundance blended line.

Once the strongest emission lines were accounted for, we examined all other spectral lines in our data that had a signal-to-noise ratio (S/N) above 3σ (in peak intensity). We first performed the line identification via visual inspection of each spectral feature in each HIFI band and compared the transition's frequency to those listed in the databases. From the possible database entries, we investigated all species with transitions that fell within a Doppler velocity range of 5.5 to 8.5 km s^{-1} (i.e., within ± 1.5 km s^{-1} of the assumed central velocity of Orion-S). Within this velocity range, we examined a smaller sub-sample of possible spectral lines with upper state excitation energies (E_{up}) less than 1500 K. If a single database entry from this sub-sample matched the observed spectral feature, we considered this to be a tentative identification. In order to confirm or reject this tentative identification, we then searched for other predicted transitions of the selected species in all of the HIFI bands. If we saw other spectral features in the data that matched the predicted frequencies, we accepted the initial line identification as being likely correct. If we did not, then the initial line identification was still considered to be only tentative, since we realize that the absence of other predicted transitions may be due to special excitation conditions. Therefore, in both cases, in order to finally confirm or reject our initial line identifications, Local Thermodynamic Equilibrium (LTE) modeling was performed (described in detail in Section 3), which allowed us to determine if all the observed spectral features from the tentatively detected species could be theoretically reproduced under uniform excitation conditions.

Our LTE models explored excitation conditions with $T_{ex} \leqslant 1500$ K (where T_{ex} is the excitation temperature—equal to the kinetic temperature in LTE), $E_{up} \leqslant 1500$ K, and total species column density $\leqslant 10^{17}$ cm^{-2}. If the LTE model produced emission at the frequency of the spectral feature, then the line identification was considered confirmed. If not, the species was assumed to have been incorrectly identified and a new identification for that spectral feature was sought. Note, at this stage, we are simply trying to produce some visible model emission at the frequency of the spectral feature and not trying to fit or replicate the observed spectral line profile. This will be performed in a subsequent stage described in Section 3.1. If a spectral feature could not be reproduced by an LTE model of any species, or if there was no database entry at the frequency of the observed spectral feature, that feature was listed as an unidentified line (32 lines in total). Visual inspection of the original, DSB spectra indicates that all of these features are "ghosts" (i.e., artifacts of the deconvolution routine). A list of

[17] CASSIS was developed by IRAP-UPS/CNRS. See http://cassis.irap.omp.eu

[18] http://spec.jpl.nasa.gov/ftp/pub/catalog/doc/catintro.pdf

[19] http://www.astro.uni-koeln.de/cdms/catalog

Table 2
Identified Species in Orion-S

Atoms	Di-atomic Molecules	Multi-atomic Molecules	Ionized Species
C-atom	CO	CCH	C^+
	^{13}CO	DCN	CH^+
	$^{13}C^{18}O$	HNC	CO^+
	$C^{18}O$	HCN	DCO^+
	$C^{17}O$	$H^{13}CN$	$H^{13}CO^+$
	CS	$HC^{15}N$	$HC^{18}O^+$
	^{13}CS	HDO[a]	HCO^+
	$C^{34}S$	o–H_2O	HCS^+
	CH	p–H_2O	N_2H^+
	CN	o–$H_2^{18}O$[a]	SH^+
	HCl[a]	p–$H_2^{18}O$[a]	…
	$H^{37}Cl$[a]	o–H_2S	…
	HF[a]	p–H_2S	…
	NO[a]	$H_2^{33}S$	…
	SiO	$H_2^{34}S$	…
	SO	H_2CS	…
	…	o–H_2CO	…
	…	p–H_2CO	…
	…	o–NH_3	…
	…	p–NH_3	…
	…	A–CH_3OH	…
	…	E–CH_3OH	…
	…	CH_3OCH_3	…
	…	NH_2	…
	…	SO_2	…

Note.
[a] JPL database used for these species. For all other species, the CDMS database is used.

all identified species is given in Table 2. A frequency ordered list of all spectral features above 3σ in intensity (as well as their peak intensity) is given in Table 3. Ghost lines are identified as "ghost." In total, we identified 52 different species (including isotopologues), which are responsible for 685 transitions (including the blended lines) in the HIFI spectra. It is, of course, possible that additional species and transitions exist in Orion-S, but at intensities too weak to be detected. This will be addressed in Section 3.3.2.

In some cases, our LTE modeling resulted in a particular spectral feature being reasonably explained by a superposition of lines from more than one species/transition (i.e., blended lines). In order to account for the possible effects of line blending, we performed modeling of all transitions of the two species in all HIFI bands. After obtaining good fits to the unblended transitions, we were able to determine how much each species contributed to the blended feature. An example of a blended line is shown in Figure 8, in which the data are shown by the black histogram, the solid red line indicates a $C^{17}O$ transition, the solid blue line indicates an H_2CO transition and the solid green line is the superposition of these two model results. Note that the solid green line in Figure 8 does not represent a multicomponent Gaussian fit but rather the LTE modeling required to reproduce the line profiles (see Section 3.1). Given the relatively few spectral lines in Orion-S, significant blending was only a problem in 6 of 685 lines detected. These blended lines are indicated by a "b" superscript in Tables 3 and 4. In Table 3, both species are listed. Blended

Table 3
All Observed Lines above the 3σ Noise Level in Order of Increasing Frequency

Frequency (GHz)	T_A (K)	Species
Band 1a		
480.2699	0.7	A–CH_3OH
481.5056	0.7	A–CH_3OH
481.9167	0.3	$C^{34}S$
482.2179	0.1	A–CH_3OH
482.2833	0.8	E–CH_3OH
482.9598	1.4	E–CH_3OH
483.0808	0.2	A–CH_3OH
483.1418	1.7	E–CH_3OH
483.3898	0.3	E–CH_3OH
483.3983	0.1	A–CH_3OH
483.4623	0.2	A–CH_3OH
483.4728	0.2	E–CH_3OH
483.5393	0.2	A–CH_3OH
483.5533	0.3	A–CH_3OH
483.5668	0.3	E–CH_3OH
483.5818	0.1	A–CH_3OH
483.6868	0.6	E–CH_3OH
483.7633	0.3	A–CH_3OH
484.0058	0.8	A–CH_3OH
484.0238	0.7	E–CH_3OH
484.0718	0.4	E–CH_3OH
484.2703	0.2	SO_2
485.2638	0.9	A–CH_3OH
486.9419	0.9	A–CH_3OH
487.5319	0.6	A–CH_3OH
487.6639	0.2	H_2CS
489.0379	0.9	A–CH_3OH
489.7509	4.5	CS
490.5970	0.2	HDO
491.5520	0.7	A–CH_3OH
491.9335	0.2	SO_2
491.9690	3.1	o–H_2CO
492.1615	4.7	[C I]
492.2795	2.0	A–CH_3OH
492.7841	0.1	CH_3OCH_3
493.7000	1.4	A–CH_3OH
493.7350	1.4	A–CH_3OH
494.4820	0.6	A–CH_3OH
494.7781	0.2	SO_2
495.1741	1.2	E–CH_3OH
496.9226	0.1	E–CH_3OH
497.8296	0.4	A–CH_3OH
501.5897	0.4	A–CH_3OH
503.0142	0.1	$H_2^{34}S$
504.2008	0.2	DCO^+
504.2948	1.3	E–CH_3OH
504.6783	0.1	SO
505.5658	1.5	o–H_2S
505.7633	0.3	A–CH_3OH
505.8343	1.7	p–H_2CO
506.1548	0.2	E–CH_3OH
506.7728	0.2	H_2CS
506.8273	0.2	DCN
508.5369	0.1	^{13}CS
508.7069	0.1	SO_2
509.0924	0.1	A–CH_3OH
509.1469	0.8	p–H_2CO
509.2939	0.3	HDO
509.5654[b]	0.8	E–CH_3OH + o–H_2CO
509.8314	0.3	p–H_2CO
510.1559	0.9	o–H_2CO

Table 3
(Continued)

Frequency (GHz)	T_A (K)	Species
510.2389	0.9	o–H_2CO
510.3459	0.3	A–CH_3OH
510.9114	0.1	$HC^{18}O^+$
511.0904	0.2	SO_2
511.5024	0.1	SO_2
511.7166	0.1	CH_3OCH_3
511.9455	0.2	HCS^+
513.0775	0.7	p–H_2CO
513.3610	0.1	H_2CS
513.3698	0.1	CH_3OCH_3
514.8535	0.7	SO
515.1700	0.2	A–CH_3OH
515.3335	0.2	A–CH_3OH
515.8230	0.1	Ghost
516.2616	0.2	$HC^{15}N$
516.3361[b]	0.7	SO
		+ H_2CS
517.3551	0.9	SO
517.9706	0.4	$H^{13}CN$
520.1801	1.2	E–CH_3OH
520.4612	1.1	$H^{13}CO^+$
520.7297	0.1	A–CH_3OH
520.8817	0.1	SiO
522.4057	0.1	H_2CS
523.1002	0.0	E–CH_3OH
523.2752	0.3	E–CH_3OH
523.4827	0.1	$^{13}C^{18}O$
523.9727	2.2	CCH
524.0352	1.8	CCH
524.2682	0.1	E–CH_3OH
524.5847	0.1	E–CH_3OH
524.6673	0.1	E–CH_3OH
524.7418	0.2	E–CH_3OH
524.8053	0.2	E–CH_3OH
524.8628	0.2	E–CH_3OH
524.9098	0.2	E–CH_3OH
524.9483	0.1	E–CH_3OH
525.0548	0.1	E–CH_3OH
525.6663	2.5	o–H_2CO
526.0363	0.1	SH^+
526.0453	0.1	SH^+
526.5233	0.1	A–CH_3OH
526.5483	0.1	E–CH_3OH
526.7878	0.1	E–CH_3OH
527.0548	0.4	A–CH_3OH
527.1738	0.1	E–CH_3OH
527.6608	0.1	E–CH_3OH
528.1813	0.1	E–CH_3OH
528.6833	0.1	E–CH_3OH
529.1419	0.2	E–CH_3OH
529.2904	0.1	SO_2
529.5409	0.2	E–CH_3OH
529.8679	0.2	E–CH_3OH
529.9739	0.2	SO_2
530.0699	0.2	A–CH_3OH
530.1234	0.3	$C^{34}S$
530.1849	0.6	E–CH_3OH
530.0244	0.1	E–CH_3OH
530.3174	0.4	E–CH_3OH
530.4559	0.5	E–CH_3OH
530.5499	0.5	E–CH_3OH
530.6124	0.5	E–CH_3OH
530.6484	0.5	E–CH_3OH

Table 3
(Continued)

Frequency (GHz)	T_A (K)	Species
530.8244	0.2	E–CH_3OH
531.0804	1.2	E–CH_3OH
531.3199	1.3	A–CH_3OH
531.6384	0.2	A–CH_3OH
531.7159	7.5	HCN
531.8709	0.4	A–CH_3OH
531.8924	0.3	A–CH_3OH
532.0334	0.4	E–CH_3OH
532.0709	0.2	E–CH_3OH
532.1349	0.3	A–CH_3OH
532.3239	0.1	CH_3OCH_3
532.4669	0.6	E–CH_3OH
532.5684	0.4	E–CH_3OH
532.7214	2.4	CH
532.7909	1.0	CH
533.3810	0.1	Ghost
535.0610	14.6	HCO^+
536.1925	0.6	A–CH_3OH
536.7585	2.1	CH
536.7805	0.5	CH
536.7925	0.9	CH
538.5716	2.2	A–CH_3OH
538.6891	3.4	CS
539.2806	0.1	E–CH_3OH
540.4656	0.2	H_2CS
540.9236	0.1	E–CH_3OH
541.7536	0.2	SO_2
541.8162	0.1	SO_2
542.0022	1.3	A–CH_3OH
542.0832	1.4	A–CH_3OH
543.0777	1.2	E–CH_3OH
543.8987	0.1	HNC
545.0437[b]	0.2	E–CH_3OH
		+ A–CH_3OH
545.1032	0.2	Ghost
545.8872	0.2	Ghost
546.2488	0.2	A–CH_3OH
547.3003	0.2	Ghost
547.6768	0.3	$H_2^{18}O$
548.8313	8.1	$C^{18}O$
549.2998	0.1	SO_2
549.5506	0.1	CH_3OCH_3
549.5533	0.1	NO
550.6564	0.0	A–CH_3OH
550.9254	29.4	^{13}CO
551.1874	0.3	NO
551.5159	0.1	Ghost
551.5344	0.3	NO
553.1474	1.0	E–CH_3OH
554.0569	0.2	E–CH_3OH
554.5784	0.1	HCS^+
555.6670	0.1	SO_2
556.9370	7.2	o–H_2O
557.1260	0.1	H_2CS
558.0870	0.3	SO
558.3465	0.4	E–CH_3OH
558.9681	2.5	N_2H^+
559.3216	0.4	SO
560.1781	0.5	SO
560.2496	0.2	E–CH_3OH
560.2716	0.2	E-CH_3OH
560.3001	0.2	Ghost

Table 3
(Continued)

Frequency (GHz)	T_A (K)	Species
Band 1b		
556.9370	8.4	o–H_2O
558.0875	0.5	SO
558.3460	0.5	E–CH_3OH
558.9681	3.4	N_2H^+
559.3206	0.5	SO
560.1781	0.6	SO
561.7136	3.0	$C^{17}O$
561.9001	2.7	o–H_2CO
564.2522	0.1	SiO
566.7312	1.3	CN
566.9477	1.6	CN
567.2612	0.2	Ghost
567.5953	0.1	SO_2
568.2358	0.2	E–CH_3OH
568.4353	0.2	CH_3OCH_3
568.5673	1.3	E–CH_3OH
568.7853	0.2	A–CH_3OH
570.2434	0.1	CH_3OCH_3
572.4974	3.3	o–NH_3
572.8984	0.2	E–CH_3OH
574.1399	0.1	H_2CS
574.8084	0.1	SO_2
574.8694	0.3	A–CH_3OH
576.2050[b]	0.4	DCO^+
576.2660	62.0	CO
576.3835	0.2	Ghost
576.7095	1.1	p–H_2CO
578.0080	0.4	E–CH_3OH
578.2165	0.2	$C^{34}S$
579.0860	1.4	A–CH_3OH
579.1520	0.8	E–CH_3OH
579.1995	0.1	DCN
579.4605	0.9	A–CH_3OH
579.8590	0.2	A–CH_3OH
579.9225	1.4	A–CH_3OH
580.0600	0.1	A–CH_3OH
580.1760	0.2	A–CH_3OH
580.2135	0.2	A–CH_3OH
580.3696	0.3	E–CH_3OH
580.4446	0.2	E–CH_3OH
580.5026	0.2	A–CH_3OH
580.9036	0.4	E–CH_3OH
581.0916	0.3	E–CH_3OH
581.6131	0.5	p–H_2CO
582.3841	0.2	o–H_2CO
582.7246	0.2	p–H_2CO
583.1456	0.6	o–H_2CO
583.3096	0.5	o–H_2CO
584.4511	1.9	A–CH_3OH
584.8227	0.5	A–CH_3OH
587.4537	0.4	p–H_2CO
587.5702	0.2	SO_2
587.6167	2.3	CS
589.1653	0.1	CH_3OCH_3
589.8703	0.1	CO^+
590.2793	1.2	A–CH_3OH
590.4418	1.1	A–CH_3OH
590.7522	0.1	CH_3OCH_3
590.7923	0.9	E–CH_3OH
591.8218	0.1	H_2CS
593.9424	0.1	SO_2
593.9624	0.1	SO_2

Table 3
(Continued)

Frequency (GHz)	T_A (K)	Species
597.2084	0.1	HCS^+
598.5485	−0.1	Ghost
599.9280	0.3	HDO
600.3320	1.7	o–H_2CO
600.9065	0.1	^{13}CS
601.2570	0.4	SO
601.8521	0.1	E–CH_3OH
602.2346	0.8	E–CH_3OH
602.2750		$HC^{15}N$
602.2916	0.4	SO
603.0236	0.5	SO
604.2641	0.2	$H^{13}CN$
604.3696	0.2	SO_2
605.8801	0.1	E–CH_3OH
607.1762	0.8	$H^{13}CO^+$
607.2167	0.3	E–CH_3OH
607.6112	0.1	SiO
607.7982	0.2	H_2CS
608.0984	0.1	CH_3OCH_3
609.7087	0.1	CH_3OCH_3
611.2688	1.2	CCH
611.3308	1.0	CCH
611.5518	0.1	SO
613.0798	0.1	SO_2
616.9814	1.2	E–CH_3OH
620.3035	5.6	HCN
620.7045	0.6	o–H_2O
622.5705	0.1	A–CH_3OH
622.6605	0.3	A–CH_3OH
622.7755	0.2	E–CH_3OH
624.1801	0.2	E–CH_3OH
624.2081	13.3	HCO^+
624.9616	1.0	$H^{37}Cl$
624.9751	1.4	$H^{37}Cl$
624.9856	0.6	$H^{37}Cl$
625.7521	0.4	E–CH_3OH
625.7601	0.1	A–CH_3OH
625.8996	2.1	HCl
625.9166	2.8	HCl
625.9296	1.5	HCl
626.0896	0.2	SO_2
626.3521	0.1	$C^{34}S$
626.4996	0.2	H_2CS
626.5141	0.1	A–CH_3OH
626.5566	0.2	E–CH_3OH
626.6271	1.5	A–CH_3OH
627.0203	0.1	CH_3OCH_3
627.1036	0.1	Ghost
627.1721	0.6	E–CH_3OH
627.5602	0.7	A–CH_3OH
628.0522	0.2	A–CH_3OH
628.1422	0.2	$^{13}C^{18}O$
628.3302	0.2	E–CH_3OH
628.4482	0.2	E–CH_3OH
628.4717	0.3	A–CH_3OH
628.5142	0.2	A–CH_3OH
628.5272	0.2	A–CH_3OH
628.6627	0.1	CH_3OCH_3
628.6982	0.3	E–CH_3OH
628.8182	0.2	E–CH_3OH
628.8682	0.2	A–CH_3OH
629.1417	1.6	A–CH_3OH
629.3232	0.4	E–CH_3OH

Table 3
(Continued)

Frequency (GHz)	T_A (K)	Species
629.6517	0.3	E–CH_3OH
629.9222	1.7	A–CH_3OH
631.2847	0.2	Ghost
631.7038	1.7	o–H_2CO
632.1918	0.2	SO_2
633.4248	0.4	A–CH_3OH
634.5118	0.6	HNC
635.8673	0.3	A–CH_3OH
636.3394	0.5	A–CH_3OH
636.3979	0.4	A–CH_3OH
636.4209	0.6	A–CH_3OH
Band 2a		
626.5191	0.7	A–CH_3OH
626.6271	1.3	A–CH_3OH
627.1711	0.6	E–CH_3OH
627.5607	0.5	A–CH_3OH
629.1417	1.0	A–CH_3OH
629.3242	0.3	E–CH_3OH
629.6482	0.3	E–CH_3OH
629.9232	1.2	A–CH_3OH
631.7038	1.3	o–H_2CO
633.4233	0.3	A–CH_3OH
634.5113	0.5	HNC
636.2514	0.2	A–CH_3OH
636.2749	0.3	A–CH_3OH
636.3059	0.3	A–CH_3OH
636.3349	0.3	A–CH_3OH
636.3669	0.4	A–CH_3OH
636.3949	0.4	A–CH_3OH
636.4209	0.3	A–CH_3OH
636.5199	0.3	A–CH_3OH
636.5339	1.3	CS
638.2804	0.7	E–CH_3OH
638.5259	1.0	A–CH_3OH
638.8194	0.9	A–CH_3OH
644.3252	0.2	NH_2
644.3790	0.4	SO
645.2576	0.4	SO
645.8756	0.4	SO
645.9282	0.1	CH_3OCH_3
647.0831	0.2	p–H_2CO
647.6130	0.2	CH_3OCH_3
648.1956	0.2	DCO^+
649.5402	0.2	E–CH_3OH
651.2997	0.1	SO_2
651.4352	0.3	NO
651.6177	0.6	E–CH_3OH
651.7742	0.4	NO
652.0972	2.8	N_2H^+
653.9703	0.4	p–H_2CO
655.2128	0.2	o–H_2CO
655.6353	0.2	p–H_2CO
656.1653	0.6	o–H_2CO
656.1723	0.4	E–CH_3OH
656.4663	0.5	o–H_2CO
658.5544	7.7	$C^{18}O$
661.0659	30.3	^{13}CO
662.2105	0.4	p–H_2CO
664.8193	0.1	CH_3OCH_3
665.2485	0.2	SO_2
665.4440	1.3	E–CH_3OH
670.3602	0.2	SO_2

Table 3
(Continued)

Frequency (GHz)	T_A (K)	Species
670.4242	0.3	A–CH_3OH
672.5657	0.2	SO_2
672.8362	0.1	A–CH_3OH
672.9037	0.3	E–CH_3OH
673.4172	0.3	E–CH_3OH
673.7472	1.4	A–CH_3OH
674.0107	2.4	$C^{17}O$
674.8113	1.1	o–H_2CO
674.9913[b]	1.4	A–CH_3OH + E–CH_3OH
675.0558	0.2	H_2CS
675.1353	0.5	E–CH_3OH
675.6138	0.5	A–CH_3OH
675.7748	0.8	E–CH_3OH
676.2143	0.3	A–CH_3OH
676.4618	0.1	SO_2
676.7523	0.3	A–CH_3OH
676.8298	0.3	A–CH_3OH
677.0138	0.3	E–CH_3OH
677.7113	0.4	E–CH_3OH
678.2528	0.2	E–CH_3OH
678.7688	0.2	Ghost
678.7864	1.6	A–CH_3OH
680.0429	0.6	CN
680.2599	0.8	CN
681.5310	−0.1	Ghost
681.9919	0.4	A–CH_3OH
685.4375	1.0	CS
685.5050	0.6	E–CH_3OH
686.7325	0.7	A–CH_3OH
687.0220	0.1	$H_2^{34}S$
687.1515	0.2	$H_2^{33}S$
687.2270	0.8	A–CH_3OH
687.3040	2.3	p–H_2S
687.4571	0.4	SO
688.2021	0.3	SO
688.7286	0.3	SO
690.5551	0.2	$H^{13}CN$
691.4706	64.4	CO
693.8787	0.4	$H^{13}CO^+$
697.1083	0.1	Ghost
697.1448	0.2	E–CH_3OH
698.5458	0.6	CCH
698.6083	0.6	CCH
701.3709[b]	1.3	o–H_2CO + E–CH_3OH
704.2609	0.2	Ghost
704.4134	0.2	CH_3OCH_3
704.9400	0.5	Ghost
705.1840	0.3	E–CH_3OH
705.4000	0.2	Ghost
705.9605	0.4	Ghost
706.6255	0.3	Ghost
707.3180	0.4	Ghost
707.7905	0.4	E–CH_3OH
708.4735[b]	0.5	o–H_2S
	0.0	+ H_2^{33} S
708.7085	0.4	Ghost
708.8741	3.2	HCN
709.2771	0.3	Ghost
713.3422	10.0	HCO^+
713.9837	0.9	E–CH_3OH
716.9402	0.5	p–H_2CO

Table 3
(Continued)

Frequency (GHz)	T_A (K)	Species
718.1618	0.3	A–CH_3OH
718.4378	0.9	E–CH_3OH
719.6653	1.1	A–CH_3OH
719.7293	1.0	Ghost
719.9548	1.5	Ghost
720.0118	0.9	E–CH_3OH
720.4418	1.2	A–CH_3OH
721.0118	0.2	E–CH_3OH
723.0404	0.4	E–CH_3OH
723.6219	0.4	A–CH_3OH
724.1224	0.7	E–CH_3OH
724.3489	0.4	A–CH_3OH
725.0954	0.9	Ghost
716.9412	0.6	p–H_2CO
Band 2b		
718.1623	0.3	A–CH_3OH
718.4378	1.0	E–CH_3OH
719.6668	1.2	A–CH_3OH
720.4433	1.4	A–CH_3OH
721.0093	0.3	E–CH_3OH
723.0429	0.5	E–CH_3OH
723.2824	0.3	E–CH_3OH
723.6199	0.5	A–CH_3OH
724.1219	0.9	E–CH_3OH
724.3409	0.2	A–CH_3OH
725.1089	0.3	HNC
725.1279	0.3	A–CH_3OH
725.3169	0.2	E–CH_3OH
726.0540	0.2	E–CH_3OH
726.2100	0.4	p–H_2CO
726.9025	0.3	E–CH_3OH
728.0535	0.3	o–H_2CO
728.5860	0.3	p–H_2CO
728.5960	0.2	p–H_2CO
728.8650	1.5	A–CH_3OH
729.2120	0.5	o–H_2CO
729.7260	0.4	o–H_2CO
730.5006	0.4	SO
730.5206	0.4	A–CH_3OH
731.1416	0.3	SO
731.5981	0.3	SO
732.4336	0.6	A–CH_3OH
732.7761	0.2	$^{13}C^{18}O$
734.2706	0.4	$H_2^{34}S$
734.3286	0.8	CS
734.8952	0.6	A–CH_3OH
735.6762	0.6	A–CH_3OH
736.0317	4.3	o–H_2S
737.3407	0.4	p–H_2CO
737.6272	0.2	Ghost
741.2263	0.2	E–CH_3OH
742.2408	0.2	H_2CS
745.2119	1.8	N_2H^+
747.3035	0.3	p–H_2S
749.0735	0.8	o–H_2CO
751.5560	0.4	E–CH_3OH
751.6766	0.3	NO
752.0321	7.9	p–H_2O
752.1076	0.6	E–CH_3OH
752.1366	0.4	E–CH_3OH
752.1716	0.3	E–CH_3OH
752.3111	0.3	E–CH_3OH

Table 3
(Continued)

Frequency (GHz)	T_A (K)	Species
753.4161	0.2	HDO
753.8671	0.1	E–CH_3OH
754.2226	0.2	E–CH_3OH
762.6378	0.9	E–CH_3OH
763.8823	0.3	E–CH_3OH
763.9533	0.9	A–CH_3OH
764.5828	−0.5	Ghost
764.8119	0.2	E–CH_3OH
765.5134	0.2	E–CH_3OH
765.9404	0.2	o–H_2S
766.0309	0.3	E–CH_3OH
766.3974	0.4	E–CH_3OH
766.6489	0.5	E–CH_3OH
766.7124	1.2	A–CH_3OH
766.7624	0.8	E–CH_3OH
766.8114	0.4	E–CH_3OH
766.9094	0.5	E–CH_3OH
766.9614	0.5	E–CH_3OH
766.9844	0.5	E–CH_3OH
768.2529	5.6	$C^{18}O$
768.5404	0.2	E–CH_3OH
770.8855	0.4	E–CH_3OH
770.8980	0.9	o–H_2CO
771.1825	27.1	^{13}CO
771.5770	0.4	A–CH_3OH
772.4425	0.2	A–CH_3OH
772.4545	0.6	E–CH_3OH
773.2611	0.2	A–CH_3OH
773.4226	0.3	A–CH_3OH
773.5136	0.3	SO
773.8896	0.2	E–CH_3OH
773.9481	0.2	A–CH_3OH
774.0666	0.2	SO
774.3331	0.3	E–CH_3OH
774.4541	0.3	SO
775.5996	0.4	E–CH_3OH
779.0072	0.5	A–CH_3OH
779.0322	0.4	E–CH_3OH
779.3822	1.3	A–CH_3OH
780.5672	0.3	$H^{13}CO^+$
783.0028	0.5	A–CH_3OH
783.1993	0.6	CS
784.1793	0.3	A–CH_3OH
785.8058	0.3	CCH
785.8679	0.2	CCH
786.2829[b]	1.5	$C^{17}O$ + p–H_2CO
790.9360	0.7	Ghost
793.3410	0.4	CN
793.5480	0.3	CN
794.5211	0.2	Ghost
794.8206	0.2	Ghost
797.4306	1.7	HCN
798.3106	0.2	p–H_2CO
Band 3a		
802.2430	0.3	E–CH_3OH
802.2810	0.3	o–H_2CO
802.4590	7.1	HCO^+
803.1130	0.3	o–H_2CO
806.6501	59.4	CO
807.8661	0.6	A–CH_3OH
809.3431	6.8	[C I]

Table 3
(Continued)

Frequency (GHz)	T_A (K)	Species
811.4452	0.6	E–CH_3OH
812.5522	0.9	A–CH_3OH
813.5442	0.2	A–CH_3OH
815.0723	0.8	E–CH_3OH
815.6943	0.1	HNC
816.0153	0.2	E–CH_3OH
816.4953	0.2	SO
816.9743	0.2	SO
817.3143	0.2	SO
818.6674	0.2	E–CH_3OH
819.4844	0.3	A–CH_3OH
820.5024	0.2	A–CH_3OH
820.7644	0.4	E–CH_3OH
821.4774	0.2	A–CH_3OH
821.7014	0.2	A–CH_3OH
821.8694	0.2	E–CH_3OH
822.5475	0.3	E–CH_3OH
823.0845	0.6	o–H_2CO
824.3525	0.2	E–CH_3OH
824.7255	0.2	E–CH_3OH
825.2795	0.3	E–CH_3OH
827.4516	0.2	A–CH_3OH
829.8906	0.7	A–CH_3OH
830.3506	1.0	A–CH_3OH
831.0487	0.3	A–CH_3OH
832.0627	0.5	CS
832.7567	0.4	A–CH_3OH
834.6517	0.2	E–CH_3OH
834.7517	0.1	E–CH_3OH
834.8397	0.2	E–CH_3OH
834.9017	0.1	E–CH_3OH
834.9577	0.2	E–CH_3OH
835.0037	0.1	E–CH_3OH
835.1358	3.0	CH^+
838.3088	0.8	N_2H^+
840.2779	0.6	o–H_2CO
851.4161	0.7	A–CH_3OH
851.9151	0.3	NO
853.5112	0.3	E–CH_3OH
855.1542	0.3	p–H_2CO
857.9613	0.7	A–CH_3OH
Band 3b		
860.4618	0.5	E–CH_3OH
863.3639	0.6	E–CH_3OH
863.4269	0.2	E–CH_3OH
867.3250	0.3	A–CH_3OH
869.0370	0.5	E–CH_3OH
869.9821	0.3	A–CH_3OH
870.1091	0.2	E–CH_3OH
870.2811	0.2	p–H_2CO
873.0361	0.2	CCH
873.7811	0.1	o–H_2CO
875.3692	0.2	o–H_2CO
876.6462	0.1	o–H_2CO
877.9232	3.4	$C^{18}O$
878.2273	0.7	A–CH_3OH
879.0153	0.2	A–CH_3OH
880.9043	0.3	CS
881.2703	21.6	^{13}CO
881.4223	0.3	A–CH_3OH
881.7833	0.8	A–CH_3OH
885.9664	1.2	HCN

Table 3
(Continued)

Frequency (GHz)	T_A (K)	Species
890.1265	0.3	E–CH_3OH
891.5586	5.5	HCO^+
893.6387	−0.7	HDO
894.6146	0.5	A–CH_3OH
896.8077	0.3	o–H_2CO
898.5247	0.9	$C^{17}O$
898.9777	0.2	Ghost
900.9658	0.1	E–CH_3OH
902.9388	0.5	A–CH_3OH
902.9838	0.2	SO
905.3959	0.2	E–CH_3OH
905.3959	0.2	E–CH_3OH
906.5939	0.2	CN
906.8029	0.2	CN
907.4303	0.2	NH_2
909.5120	0.3	o–H_2CO
909.7400	0.4	E–CH_3OH
910.8110	0.2	E–CH_3OH
911.6440	0.5	E–CH_3OH
912.1100	0.8	E–CH_3OH
916.1771	0.5	p–H_2O
916.6502	0.3	E–CH_3OH
917.2702	0.4	E–CH_3OH
917.4082	0.2	E–CH_3OH
921.7973	59.5	CO
921.9873	0.5	E–CH_3OH
923.5853	0.3	p–H_2CO
926.5564	0.5	A–CH_3OH
926.8944	0.3	A–CH_3OH
929.7315	0.3	CS
930.2035	0.3	A–CH_3OH
931.3885	0.4	N_2H^+
933.6945	0.6	A–CH_3OH
937.4826	0.4	A–CH_3OH
947.4759	0.3	A–CH_3OH
952.5422	−0.3	NH_2
952.5740	−0.8	NH_2
952.6268	−0.3	NH_2
Band 4a		
960.4732	0.6	E–CH_3OH
965.4513	0.4	E–CH_3OH
974.4895	0.7	HCN
974.6895	0.3	A–CH_3OH
974.8795	0.5	A–CH_3OH
980.0316	0.4	A–CH_3OH
980.6376	4.3	HCO^+
986.1018	0.6	A–CH_3OH
987.5618	2.2	$C^{18}O$
987.9298	8.5	p–H_2O
991.3259	17.6	^{13}CO
991.5839	0.5	A–CH_3OH
993.1019	1.7	o–H_2S
1002.7782	0.8	p–H_2S
1006.1242	0.4	E–CH_3OH
1008.8183	0.6	E–CH_3OH
1010.7323	0.6	$C^{17}O$
1013.5664	0.4	E–CH_3OH
1023.1986	0.6	A–CH_3OH
1036.6990	1.1	SO_2
1036.9070	66.9	CO
1039.0150	0.5	A–CH_3OH
1057.1194	0.5	E–CH_3OH

Table 3
(Continued)

Frequency (GHz)	T_A (K)	Species
Band 4b		
1057.1239	0.5	E–CH_3OH
1062.9821	1.0	HCN
1069.6982	2.8	HCO^+
1072.8303	1.0	o–H_2S
1092.4668	0.4	A–CH_3OH
1097.1589	1.4	$C^{18}O$
1097.3689	3.4	o–H_2O
1101.3450	12.5	^{13}CO
1101.6990	−0.7	p–$H_2^{18}O$
1105.3691	0.4	E–CH_3OH
1113.3472	4.0	p–H_2O
Band 5a		
1113.3477	3.5	p–H_2O
1119.8339	0.4	A–CH_3OH
1122.9060	0.3	$C^{17}O$
1151.4506	0.6	HCN
1151.7555	0.9	A–CH_3OH
1151.9826	51.0	CO
1152.9207	0.6	A–CH_3OH
1153.1267	4.4	o–H_2O
1153.5527	0.6	E–CH_3OH
1158.7328	1.7	HCO^+
1162.7149[b]	0.6	A–CH_3OH + E–CH_3OH
1162.9129	4.4	o–H_2O
1168.1190	0.5	A–CH_3OH
1168.4524	−1.1	p–NH_3
1196.0197	0.5	o–H_2S
1206.7279	0.7	$C^{18}O$
1207.6540	0.5	p–H_2O
1211.3260	6.8	^{13}CO
1214.8529	−1.0	o–NH_3
1215.2457	−1.3	p–NH_3
1228.7924	1.3	p–H_2O
1232.4685	−1.2	HF
Band 5b		
1228.7922	1.7	p–H_2O
1232.4692	−1.2	HF
1239.9125	0.4	HCN
1247.7406	0.8	HCO^+
1267.0091	44.6	CO
Band 6a		
1496.9192	42.0	CO
Band 6b		
1611.7859	37.3	CO
1669.9169	7.7	o–H_2O
Band 7a		
1726.5976	26.9	CO
Band 7b		
1841.3367	20.1	CO
1900.5261	69.5	[C II]

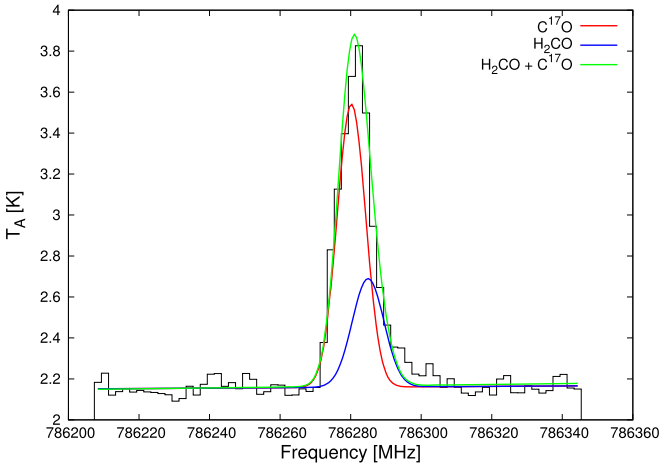

Figure 8. Example of a blended line at 786.3 GHz, produced by $C^{17}O$ and H_2CO. The red line shows the LTE modeled synthetic spectrum for $C^{17}O$ and the blue line shows that for H_2CO (Tables 5 and 6). The green line is the superposition of these two components. Data are shown by the black histogram.

lines were excluded from the modeling analysis presented in Section 3.

2.3. Line Profiles

Although all lines above the 3σ S/N level in intensity were identified, Gaussian fitting and subsequent modeling was only performed on lines that were above the 5σ noise level (where the noise is calculated from line-free regions of the spectrum immediately adjacent to the line). Gaussian fits were obtained using the Levenberg–Marquardt algorithm as implemented in the CASSIS software package and were done independently from LTE modeling, the latter of which will be described in Section 3.1. A linear or a second order baseline was fit to the data prior to Gaussian fitting, but was not removed so we could include the continuum in subsequent modeling (important for absorption lines).

In most cases, a single component Gaussian fit to a specific species could reasonably reproduce the observed lines. However, in some cases, a two component Gaussian fit was needed, one component being narrow ($\Delta V_{\rm FWHM}$ = 3–5 km s^{-1}) and the other broad ($\Delta V_{\rm FWHM}$ = 7–14 km s^{-1}); the latter could be the effect of a hot core, an outflow, or a shock. Figure 9 provides an example of a species that needed only a single component fit (^{13}CO), whereas Figure 10 shows the spectra for HCN, a typical example of a species requiring a two component fit. In addition, $^{12}C^{16}O$ line profiles are the only ones among 52 identified species, which clearly had a non-Gaussian shape, probably due to self-absorption. A few other transitions are seen in absorption rather than emission and are listed in Table 3 with negative intensities.

Table 4 shows the results of the Gaussian fitting for each species. The reported result for each individual line profile is the best Gaussian fit. We should note that, usually, the signal-to-noise ratio is lower, as we move to higher frequencies. In the case of a two component fit, the narrower component is referred to as "main" and the broad component is referred to as "wing." The first column in Table 4 is the transition quantum number (an explanation of the quantum numbers is provided on

Table 4
Gaussian Fits to Lines above 5σ

[C I]

Transition $^{2s+1}L_{\lvert L+S\rvert}$	Frequency MHz	T_A (K)	V_{LSR} (km s^{-1})	ΔV_{FWHM} (km s^{-1})	$\int T_A dV$ (K km s^{-1})	E_u (K)
$^3P_1 \rightarrow {}^3P_0$	492161.28	5.2	7.6	4.7	26.1	23.62
$^3P_2 \rightarrow {}^3P_1$	809342.91	6.9	7.2	4.2	30.8	62.46

[C II]

Transition $^{2s+1}L_{\lvert L+S\rvert}$	Frequency MHz	T_A (K)	V_{LSR} (km s^{-1})	ΔV_{FWHM} (km s^{-1})	$\int T_A dV$ (K km s^{-1})	E_u (K)
$^2P_{3/2} \rightarrow {}^2P_{1/2}$	1900527.55	69.1	8.6	3.8	279.8	91.21

CCH

Transition N_{J,F_1}	Frequency MHz	T_A (K)	V_{LSR} (km s^{-1})	ΔV_{FWHM} (km s^{-1})	$\int T_A dV$ (K km s^{-1})	E_u (K)
$6_{6.5,7} \rightarrow 5_{5.5,6}$	523972.07	2.2	6.6	4.5	10.7	88.02
$6_{5.56} \rightarrow 5_{4.5,5}$	524034.40	1.9	6.7	4.0	8.1	88.04
$7_{7.5,8} \rightarrow 6_{6.5,7}$	611267.06	1.2	6.8	5.2	6.4	117.36
$7_{6.5,6} \rightarrow 6_{5.5,5}$	611329.64	1.0	7.0	4.9	5.0	117.38
$8_{8.5,9} \rightarrow 7_{7.5,8}$	698544.47	0.6	7.4	5.9	3.7	150.88
$8_{7.5,7} \rightarrow 7_{6.5,6}$	698607.43	0.5	7.0	5.2	2.8	150.91
$9_{9.5,10} \rightarrow 8_{8.5,9}$	785801.64	0.3	7.9	8.2	2.3	188.59
$9_{8.5,8} \rightarrow 8_{7.5,7}$	785864.19	0.2	7.0	5.8	1.3	188.62

CH

Transition N_{K,J,F_1}	Frequency MHz	T_A (K)	V_{LSR} (km s^{-1})	ΔV_{FWHM} (km s^{-1})	$\int T_A dV$ (K km s^{-1})	E_u (K)
$1_{1,1.5,1} \rightarrow 1_{-1,0.5,1}$	532721.73	2.4	7.1	4.2	10.8	25.73
$1_{1,1.5,1} \rightarrow 1_{-1,0.5,0}$	532791.46	1.0	8.4	4.8	4.9	25.73
$1_{-1,1.5,2} \rightarrow 1_{1,0.5,1}$	536759.12	2.2	8.2	4.0	9.2	25.73
$1_{-1,1.5,1} \rightarrow 1_{1,0.5,1}$	536779.69	0.6	8.3	3.8	2.2	25.76
$1_{-1,1.5,1} \rightarrow 1_{1,0.5,0}$	536793.54	1.0	8.3	4.1	4.2	25.76

CH^+

Transition J	Frequency MHz	T_A (K)	V_{LSR} (km s^{-1})	ΔV_{FWHM} (km s^{-1})	$\int T_A dV$ (K km s^{-1})	E_u (K)
$1 \rightarrow 0$	835135.84	4.0	8.3	4.8	20.4	40.08

A–CH_3OH

Transition $J_{+K,v_t^{\pi}}$	Frequency MHz	T_A (K)	V_{LSR} (km s^{-1})	ΔV_{FWHM} (km s^{-1})	$\int T_A dV$ (K km s^{-1})	E_u (K)
$3_{2,0^+} \rightarrow 3_{1,0^-}$	480269.83	0.7	6.7	3.7	2.7	51.64
$2_{2,0^+} \rightarrow 2_{1,0^-}$	481505.55	0.7	6.1	3.3	2.4	44.67
$10_{0,0^+} \rightarrow 9_{0,0^+}$	483141.47	1.5	6.6	4.3	6.9	127.6
$10_{2,0^-} \rightarrow 9_{2,0^-}$	483388.95	0.3	6.8	4.9	1.4	165.35
$10_{3,0^+} \rightarrow 9_{3,0^+}$	483553.40	0.2	5.5	6.4	1.7	177.46
$10_{3,0^-} \rightarrow 9_{3,0^-}$	483566.43	0.3	6.5	3.9	1.2	177.46
$10_{2,0^+} \rightarrow 9_{2,0^+}$	483762.05	0.2	6.6	5.7	1.4	165.4
$2_{2,0^-} \rightarrow 2_{1,0^+}$	484005.49	0.7	6.5	4.2	3.0	44.67
$3_{2,0^-} \rightarrow 3_{1,0^+}$	485263.94	0.8	6.6	4.0	3.5	51.64
$4_{2,0^-} \rightarrow 4_{1,0^+}$	486941.55	0.9	6.5	4.1	3.7	60.92
$10_{1,0^-} \rightarrow 9_{1,0^-}$	487532.70	0.6	6.5	4.4	2.9	143.28
$5_{2,0^-} \rightarrow 5_{1,0^+}$	489037.53	0.8	6.6	4.1	3.5	72.53
$6_{2,0^-} \rightarrow 6_{1,0^+}$	491551.87	0.7	6.3	4.1	2.9	86.46
$4_{1,0^+} \rightarrow 3_{0,0^+}$	492279.27	2.0	6.7	4.2	8.8	37.55
$5_{3,0^+} \rightarrow 4_{2,0^+}$	493699.96	1.3	6.5	3.7	5.1	84.62

Table 4
(Continued)

A–CH_3OH

Transition J_{+K,v_t^π}	Frequency MHz	T_A (K)	V_{LSR} (km s^{-1})	ΔV_{FWHM} (km s^{-1})	$\int T_A dV$ (K km s^{-1})	E_u (K)
$5_{3,0^-} \rightarrow 4_{2,0^-}$	493734.65	1.4	6.4	3.7	5.3	84.62
$7_{2,0^-} \rightarrow 7_{1,0^+}$	494482.35	0.6	6.5	4.3	2.6	102.7
$8_{2,0^-} \rightarrow 8_{1,0^+}$	497829.07	0.4	6.4	4.3	2.0	121.27
$9_{2,0^-} \rightarrow 9_{1,0^+}$	501589.39	0.4	6.7	4.0	1.5	142.15
$10_{2,0^-} \rightarrow 10_{1,0^+}$	505762.88	0.3	6.4	4.5	1.3	165.35
$11_{2,0^-} \rightarrow 11_{1,0^+}$	510345.79	0.2	6.4	4.7	1.0	190.86
$16_{0,0^+} \rightarrow 15_{1,0^+}$	515170.91	0.2	6.6	4.9	1.1	315.21
$11_{1,0^+} \rightarrow 10_{1,0^+}$	527054.34	0.4	6.5	3.9	1.6	166.37
$11_{0,0^+} \rightarrow 10_{0,0^+}$	531320.09	1.2	6.6	4.3	5.4	153.1
$11_{2,0^-} \rightarrow 10_{2,0^-}$	531636.16	0.2	7.1	6.9	1.7	190.87
$11_{4,0^-} \rightarrow 10_{4,0^-}$	531869.53	0.4	7.5	6.2	2.3	233.52
$11_{3,0^-} \rightarrow 10_{3,0^-}$	531893.14	0.3	6.9	4.8	1.4	202.98
$11_{2,0^+} \rightarrow 10_{2,0^+}$	532133.99	0.3	6.2	4.1	1.1	190.94

A–CH_3OH

Transition J_{+K,v_t^π}	Frequency MHz	T_A (K)	V_{LSR} (km s^{-1})	ΔV_{FWHM} (km s^{-1})	$\int T_A dV$ (K km s^{-1})	E_u (K)
$11_{1,0^-} \rightarrow 10_{1,0^-}$	536192.13	0.6	6.4	3.7	2.4	169.01
$5_{1,0^+} \rightarrow 4_{0,0^+}$	538571.19	2.1	6.7	4.4	9.7	49.06
$6_{3,0^+} \rightarrow 5_{2,0^+}$	542002.05	1.2	6.4	3.7	4.7	98.55
$6_{3,0^-} \rightarrow 5_{2,0^-}$	542082.94	1.2	6.5	3.7	4.7	98.55
$12_{1,0^+} \rightarrow 11_{1,0^+}$	574869.74	0.3	6.3	4.2	1.4	193.96
$2_{2,0^-} \rightarrow 1_{1,0^-}$	579085.75	1.3	6.5	3.7	5.2	44.67
$12_{0,0^+} \rightarrow 11_{0,0^+}$	579460.65	0.9	6.5	4.4	4.0	180.91
$2_{2,0^+} \rightarrow 1_{1,0^+}$	579922.27	1.3	6.5	4.1	5.7	44.67
$12_{3,0^+} \rightarrow 11_{3,0^+}$	580176.81	0.2	6.6	4.2	0.8	230.83
$12_{3,0^-} \rightarrow 11_{3,0^-}$	580212.19	0.2	7.3	5.3	1.1	230.83
$12_{2,0^+} \rightarrow 11_{2,0^+}$	580503.31	0.2	6.3	4.5	0.9	218.8
$6_{1,0^+} \rightarrow 5_{0,0^+}$	584450.72	2.5	6.6	4.3	11.3	62.87
$12_{1,0^-} \rightarrow 11_{1,0^-}$	584823.31	0.4	6.6	5.3	2.5	197.08
$7_{3,0^+} \rightarrow 6_{2,0^+}$	590278.73	1.0	6.5	3.9	4.3	114.79
$7_{3,0^-} \rightarrow 6_{2,0^-}$	590441.53	1.0	6.4	3.8	4.1	114.79
$13_{1,0^+} \rightarrow 12_{1,0^+}$	622660.02	0.3	6.4	4.3	1.4	223.85
$3_{2,0^-} \rightarrow 2_{1,0^-}$	626627.34	1.4	6.5	3.9	5.5	51.64
$13_{0,0^+} \rightarrow 12_{0,0^+}$	627559.43	0.6	6.5	5.4	3.4	211.03
$13_{2,0^-} \rightarrow 12_{2,0^-}$	628052.23	0.2	6.8	6.0	1.2	248.84
$13_{3,0^+} \rightarrow 12_{3,0^+}$	628471.51	0.2	6.2	6.3	1.3	260.99
$13_{4,0^-} \rightarrow 12_{4,0^-}$	628513.72	0.2	6.3	3.5	0.7	291.53
$13_{3,0^-} \rightarrow 12_{3,0^-}$	628524.83	0.2	7.1	5.3	1.1	261
$13_{2,0^+} \rightarrow 12_{2,0^+}$	628868.08	0.2	7.5	5.1	1.1	248.98
$3_{2,0^+} \rightarrow 2_{1,0^+}$	629141.49	1.4	6.5	4.1	6.2	51.64
$7_{1,0^+} \rightarrow 6_{0,0^+}$	629922.01	1.6	6.7	4.6	7.9	78.97
$13_{1,0^-} \rightarrow 12_{1,0^-}$	633424.48	0.4	6.3	4.9	2.1	227.48
$7_{4,0^-} \rightarrow 7_{3,0^+}$	636336.97	0.3	7.2	4.1	1.2	145.33
$4_{4,0^-} \rightarrow 4_{3,0^+}$	636422.01	0.5	6.0	2.8	1.5	103.56
$3_{2,0^-} \rightarrow 2_{1,0^-}$	626627.67	1.1	6.3	4.0	4.8	51.64
$13_{0,0^+} \rightarrow 12_{0,0^+}$	627560.25	0.5	6.1	3.9	2.0	211.03
$3_{2,0^+} \rightarrow 2_{1,0^+}$	629141.29	1.0	6.6	4.2	4.2	51.64
$7_{1,0^+} \rightarrow 6_{0,0^+}$	629921.68	1.1	6.8	5.0	5.9	78.97
$13_{1,0^-} \rightarrow 12_{1,0^-}$	633425.22	0.2	6.0	5.2	1.3	227.48
$7_{4,0^-} \rightarrow 7_{3,0^+}$	636335.86	0.3	7.7	4.4	1.4	145.33

Table 4
(Continued)

A–CH_3OH

Transition J_{+K,v_t^π}	Frequency MHz	T_A (K)	V_{LSR} (km s^{-1})	ΔV_{FWHM} (km s^{-1})	$\int T_A dV$ (K km s^{-1})	E_u (K)
$6_{4,0^+} \rightarrow 6_{3,0^-}$	636365.90	0.3	6.1	4.4	1.6	129.09
$5_{4,0^-} \rightarrow 5_{3,0^+}$	636395.60	0.3	6.1	4.6	1.6	115.16
$4_{4,0^+} \rightarrow 4_{3,0^-}$	636420.70	0.3	6.6	3.5	1.0	103.56

A–CH_3OH

Transition J_{+K,v_t^π}	Frequency MHz	T_A (K)	V_{LSR} (km s^{-1})	ΔV_{FWHM} (km s^{-1})	$\int T_A dV$ (K km s^{-1})	E_u (K)
$8_{3,0^+} \rightarrow 7_{2,0^+}$	638524.78	0.9	6.4	4.4	4.3	133.36
$8_{3,0^-} \rightarrow 7_{2,0^-}$	638818.88	0.9	6.5	4.4	4.0	133.36
$14_{1,0^+} \rightarrow 13_{1,0^+}$	670424.18	0.2	6.3	6.8	1.6	256.02
$4_{2,0^-} \rightarrow 3_{1,0^-}$	673747.18	1.3	6.5	4.2	5.8	60.92
$8_{1,0^+} \rightarrow 7_{0,0^+}$	674991.12	1.3	6.8	4.5	6.2	97.38
$14_{0,0^+} \rightarrow 13_{0,0^+}$	675613.75	0.5	6.5	5.5	2.8	243.45
$4_{2,0^+} \rightarrow 3_{1,0^+}$	678786.36	1.4	6.5	3.9	5.9	60.93
$14_{1,0^-} \rightarrow 13_{1,0^-}$	681991.47	0.3	6.3	6.9	2.2	260.21
$9_{3,0^+} \rightarrow 8_{2,0^+}$	686733.14	0.7	6.3	4.0	2.8	154.25
$9_{3,0^-} \rightarrow 8_{2,0^-}$	687225.61	0.7	6.6	4.7	3.6	154.25
$9_{1,0^+} \rightarrow 8_{0,0^+}$	719665.76	1.0	6.6	5.2	5.7	118.08
$5_{2,0^-} \rightarrow 4_{1,0^-}$	720442.77	1.1	6.5	3.9	4.6	72.53
$15_{0,0^+} \rightarrow 14_{0,0^+}$	723621.75	0.4	6.0	4.8	1.8	278.18
$9_{1,0^+} \rightarrow 8_{0,0^+}$	719665.58	1.1	6.7	4.6	5.4	118.08
$5_{2,0^-} \rightarrow 4_{1,0^-}$	720442.56	1.3	6.5	4.1	5.7	72.53
$15_{0,0^+} \rightarrow 14_{0,0^+}$	723620.68	0.4	6.4	6.1	2.8	278.18
$5_{2,0^+} \rightarrow 4_{1,0^+}$	728863.72	1.4	6.5	4.3	6.3	72.53
$15_{1,0^-} \rightarrow 14_{1,0^-}$	730520.33	0.3	6.7	5.1	1.5	295.27
$10_{3,0^+} \rightarrow 9_{2,0^+}$	734895.06	0.5	6.5	5.1	2.8	177.46
$10_{3,0^-} \rightarrow 9_{2,0^-}$	735674.32	0.6	6.5	5.0	3.0	177.46
$10_{1,0^+} \rightarrow 9_{0,0^+}$	763953.80	0.8	6.8	5.5	4.5	141.08
$6_{2,0^-} \rightarrow 5_{1,0^-}$	766711.66	1.0	6.5	3.8	4.0	86.46
$16_{1,0^-} \rightarrow 15_{1,0^-}$	779006.31	0.4	7.9	4.2	1.9	332.65
$6_{2,0^+} \rightarrow 5_{1,0^+}$	779381.81	1.2	6.4	4.3	5.3	86.46
$11_{3,0^+} \rightarrow 10_{2,0^+}$	783002.74	0.4	6.6	4.1	1.9	202.98
$11_{3,0^-} \rightarrow 10_{2,0^-}$	784178.53	0.4	6.6	4.8	1.8	202.99
$11_{1,0^+} \rightarrow 10_{0,0^+}$	807866.57	0.6	6.8	5.2	3.1	166.37
$7_{2,0^-} \rightarrow 6_{1,0^-}$	812551.63	0.8	6.5	4.4	3.8	102.7
$4_{4,0^-} \rightarrow 3_{3,0^-}$	829891.72	0.7	6.9	4.6	3.1	103.56
$7_{2,0^+} \rightarrow 6_{1,0^+}$	830351.20	0.9	6.3	4.2	4.0	102.72
$12_{3,0^+} \rightarrow 11_{2,0^+}$	831048.06	0.3	5.9	4.4	1.4	230.83
$12_{3,0^-} \rightarrow 11_{2,0^-}$	832755.31	0.3	6.4	5.3	1.8	230.83
$12_{1,0^+} \rightarrow 11_{0,0^+}$	851415.12	0.6	7.0	4.7	3.0	193.96
$8_{2,0^-} \rightarrow 7_{1,0^-}$	857960.16	0.6	6.6	3.8	2.4	121.27
$5_{4,0^+} \rightarrow 4_{3,0^+}$	878227.11	0.6	6.8	4.5	2.7	115.16
$13_{3,0^+} \rightarrow 12_{2,0^+}$	879015.02	0.3	6.3	5.9	1.6	260.99
$13_{3,0^-} \rightarrow 12_{2,0^-}$	881420.97	0.3	6.9	6.6	1.8	261

A–CH_3OH

Transition J_{+K,v_t^π}	Frequency MHz	T_A (K)	V_{LSR} (km s^{-1})	ΔV_{FWHM} (km s^{-1})	$\int T_A dV$ (K km s^{-1})	E_u (K)
$8_{2,0^+} \rightarrow 7_{1,0^+}$	881783.47	0.7	6.5	4.5	3.6	121.29
$13_{1,0^+} \rightarrow 12_{0,0^+}$	894614.92	0.4	6.8	4.7	1.9	223.84
$13_{1,0^+} \rightarrow 12_{0,0^+}$	894614.92	0.4	6.8	4.7	1.9	223.84
$9_{2,0^-} \rightarrow 8_{1,0^-}$	902936.66	0.4	6.4	5.3	2.5	142.15
$6_{4,0^+} \rightarrow 5_{3,0^+}$	926555.20	0.4	7.0	5.3	2.5	129.09
$9_{2,0^+} \rightarrow 8_{1,0^+}$	933694.55	0.6	6.5	4.6	2.7	142.19
$14_{1,0^+} \rightarrow 13_{0,0^+}$	937479.55	0.3	6.6	5.8	2.0	256.02

Table 4
(Continued)

A–CH_3OH

Transition J_{+K,v_t^π}	Frequency MHz	T_A (K)	V_{LSR} (km s^{-1})	ΔV_{FWHM} (km s^{-1})	$\int T_A dV$ (K km s^{-1})	E_u (K)
$7_{4,0^-} \rightarrow 6_{3,0^-}$	974878.74	0.4	6.4	6.4	2.9	145.33
$10_{2,0^+} \rightarrow 9_{1,0^+}$	986100.37	0.5	6.2	5.1	3.0	165.4
$8_{4,0^+} \rightarrow 7_{3,0^+}$	1023196.73	0.5	7.2	4.4	2.2	163.9

E–CH_3OH

Transition $J_{\pm K,v_t}$	Frequency MHz	T_A (K)	V_{LSR} (km s^{-1})	ΔV_{FWHM} (km s^{-1})	$\int T_A dV$ (K km s^{-1})	E_u (K)
$10_{0,0} \rightarrow 9_{0,0}$	482283.13	0.7	6.4	3.8	2.8	132.71
$10_{-1,0} \rightarrow 9_{-1,0}$	482959.74	1.4	6.4	3.9	5.7	125.25
$10_{1,0} \rightarrow 9_{1,0}$	483687.10	0.5	6.5	3.9	2.2	140.83
$10_{2,0} \rightarrow 9_{2,0}$	484023.82	0.6	6.6	4.5	3.0	142.08
$10_{-2,0} \rightarrow 9_{-2,0}$	484072.13	0.3	6.8	5.0	1.6	145.73
$7_{0,0} \rightarrow 6_{-1,0}$	495173.84	1.2	6.6	3.9	4.8	70.18
$7_{1,0} \rightarrow 6_{0,0}$	504294.53	1.2	6.4	3.6	4.7	248.24
$11_{1,0} \rightarrow 10_{2,0}$	506153.78	0.2	6.6	5.1	1.0	166.37
$10_{2,0} \rightarrow 9_{1,0}$	509564.94	0.7	6.8	5.2	3.9	142.08
$2_{-2,0} \rightarrow 1_{-1,0}$	520179.58	1.1	6.7	4.1	5.0	24.96
$14_{-1,0} \rightarrow 13_{0,0}$	523275.25	0.3	6.5	4.9	1.4	241.04

E–CH_3OH

Transition $J_{\pm K,v_t}$	Frequency MHz	T_A (K)	V_{LSR} (km s^{-1})	ΔV_{FWHM} (km s^{-1})	$\int T_A dV$ (K km s^{-1})	E_u (K)
$8_{3,0} \rightarrow 8_{2,0}$	530123.52	0.3	6.9	5.4	1.7	123.38
$11_{0,0} \rightarrow 10_{0,0}$	530184.87	0.5	6.6	4.6	2.5	158.15
$7_{3,0} \rightarrow 7_{2,0}$	530316.84	0.3	6.6	4.9	1.8	104.81
$6_{3,0} \rightarrow 6_{2,0}$	530455.52	0.4	6.5	4.1	1.9	88.56
$5_{3,0} \rightarrow 5_{2,0}$	530549.77	0.4	6.7	4.6	2.2	74.63
$4_{3,0} \rightarrow 4_{2,0}$	530611.06	0.4	6.6	4.3	2.0	63.03
$3_{3,0} \rightarrow 3_{2,0}$	530647.07	0.4	7.1	5.0	2.1	53.74
$11_{-1,0} \rightarrow 10_{-1,0}$	531080.10	1.1	6.5	4.3	4.9	150.74
$11_{1,0} \rightarrow 10_{1,0}$	532032.12	0.4	6.6	5.2	2.2	166.37
$11_{2,0} \rightarrow 10_{2,0}$	532467.35	0.5	6.4	4.6	2.7	167.63
$11_{-2,0} \rightarrow 10_{-2,0}$	532567.79	0.3	6.4	5.2	1.7	171.29
$8_{0,0} \rightarrow 7_{-1,0}$	543076.99	1.1	6.6	4.5	5.2	88.72
$8_{1,0} \rightarrow 7_{0,0}$	553147.29	0.9	6.4	3.6	3.6	96.73
$11_{2,0} \rightarrow 10_{1,0}$	558345.87	0.4	6.3	4.3	1.9	167.63
$11_{2,0} \rightarrow 10_{1,0}$	558345.39	0.5	6.6	4.5	2.3	167.63
$3_{-2,0} \rightarrow 2_{-1,0}$	568566.84	1.2	6.6	4.3	5.6	31.93
$15_{-1,0} \rightarrow 14_{0,0}$	572900.17	0.2	6.2	5.0	1.2	275.74
$12_{0,0} \rightarrow 11_{0,0}$	578007.58	0.4	6.4	4.6	1.9	185.89
$12_{-1,0} \rightarrow 11_{-1,0}$	579151.93	0.7	6.5	4.4	3.5	178.53
$12_{1,0} \rightarrow 11_{1,0}$	580369.39	0.3	6.6	4.5	1.5	194.22
$12_{2,0} \rightarrow 11_{2,0}$	580903.85	0.4	6.4	4.9	2.2	195.51
$12_{-2,0} \rightarrow 11_{-2,0}$	581092.64	0.3	6.5	4.8	1.3	199.18
$9_{0,0} \rightarrow 8_{-1,0}$	590791.90	0.8	6.5	4.1	3.7	109.56
$9_{1,0} \rightarrow 8_{0,0}$	602234.23	0.8	6.4	4.0	3.4	117.62
$12_{2,0} \rightarrow 11_{1,0}$	607217.09	0.3	6.4	5.2	1.7	195.51
$4_{-2,0} \rightarrow 3_{-1,0}$	616980.70	1.2	6.6	4.1	5.1	41.22
$16_{-1,0} \rightarrow 15_{0,0}$	622775.50	0.2	6.1	5.0	1.0	312.73
$13_{0,0} \rightarrow 12_{0,0}$	625750.66	0.3	6.4	5.4	1.7	215.92
$13_{-1,0} \rightarrow 12_{-1,0}$	627171.60	0.6	6.5	4.9	3.0	208.64
$13_{1,0} \rightarrow 12_{1,0}$	628698.28	0.2	6.1	5.0	1.1	224.39

Table 4
(Continued)

E–CH_3OH

Transition $J_{\pm K,v_t}$	Frequency MHz	T_A (K)	V_{LSR} (km s^{-1})	ΔV_{FWHM} (km s^{-1})	$\int T_A dV$ (K km s^{-1})	E_u (K)
$13_{3,0} \rightarrow 12_{3,0}$	628817.62	0.2	6.3	4.0	0.8	251.06
$13_{2,0} \rightarrow 12_{2,0}$	629322.36	0.4	6.7	5.0	2.0	225.71
$13_{-2,0} \rightarrow 12_{-2,0}$	629653.22	0.2	6.3	7.8	1.9	229.4

E–CH_3OH

Transition $J_{\pm K,v_t}$	Frequency MHz	T_A (K)	V_{LSR} (km s^{-1})	ΔV_{FWHM} (km s^{-1})	$\int T_A dV$ (K km s^{-1})	E_u (K)
$13_{-1,0} \rightarrow 12_{-1,0}$	627171.35	0.5	6.6	4.4	2.3	208.64
$13_{2,0} \rightarrow 12_{2,0}$	629321.48	0.3	7.1	6.0	1.6	225.71
$13_{-2,0} \rightarrow 12_{-2,0}$	629651.72	0.2	7.0	5.2	1.1	229.4
$10_{0,0} \rightarrow 9_{-1,0}$	638280.27	0.7	6.7	4.4	3.1	132.71
$10_{1,0} \rightarrow 9_{0,0}$	651618.53	0.6	6.5	4.6	2.9	140.83
$13_{2,0} \rightarrow 12_{1,0}$	656166.61	0.6	8.1	6.4	3.8	225.71
$5_{-2,0} \rightarrow 4_{-1,0}$	665443.13	1.2	6.7	4.3	5.2	52.83
$14_{0,0} \rightarrow 13_{0,0}$	673416.97	0.3	6.6	4.9	1.4	248.24
$14_{-1,0} \rightarrow 13_{-1,0}$	675135.73	0.4	6.5	6.0	2.8	241.04
$3_{3,0} \rightarrow 2_{2,0}$	675773.95	0.7	6.8	4.9	3.6	53.74
$14_{1,0} \rightarrow 13_{1,0}$	677011.82	0.2	7.5	8.3	2.1	256.88
$14_{2,0} \rightarrow 13_{2,0}$	677711.91	0.3	6.1	4.9	1.7	258.24
$11_{0,0} \rightarrow 10_{-1,0}$	685505.14	0.5	7.0	5.9	3.2	158.15
$6_{-2,0} \rightarrow 5_{-1,0}$	713983.43	0.9	6.6	4.1	3.9	66.76
$6_{-2,0} \rightarrow 5_{-1,0}$	713983.43	0.9	6.6	4.1	3.9	66.76
$4_{-4,0} \rightarrow 3_{-3,0}$	718436.93	0.8	6.7	4.0	3.5	103.22
$15_{-1,0} \rightarrow 14_{-1,0}$	723040.58	0.4	6.9	5.4	2.0	275.74
$4_{3,0} \rightarrow 3_{2,0}$	724122.89	0.6	6.5	5.7	3.4	63.03
$4_{3,0} \rightarrow 3_{2,0}$	724122.10	0.8	6.8	5.3	4.2	63.03
$12_{0,0} \rightarrow 11_{-1,0}$	732433.68	0.4	6.4	5.1	2.2	185.89
$12_{1,0} \rightarrow 11_{0,0}$	751552.50	0.4	6.4	5.8	2.3	194.22
$7_{-2,0} \rightarrow 6_{-1,0}$	762636.47	0.7	6.7	4.4	3.4	83.02
$9_{-3,0} \rightarrow 9_{-2,0}$	766028.92	0.3	6.7	5.2	1.4	159.27
$8_{-3,0} \rightarrow 8_{-2,0}$	766396.97	0.4	6.6	5.9	2.3	138.38
$7_{-3,0} \rightarrow 7_{-2,0}$	766648.47	0.4	6.6	4.5	1.9	119.81
$5_{-4,0} \rightarrow 4_{-3,0}$	766761.68	0.8	6.6	3.3	2.9	114.82
$6_{-3,0} \rightarrow 6_{-2,0}$	766811.56	0.4	6.6	2.6	1.1	103.56
$5_{-3,0} \rightarrow 5_{-2,0}$	766908.51	0.4	6.8	4.2	1.9	89.63
$4_{-3,0} \rightarrow 4_{-2,0}$	766961.54	0.5	6.4	3.4	1.6	78.03

E–CH_3OH

Transition $J_{\pm K,v_t}$	Frequency MHz	T_A (K)	V_{LSR} (km s^{-1})	ΔV_{FWHM} (km s^{-1})	$\int T_A dV$ (K km s^{-1})	E_u (K)
$3_{-3,0} \rightarrow 3_{-2,0}$	766983.75	0.4	6.4	3.1	1.2	68.74
$5_{3,0} \rightarrow 4_{2,0}$	772453.48	0.5	7.2	7.1	4.0	74.63
$13_{0,0} \rightarrow 12_{-1,0}$	779030.27	0.4	7.2	6.0	2.2	215.92
$8_{-2,0} \rightarrow 7_{-1,0}$	811444.68	0.5	7.0	6.0	3.4	101.6
$6_{-4,0} \rightarrow 5_{-3,0}$	815071.72	0.7	6.6	4.3	3.1	128.75
$6_{3,0} \rightarrow 5_{2,0}$	820764.66	0.4	6.2	4.4	1.8	88.56
$9_{-2,0} \rightarrow 8_{-1,0}$	860459.44	0.4	7.0	5.5	2.4	122.5
$7_{-4,0} \rightarrow 6_{-3,0}$	863365.78	0.5	6.7	5.2	2.9	145
$7_{3,0} \rightarrow 6_{2,0}$	869039.06	0.5	6.6	5.2	2.6	104.81
$10_{-2,0} \rightarrow 9_{-1,0}$	909738.07	0.3	6.9	4.7	1.6	145.73

Table 4
(Continued)

E–CH_3OH

Transition $J_{\pm K,v_t}$	Frequency MHz	T_A (K)	V_{LSR} (km s^{-1})	ΔV_{FWHM} (km s^{-1})	$\int T_A dV$ (K km s^{-1})	E_u (K)
$8_{-4,0} \rightarrow 7_{-3,0}$	911643.69	0.4	6.5	4.5	2.1	163.56
$3_{-3,0} \rightarrow 2_{-2,0}$	912109.65	0.7	6.6	5.1	3.5	68.74
$8_{3,0} \rightarrow 7_{2,0}$	917269.03	0.4	7.3	4.9	1.9	123.38
$4_{-3,0} \rightarrow 3_{-2,0}$	960473.04	0.6	6.4	5.3	3.1	78.03

CN, v = 0

Transition $N_{J,F1}$	Frequency MHz	T_A (K)	V_{LSR} (km s^{-1})	ΔV_{FWHM} (km s^{-1})	$\int T_A dV$ (K km s^{-1})	E_u (K)
$5_{4.5,5.5} \rightarrow 4_{3.5,4.5}$	566729.48	1.3	7.3	5.3	7.3	81.59
$5_{5.5,5.5} \rightarrow 4_{4.5,4.5}$	566946.10	1.6	7.6	5.6	9.8	81.64
$6_{5.5,6.5} \rightarrow 5_{4.5,5.5}$	680046.29	0.5	7.5	5.4	3.0	114.23
$6_{6.5,6.5} \rightarrow 5_{5.5,5.5}$	680263.15	0.7	7.5	5.4	4.1	114.29
$7_{6.5,7.5} \rightarrow 6_{5.5,6.5}$	793337.05	0.3	7.3	6.9	2.2	152.38
$7_{7.5,7.5} \rightarrow 6_{6.5,6.5}$	793552.12	0.3	7.6	6.4	1.8	152.38

CO

	Transition J	Frequency MHz	T_A (K)	V_{LSR} (km s^{-1})	ΔV_{FWHM} (km s^{-1})	$\int T_A dV$ (K km s^{-1})	E_u (K)
Main	5 → 4	576267.41	52.5	7.3	6.3	352.5	82.98
Wing	5 → 4	576267.63	7.7	7.2	19.1	156.7	82.98
Main	6 → 5	691472.71	48.2	7.2	5.8	299.0	116.16
Wing	6 → 5	691472.71	11.9	7.2	17.6	222.7	116.16
Main	7 → 6	806653.11	46.6	6.5	5.0	248.5	154.88
Wing	7 → 6	806651.38	7.8	7.2	22.4	185.5	154.88
Main	8 → 7	921801.29	45.2	6.5	5.1	244.5	199.11
Wing	8 → 7	921799.21	7.3	7.2	23.8	184.5	199.11
Main	9 → 8	1036911.45	45.8	7.3	6.0	292.2	248.88
Wing	9 → 8	1036911.85	11.7	7.2	18.0	223.7	248.88
Main	10 → 9	1151987.56	39.3	6.5	4.6	194.1	304.17
Wing	10 → 9	1151987.37	5.5	6.5	23.0	134.4	304.17
Main	11 → 10	1267014.10	31.2	7.1	5.0	166.0	364.97
Wing	11 → 10	1267016.60	10.8	6.5	15.0	173.1	367.97
Main	13 → 12	1496920.46	29.8	7.5	4.8	152.8	503.14
Wing	13 → 12	1496925.41	8.7	6.5	18.2	167.9	503.14
Main	14 → 13	1611790.99	28.5	7.5	4.9	148.6	580.5
Wing	14 → 13	1611792.67	4.9	7.2	21.9	114.6	580.5
Main	15 → 14	1726597.84	20.4	7.8	3.5	75.5	663.36
Wing	15 → 14	1726601.59	6.2	7.2	14.0	92.3	663.36
Main	16 → 15	1841340.61	14.0	7.8	4.0	59.4	751.73
Wing	16 → 15	1841344.53	4.0	7.2	15.0	63.2	751.73

^{13}CO

Transition J	Frequency MHz	T_A (K)	V_{LSR} (km s^{-1})	ΔV_{FWHM} (km s^{-1})	$\int T_A dV$ (K km s^{-1})	E_u (K)
5 → 4	550925.82	30.9	7.3	4.8	157.6	79.33
6 → 5	661066.67	30.8	7.3	4.7	155.2	111.05
7 → 6	771182.86	28.0	7.5	5.1	152.0	148.06
8 → 7	881271.54	22.6	7.4	4.7	112.0	190.36
9 → 8	991327.01	17.5	7.7	4.7	87.8	237.94
10 → 9	1101346.80	13.1	7.8	4.6	64.4	290.79
11 → 10	1211327.07	6.7	7.6	4.3	31.0	348.93

$C^{18}O$

Transition J	Frequency MHz	T_A (K)	V_{LSR} (km s^{-1})	ΔV_{FWHM} (km s^{-1})	$\int T_A dV$ (K km s^{-1})	E_u (K)
5 → 4	548831.12	8.5	6.8	4.1	36.4	79.02
6 → 5	658553.65	8.0	6.9	3.7	31.5	110.63

Table 4
(Continued)

$C^{18}O$

Transition J	Frequency MHz	T_A (K)	V_{LSR} (km s^{-1})	ΔV_{FWHM} (km s^{-1})	$\int T_A dV$ (K km s^{-1})	E_u (K)
7 → 6	768252.15	5.8	7.0	4.1	25.4	147.5
8 → 7	877922.54	3.5	6.9	5.0	18.7	189.64
9 → 8	987559.09	2.2	7.6	5.9	13.8	237.03
10 → 9	1097163.80	1.5	6.8	3.2	5.1	289.69

$C^{17}O$

Transition J	Frequency MHz	T_A (K)	V_{LSR} (km s^{-1})	ΔV_{FWHM} (km s^{-1})	$\int T_A dV$ (K km s^{-1})	E_u (K)
5 → 4	561713.01	3.0	6.7	3.7	11.9	80.88
6 → 5	674009.48	2.4	6.6	3.7	9.3	113.23
7 → 6	786282.9[b]	…	6.5	4.5	7.6	150.96
8 → 7	898523.38	0.9	7.0	4.1	4.0	194.09
9 → 8	1010731.41	0.4	7.2	3.5	1.5	242.59
10 → 9	1122902.89	0.2	7.4	4.2	1.1	296.49

$^{13}C^{18}O$

Transition J	Frequency MHz	T_A (K)	V_{LSR} (km s^{-1})	ΔV_{FWHM} (km s^{-1})	$\int T_A dV$ (K km s^{-1})	E_u (K)
5 → 4	523484.35	0.1	6.9	4.1	0.6	75.37
6 → 5	628141.57	0.1	6.6	2.6	0.3	105.52

CS, v = 0

	Transition J	Frequency MHz	T_A (K)	V_{LSR} (km s^{-1})	ΔV_{FWHM} (km s^{-1})	$\int T_A dV$ (K km s^{-1})	E_u (K)
Main	10 → 9	489750.85	4.1	7.3	4.3	18.8	129.29
Wing	10 → 9	489750.92	0.6	6.7	7.8	4.6	129.29
Main	11 → 10	538688.84	3.3	7.2	4.7	16.5	155.15
Wing	11 → 10	538688.92	0.3	7.0	16.9	4.5	155.15
Main	12 → 11	587616.41	2.2	7.1	4.9	11.2	183.35
Wing	12 → 11	587619.04	0.2	6.5	12.9	2.4	183.35
Main	13 → 12	636532.25	1.0	7.2	5.3	5.8	213.9
Wing	13 → 12	636531.41	0.2	8.0	15.0	3.9	213.9
Main	14 → 13	685435.93	1.0	7.0	6.0	6.6	246.79
Wing	14 → 13	…	…	…	…	…	246.79
Main	15 → 14	734325.78	0.6	6.7	5.1	3.1	282.04
Wing	15 → 14	734327.70	0.2	6.5	20.4	4.8	282.04
Main	16 → 15	783201.36	0.3	7.2	5.0	1.4	319.62
Wing	16 → 15	783203.40	0.3	7.0	10.3	2.9	319.62
Main	17 → 16	832061.55	0.4	6.6	6.1	2.9	359.56
Wing	17 → 16	…	…	…	…	…	359.56
Main	18 → 17	880903.85	0.3	7.2	9.0	2.9	401.83
Wing	18 → 17	…	…	…	…	…	401.83

^{13}CS

Transition J	Frequency MHz	T_A (K)	V_{LSR} (km s^{-1})	ΔV_{FWHM} (km s^{-1})	$\int T_A dV$ (K km s^{-1})	E_u (K)
11 → 10	508535.83	0.1	7.1	6.1	0.5	146.46

$C^{34}S$

Transition J	Frequency MHz	T_A (K)	V_{LSR} (km s^{-1})	ΔV_{FWHM} (km s^{-1})	$\int T_A dV$ (K km s^{-1})	E_u (K)
10 → 9	481916.67	0.3	6.8	4.6	1.4	127.23
11 → 10	530071.15	0.2	7.5	5.3	1.0	152.67

Table 4
(Continued)

$C^{34}S$

Transition J	Frequency MHz	T_A (K)	V_{LSR} (km s^{-1})	ΔV_{FWHM} (km s^{-1})	$\int T_A dV$ (K km s^{-1})	E_u (K)
$12 \rightarrow 11$	578215.88	0.2	7.6	7.3	1.3	180.42

DCN, v = 0

Transition N_k	Frequency MHz	T_A (K)	V_{LSR} (km s^{-1})	ΔV_{FWHM} (km s^{-1})	$\int T_A dV$ (K km s^{-1})	E_u (K)
$7_0 \rightarrow 6_0$	506825.63	0.2	6.9	5.2	1.0	97.3

DCO^+

Transition J	Frequency MHz	T_A (K)	V_{LSR} (km s^{-1})	ΔV_{FWHM} (km s^{-1})	$\int T_A dV$ (K km s^{-1})	E_u (K)
$7 \rightarrow 6$	504200.27	0.2	7.1	4.4	0.8	96.80
$8 \rightarrow 7$	576205.0[b]	…	…	…	…	124.45
$9 \rightarrow 8$	648195.15	0.2	6.1	2.1	0.4	155.56

o–H_2S

Transition $J_{\Omega,\Lambda}$	Frequency MHz	T_A (K)	V_{LSR} (km s^{-1})	ΔV_{FWHM} (km s^{-1})	$\int T_A dV$ (K km s^{-1})	E_u (K)
$2_{2,1} \rightarrow 2_{1,2}$	505565.22	1.5	7.0	5.0	8.2	59.59
$3_{1,2} \rightarrow 3_{0,3}$	708470.60	0.4	6.9	7.5	3.5	116.99
$2_{1,2} \rightarrow 1_{0,1}$	736034.21	4.5	7.4	5.9	27.9	35.32
$3_{0,3} \rightarrow 2_{1,2}$	993107.06	1.7	5.8	6.3	11.4	82.99
$2_{2,1} \rightarrow 1_{1,0}$	1072837.04	0.9	7.7	6.0	5.7	59.59

p–H_2S

Transition $J_{\Omega,\Lambda}$	Frequency MHz	T_A (K)	V_{LSR} (km s^{-1})	ΔV_{FWHM} (km s^{-1})	$\int T_A dV$ (K km s^{-1})	E_u (K)
$2_{0,2} \rightarrow 1_{1,1}$	687303.34	2.4	7.1	5.1	12.7	54.7
$3_{1,3} \rightarrow 2_{0,2}$	1002777.30	0.6	7.4	5.6	3.8	102.82

$H_2^{34}S$

Transition N_{K_a,K_c}	Frequency MHz	T_A (K)	V_{LSR} (km s^{-1})	ΔV_{FWHM} (km s^{-1})	$\int T_A dV$ (K km s^{-1})	E_u (K)
$2_{1,2} \rightarrow 1_{0,1}$	734269.67	0.3	6.9	4.1	1.3	55.01

H_2CS

Transition J_{K_a,K_c}	Frequency MHz	T_A (K)	V_{LSR} (km s^{-1})	ΔV_{FWHM} (km s^{-1})	$\int T_A dV$ (K km s^{-1})	E_u (K)
$14_{1,13} \rightarrow 13_{1,12}$	487664.03	0.2	6.8	4.5	0.8	188.8
$15_{1,15} \rightarrow 14_{1,14}$	506771.50	0.2	6.6	5.2	1.1	207.86
$15_{0,15} \rightarrow 14_{0,14}$	513361.94	0.1	6.6	4.0	0.4	197.44
$15_{2,13} \rightarrow 14_{2,12}$	516336.1[b]	…	…	…	…	250.71
$15_{1,14} \rightarrow 14_{1,13}$	522403.63	0.1	6.9	5.1	0.9	213.87
$16_{1,16} \rightarrow 15_{1,15}$	540465.31	0.1	6.5	3.5	0.5	233.79
$17_{1,17} \rightarrow 16_{1,16}$	574140.12	0.1	6.8	4.7	0.5	261.35

HF

Transition J	Frequency MHz	T_A (K)	V_{LSR} (km s^{-1})	ΔV_{FWHM} (km s^{-1})	$\int T_A dV$ (K km s^{-1})	E_u (K)
$1 \rightarrow 0$	1232469.17	−1.1	8.7	3.2	−7.0	59.15

o–H_2CO

Transition J_{K_a,K_c}	Frequency MHz	T_A (K)	V_{LSR} (km s^{-1})	ΔV_{FWHM} (km s^{-1})	$\int T_A dV$ (K km s^{-1})	E_u (K)
$7_{1,7} \rightarrow 6_{1,6}$	491968.45	3.1	7.0	4.4	14.7	91.15

Table 4
(Continued)

o–H_2CO

Transition J_{K_a,K_c}	Frequency MHz	T_A (K)	V_{LSR} (km s^{-1})	ΔV_{FWHM} (km s^{-1})	$\int T_A dV$ (K km s^{-1})	E_u (K)
$7_{5,3} \rightarrow 6_{5,2}$	509562.12[b]	...	...	...	...	376.68
$7_{3,5} \rightarrow 6_{3,4}$	510155.94	0.9	6.9	4.8	4.4	188.73
$7_{3,4} \rightarrow 6_{3,3}$	510238.04	0.9	6.9	4.4	4.0	188.73
$7_{1,6} \rightarrow 6_{1,5}$	525666.11	2.5	6.8	4.6	12.2	97.63
$8_{1,8} \rightarrow 7_{1,7}$	561899.30	2.6	7.0	4.4	12.5	118.12
$8_{5,3} \rightarrow 7_{5,2}$	582382.77	0.2	6.6	6.3	1.3	404.63
$8_{3,6} \rightarrow 7_{3,5}$	583144.85	0.6	6.9	5.2	3.2	216.71
$8_{3,5} \rightarrow 7_{3,4}$	583308.64	0.6	7.0	4.6	2.8	216.73
$8_{1,7} \rightarrow 7_{1,6}$	600331.09	1.7	6.7	4.5	8.1	126.44
$9_{1,9} \rightarrow 8_{1,8}$	631703.48	1.5	6.7	4.6	7.3	148.43
$9_{5,5} \rightarrow 8_{5,4}$	655212.67	0.2	6.7	5.4	1.1	436.08
$9_{3,7} \rightarrow 8_{3,6}$	656166.83	0.6	6.0	6.2	3.9	248.2
$9_{3,6} \rightarrow 8_{3,5}$	656465.35	0.5	6.6	4.6	2.3	248.23
$9_{1,8} \rightarrow 8_{1,7}$	674810.63	1.1	6.6	4.8	5.4	158.83
$10_{1,10} \rightarrow 9_{1,9}$	701370.13	1.3	7.1	5.1	7.1	182.1
$10_{5,6} \rightarrow 9_{5,5}$	728052.29	0.2	7.5	5.1	1.0	471.02
$10_{3,8} \rightarrow 9_{3,7}$	729213.26	0.4	6.7	4.5	2.0	283.2
$10_{3,7} \rightarrow 9_{3,6}$	729725.77	0.3	6.7	5.9	2.1	283.25
$10_{1,9} \rightarrow 9_{1,8}$	749072.76	0.8	6.7	4.5	3.8	194.78
$11_{1,11} \rightarrow 10_{1,10}$	770895.15	0.7	7.4	7.7	5.7	219.09
$11_{1,10} \rightarrow 10_{1,9}$	823084.31	0.5	6.4	5.1	2.8	234.28
$12_{1,12} \rightarrow 11_{1,11}$	840277.03	0.5	6.5	4.8	2.5	259.42
$12_{1,11} \rightarrow 11_{1,10}$	896807.59	0.3	6.2	4.9	1.7	277.32
$13_{1,13} \rightarrow 12_{1,12}$	909511.04	0.3	5.9	6.0	2.0	303.07

p–H_2CO

Transition J_{K_a,K_c}	Frequency MHz	T_A (K)	V_{LSR} (km s^{-1})	ΔV_{FWHM} (km s^{-1})	$\int T_A dV$ (K km s^{-1})	E_u (K)
$7_{0,7} \rightarrow 6_{0,6}$	505834.17	1.7	6.7	4.0	7.2	97.44
$7_{2,6} \rightarrow 6_{2,5}$	509146.74	0.8	6.7	4.2	3.4	144.93
$7_{4,4} \rightarrow 6_{4,3}$	509830.59	0.2	6.4	4.2	1.0	286.17
$7_{2,5} \rightarrow 6_{2,4}$	513076.79	0.7	6.7	4.5	3.2	145.35
$8_{0,8} \rightarrow 7_{0,7}$	576709.19	1.1	6.6	4.2	4.9	125.12
$8_{2,7} \rightarrow 7_{2,6}$	581612.27	0.5	6.8	4.3	2.3	172.84
$8_{4,5} \rightarrow 7_{4,4}$	582723.54	0.2	6.7	5.7	1.2	314.14
$8_{2,6} \rightarrow 7_{2,5}$	587454.12	0.5	6.8	4.8	2.4	173.55
$9_{0,9} \rightarrow 8_{0,8}$	647082.69	0.9	6.6	4.1	3.7	156.18
$9_{2,8} \rightarrow 8_{2,7}$	653971.43	0.4	6.4	4.6	1.9	204.23
$9_{4,6} \rightarrow 8_{4,5}$	655640.45	0.2	6.8	6.0	1.2	345.6
$9_{2,7} \rightarrow 8_{2,6}$	662209.75	0.4	6.7	4.5	1.9	205.33
$10_{0,10} \rightarrow 9_{0,9}$	716939.12	0.4	6.7	5.6	2.4	190.58
$10_{2,9} \rightarrow 9_{2,8}$	726209.22	0.3	6.6	6.5	2.0	239.08
$10_{2,8} \rightarrow 9_{2,7}$	737342.68	0.3	7.0	5.3	1.7	380.57
$11_{0,11} \rightarrow 10_{0,10}$	786282.9[b]	...	6.5	4.5	7.6	228.32

o–H_2O

	Transition $J_{K_{-1},K_{+1}}$	Frequency MHz	T_A (K)	V_{LSR} (km s^{-1})	ΔV_{FWHM} (km s^{-1})	$\int T_A dV$ (K km s^{-1})	E_u (K)
Main	$1_{1,0} \rightarrow 1_{0,1}$	556935.64	6.2	7.2	7.8	51.9	26.73
Wing	$1_{1,0} \rightarrow 1_{0,1}$	556939.86	1.4	4.9	34.3	52.1	26.73
Main	$5_{3,2} \rightarrow 4_{4,1}$	620704.48	0.5	5.3	2.0	1.1	697.84
Wing	$5_{3,2} \rightarrow 4_{4,1}$	620704.48	...	...	...	...	697.84

Table 4
(Continued)

o–H_2O							
	Transition $J_{K_{-1},K_{+1}}$	Frequency MHz	T_A (K)	V_{LSR} (km s^{-1})	ΔV_{FWHM} (km s^{-1})	$\int T_A dV$ (K km s^{-1})	E_u (K)
Main	$3_{1,2} \rightarrow 3_{0,3}$	1097364.47	1.5	7.1	5.1	8.2	215.2
Wing	$3_{1,2} \rightarrow 3_{0,3}$	1097371.43	2.0	5.2	14.8	31.2	215.2
Main	$3_{1,2} \rightarrow 2_{2,1}$	1153127.12	1.6	6.9	5.3	8.9	215.203
Wing	$3_{1,2} \rightarrow 2_{2,1}$	1153133.21	2.6	5.3	19.2	53.7	215.2
Main	$3_{2,1} \rightarrow 3_{1,2}$	1162913.04	2.9	6.6	4.3	13.4	271.01
Wing	$3_{2,1} \rightarrow 3_{1,2}$	1162914.76	1.4	6.2	18.6	28.4	271.01
p–H_2O							
	Transition $J_{K_{-1},K_{+1}}$	Frequency MHz	T_A (K)	V_{LSR} (km s^{-1})	ΔV_{FWHM} (km s^{-1})	$\int T_A dV$ (K km s^{-1})	E_u (K)
Main	$2_{1,1} \rightarrow 2_{0,2}$	752033.42	5.5	6.9	5.8	33.6	136.94
Wing	$2_{1,1} \rightarrow 2_{0,2}$	752034.00	2.5	6.7	21.8	58.8	136.94
Main	$4_{2,2} \rightarrow 3_{3,1}$	916174.82	0.3	5.9	6.9	2.0	454.34
Wing	$4_{2,2} \rightarrow 3_{3,1}$	916174.82	…	…	…	…	454.34
Main	$2_{0,2} \rightarrow 1_{1,1}$	987927.13	6.1	6.9	7.5	48.6	100.85
Wing	$2_{0,2} \rightarrow 1_{1,1}$	987938.36	2.4	3.5	26.2	66.2	100.85
Main	$1_{1,1} \rightarrow 0_{0,0}$	1113349.92	1.9	5.1	4.5	9.1	53.43
Wing	$1_{1,1} \rightarrow 0_{0,0}$	1113352.60	1.8	4.4	22.3	42.8	53.43
Main	$4_{2,2} \rightarrow 4_{1,3}$	1207638.86	0.3	7.0	13.6	4.2	454.34
Wing	$4_{2,2} \rightarrow 4_{1,3}$	1207638.86	…	…	…	…	454.34
Main	$2_{2,0} \rightarrow 2_{1,1}$	1228791.19	1.2	6.4	5.4	7.2	195.91
Wing	$2_{2,0} \rightarrow 2_{1,1}$	1228791.19	…	…	…	…	195.91
	$1_{1,0,0} \rightarrow 1_{0,1,0}$	547676.36	0.2	7.0	5.6	1.43	
HDO							
	Transition $J_{K_{-1},K_{+1}}$	Frequency MHz	T_A (K)	V_{LSR} (km s^{-1})	ΔV_{FWHM} (km s^{-1})	$\int T_A dV$ (K km s^{-1})	E_u (K)
	$2_{0,2} \rightarrow 1_{1,1}$	490597.00	0.2	6.8	3.9	0.7	66.43
	$1_{1,0} \rightarrow 1_{1,1}$	509293.66	0.3	6.3	3.4	1.0	46.76
	$2_{1,1} \rightarrow 2_{0,2}$	599927.69	0.2	6.5	2.9	0.7	95.23
HCl							
	Transition N_J	Frequency MHz	T_A (K)	V_{LSR} (km s^{-1})	ΔV_{FWHM} (km s^{-1})	$\int T_A dV$ (K km s^{-1})	E_u (K)
	$1_{1.5} \rightarrow 0_{1.5}$	625901.60	2.1	7.8	4.4	9.9	30.04
	$1_{2.5} \rightarrow 0_{1.5}$	625918.76	2.8	7.9	4.1	12.0	30.04
	$1_{0.5} \rightarrow 0_{1.5}$	625932.01	1.4	7.9	4.7	7.0	30.04
$H^{37}Cl$							
	Transition N_J	Frequency MHz	T_A (K)	V_{LSR} (km s^{-1})	ΔV_{FWHM} (km s^{-1})	$\int T_A dV$ (K km s^{-1})	E_u (K)
	$1_{1.5} \rightarrow 0_{1.5}$	624962.48	1.0	8.3	3.1	3.1	29.99
	$1_{2.5} \rightarrow 0_{1.5}$	624975.93	1.4	8.1	3.8	5.5	29.99
	$1_{0.5} \rightarrow 0_{1.5}$	624986.44	0.6	8.8	5.4	3.6	29.99
HCN							
	Transition J	Frequency MHz	T_A (K)	V_{LSR} (km s^{-1})	ΔV_{FWHM} (km s^{-1})	$\int T_A dV$ (K km s^{-1})	E_u (K)
Main	$6 \rightarrow 5$	531716.10	7.4	7.1	5.4	43.0	89.32
Wing	$6 \rightarrow 5$	531718.60	0.5	6.0	25.3	14.0	89.32
Main	$7 \rightarrow 6$	620303.70	5.1	7.2	5.3	28.4	119.09
Wing	$7 \rightarrow 6$	620305.69	0.8	5.9	17.1	14.3	119.09
Main	$8 \rightarrow 7$	708876.27	2.5	7.4	5.2	13.8	153.11

Table 4
(Continued)

HCN

	Transition J	Frequency MHz	T_A (K)	V_{LSR} (km s^{-1})	ΔV_{FWHM} (km s^{-1})	$\int T_A dV$ (K km s^{-1})	E_u (K)
Wing	8 → 7	708878.31	0.9	6.2	16.0	15.0	153.11
Main	9 → 8	797432.27	0.9	7.6	4.9	4.9	191.38
Wing	9 → 8	797435.00	0.8	6.3	13.5	11.2	191.38
Main	10 → 9	885969.75	0.6	7.4	5.7	3.9	233.9
Wing	10 → 9	885973.43	0.6	6.3	16.0	10.2	233.9
Main	11 → 10	974486.55	0.6	6.5	5.5	3.5	280.67
Wing	11 → 10	…	…	…	…	…	280.67
Main	13 → 12	1151448.54	0.5	5.9	6.2	3.0	386.95
Wing	13 → 12	…	…	…	…	…	386.95

$H^{13}CN$

Transition J	Frequency MHz	T_A (K)	V_{LSR} (km s^{-1})	ΔV_{FWHM} (km s^{-1})	$\int T_A dV$ (K km s^{-1})	E_u (K)
6 → 5	517969.24	0.4	7.3	5.0	2.1	87.01
7 → 6	604266.38	0.2	7.8	7.5	1.7	116.01

HNC

Transition J_{K_a,K_c}	Frequency MHz	T_A (K)	V_{LSR} (km s^{-1})	ΔV_{FWHM} (km s^{-1})	$\int T_A dV$ (K km s^{-1})	E_u (K)
$6_{0,0} \rightarrow 5_{0,0}$	543897.76	1.2	7.0	4.2	5.4	91.37
$7_{0,0} \rightarrow 6_{0,0}$	634510.41	0.5	7.2	4.5	2.2	121.82

HCO^+

Transition J	Frequency MHz	T_A (K)	V_{LSR} (km s^{-1})	ΔV_{FWHM} (km s^{-1})	$\int T_A dV$ (K km s^{-1})	E_u (K)
6 → 5	535061.20	15.3	7.2	5.5	90.3	89.88
7 → 6	624208.34	13.8	7.0	5.7	83.7	119.84
8 → 7	713341.48	10.5	6.9	5.3	59.4	154.08
9 → 8	802458.39	7.4	6.9	5.2	41.0	192.59
10 → 9	891558.14	5.6	6.7	5.2	31.2	235.38
11 → 10	980636.88	4.2	6.9	5.3	23.8	282.44
12 → 11	1069695.54	2.5	6.5	5.2	14.0	333.78
13 → 12	1158729.89	1.6	6.3	4.7	7.9	389.39
14 → 13	1247737.53	0.9	6.4	5.0	5.0	449.27

$H^{13}CO^+$

Transition J	Frequency MHz	T_A (K)	V_{LSR} (km s^{-1})	ΔV_{FWHM} (km s^{-1})	$\int T_A dV$ (K km s^{-1})	E_u (K)
6 → 5	520460.32	1.1	6.7	3.9	4.6	87.43
7 → 6	607175.53	0.7	6.7	3.7	2.7	116.57
8 → 7	693877.57	0.4	6.4	3.4	1.6	149.87
9 → 8	780563.19	0.2	6.9	5.5	1.3	187.33

N_2H^+

Transition J	Frequency MHz	T_A (K)	V_{LSR} (km s^{-1})	ΔV_{FWHM} (km s^{-1})	$\int T_A dV$ (K km s^{-1})	E_u (K)
6 → 5	558967.76	2.7	6.3	0.1	7.2	93.9
7 → 6	652097.23	2.7	6.3	0.0	6.7	125.19
8 → 7	745211.80	1.6	6.3	0.1	3.7	160.96

Table 4
(Continued)

N_2H^+

Transition J	Frequency MHz	T_A (K)	V_{LSR} (km s^{-1})	ΔV_{FWHM} (km s^{-1})	$\int T_A dV$ (K km s^{-1})	E_u (K)
$9 \rightarrow 8$	838309.70	0.9	6.2	0.2	1.8	201.19
$10 \rightarrow 9$	931388.75	0.5	6.0	0.3	1.3	245.89

NH_3

	Transition $N_{K,v}$	Frequency MHz	T_A (K)	V_{LSR} (km s^{-1})	ΔV_{FWHM} (km s^{-1})	$\int T_A dV$ (K km s^{-1})	E_u (K)
Main	$1_{0,0} \rightarrow 0_{0,1}$	572498.04	3.3	7.1	5.9	20.8	27.48
Wing	$1_{0,0} \rightarrow 0_{0,1}$	572496.26	0.2	7.5	12.0	2.1	27.48
Absorption	$2_{1,1} \rightarrow 1_{1,0}$	1215245.71	−0.7	6.5	5.1	−3.9	80.45

NO

Transition $N_{\Lambda F_1 F_2}$	Frequency MHz	T_A (K)	V_{LSR} (km s^{-1})	ΔV_{FWHM} (km s^{-1})	$\int T_A dV$ (K km s^{-1})	E_u (K)
$6_{-1,5.5,5.5} \rightarrow 5_{1,4.5,4.5}$	551187.85	0.3	6.7	4.6	1.5	84.15
$6_{1,5.5,4.5} \rightarrow 5_{-1,4.5,3.5}$	551533.80	0.3	7.1	4.8	1.4	84.25
$6_{1,6.5,6.5} \rightarrow 6_{-1,5.5,5.5}$	651433.16	0.3	6.8	5.8	1.7	115.42
$6_{-1,6.5,5.5} \rightarrow 6_{1,5.5,4.5}$	651773.27	0.4	6.9	4.3	1.7	115.53

SO

Transition N_J	Frequency MHz	T_A (K)	V_{LSR} (km s^{-1})	ΔV_{FWHM} (km s^{-1})	$\int T_A dV$ (K km s^{-1})	E_u (K)
$4_3 \rightarrow 1_2$	504676.68	0.1	6.8	3.8	0.5	28.68
$12_{11} \rightarrow 11_{10}$	514853.39	0.7	7.2	6.7	4.7	167.59
$12_{12} \rightarrow 11_{11}$	516335.63	0.6	7.1	7.6	5.1	174.22
$12_{13} \rightarrow 11_{12}$	517354.09	0.8	7.3	6.4	5.7	165.78
$13_{12} \rightarrow 12_{11}$	558087.15	0.4	7.3	5.9	2.4	194.37
$13_{13} \rightarrow 12_{12}$	559319.68	0.4	7.0	6.6	2.7	201.07
$13_{14} \rightarrow 12_{13}$	560178.46	0.5	7.1	5.7	2.7	192.66
$14_{13} \rightarrow 13_{12}$	601257.88	0.4	7.3	9.6	3.7	223.23
$14_{14} \rightarrow 13_{13}$	602291.95	0.3	7.5	9.0	3.2	229.97
$14_{15} \rightarrow 13_{14}$	603021.65	0.4	7.0	8.2	3.5	221.61
$5_4 \rightarrow 2_3$	611551.86	0.1	7.3	3.7	0.4	38.58
$15_{14} \rightarrow 14_{13}$	644377.53	0.3	7.7	9.0	3.3	254.15
$15_{15} \rightarrow 14_{14}$	645253.67	0.3	7.6	9.0	2.8	260.94
$15_{16} \rightarrow 14_{15}$	645874.95	0.3	7.5	10.5	3.8	252.6
$16_{15} \rightarrow 15_{14}$	687457.56	0.3	7.1	12.6	3.4	287.15
$16_{16} \rightarrow 15_{15}$	688204.39	0.2	7.1	10.5	2.7	293.97
$16_{17} \rightarrow 15_{16}$	688733.81	0.3	7.8	14.9	4.0	285.66
$17_{16} \rightarrow 16_{15}$	730500.26	0.3	7.2	7.5	2.2	322.2

SO_2

Transition N_{K_a,K_c}	Frequency MHz	T_A (K)	V_{LSR} (km s^{-1})	ΔV_{FWHM} (km s^{-1})	$\int T_A dV$ (K km s^{-1})	E_u (K)
$13_{3,11} \rightarrow 12_{2,10}$	484270.75	0.2	7.1	4.0	0.6	105.83
$7_{4,4} \rightarrow 6_{3,3}$	491933.52	0.1	7.7	5.4	0.8	65.01
$12_{3,9} \rightarrow 11_{2,10}$	494779.07	0.2	7.4	3.3	0.7	93.96

Note. Superscipt "b" means it is a blended line and excluded.

the CDMS and JPL websites). The centroid frequency of the fitted Gaussian profile is listed in the second column. T_A and V_{LSR} are, respectively, the observed antenna temperature and centroid velocity of the corresponding Gaussian fit. ΔV_{FWHM} is the "Full Width Half Maximum," and $\int T_A dV$ (km s^{-1}) is the integrated line intensity.

Note that Gaussian fitting was performed on each line separately (i.e., we did not utilize a single set of Gaussian parameters to fit all transitions simultaneously). This implies that each transition of a given species can have slightly different V_{LSR} and ΔV_{FWHM}. This effect is best demonstrated using methanol as an example, since it has the largest number of

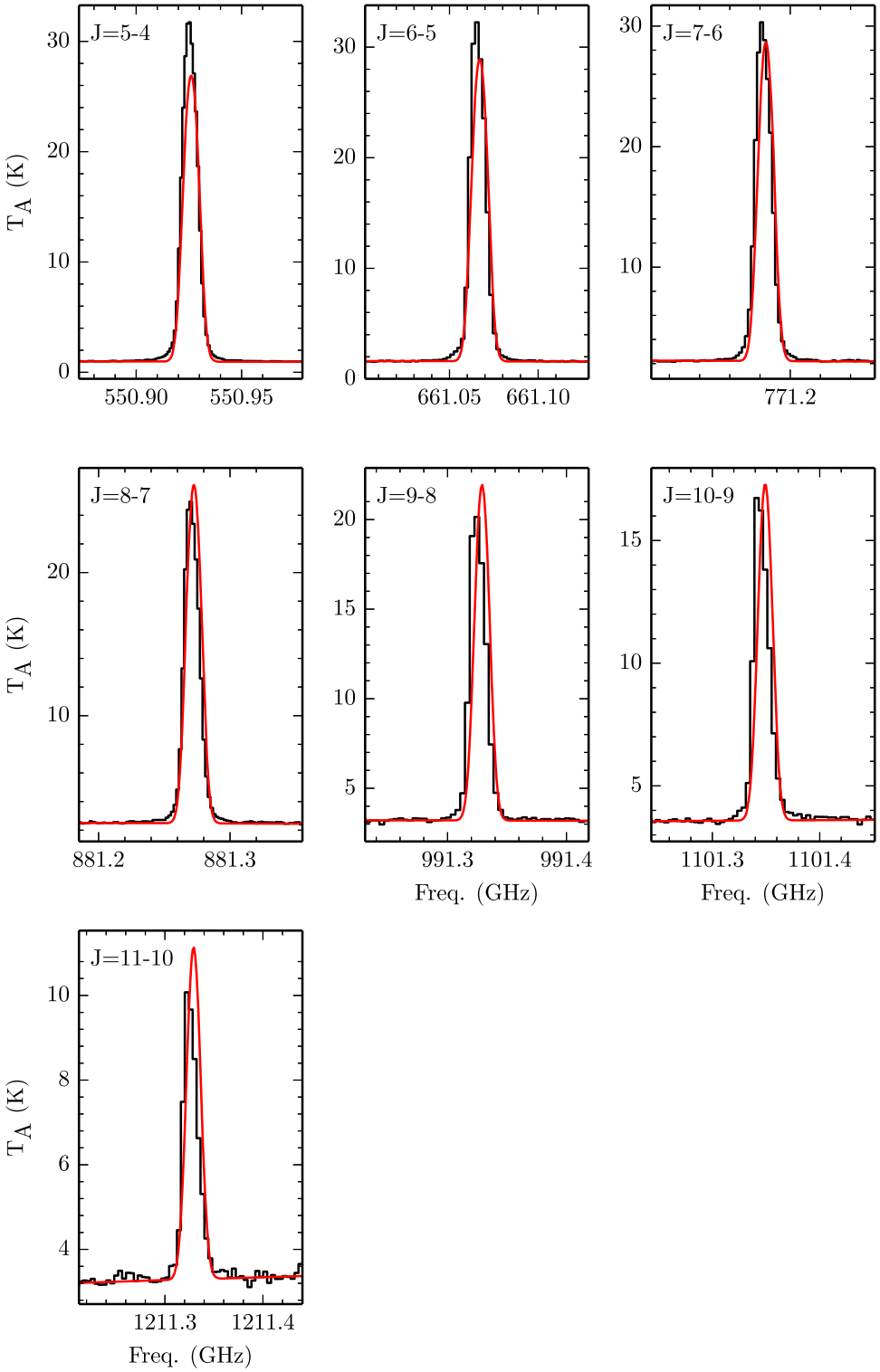

Figure 9. One-component LTE modeling for ^{13}CO. The black histogram shows the data. Resulting model spectra are shown in red. LTE model parameters are provided in Table 5.

transitions. The mean values of $V_{\rm LSR}$ and $\Delta V_{\rm FWHM}$ for methanol A and E combined is $6.6 \pm 0.3\,{\rm km\,s^{-1}}$ and $4.7 \pm 0.9\,{\rm km\,s^{-1}}$, respectively, where the errors are the 1σ standard deviations about the mean. The calculated scatter about the mean, however, is an intensity dependent parameter. Figures 11 and 12 plot $V_{\rm LSR}$ and $\Delta V_{\rm FWHM}$ versus $T_{\rm A}$ ($>5\sigma$) for all the fitted methanol A and E transitions in Table 4, and clearly show that the scatter in both fitted parameters decreases with increasing $T_{\rm A}$. For transitions with $T_{\rm A} < 0.5\,{\rm K}$, $\langle {\rm V_{LSR}} \rangle = 6.59 \pm 0.39$ km s^{-1} and $\langle \Delta V_{\rm FWHM} \rangle = 4.99 \pm 0.92\,{\rm km\,s^{-1}}$. Whereas, for transitions with $T_{\rm A} > 0.5\,{\rm K}$, $\langle {\rm V_{LSR}} \rangle = 6.57 \pm 0.23$ km s^{-1} and $\langle \Delta V_{\rm FWHM} \rangle = 4.39 \pm 0.67\,{\rm km\,s^{-1}}$. This suggests that most of the observed scatter in these parameters is not due to the emission itself but it is due to our Gaussian fitting procedure,

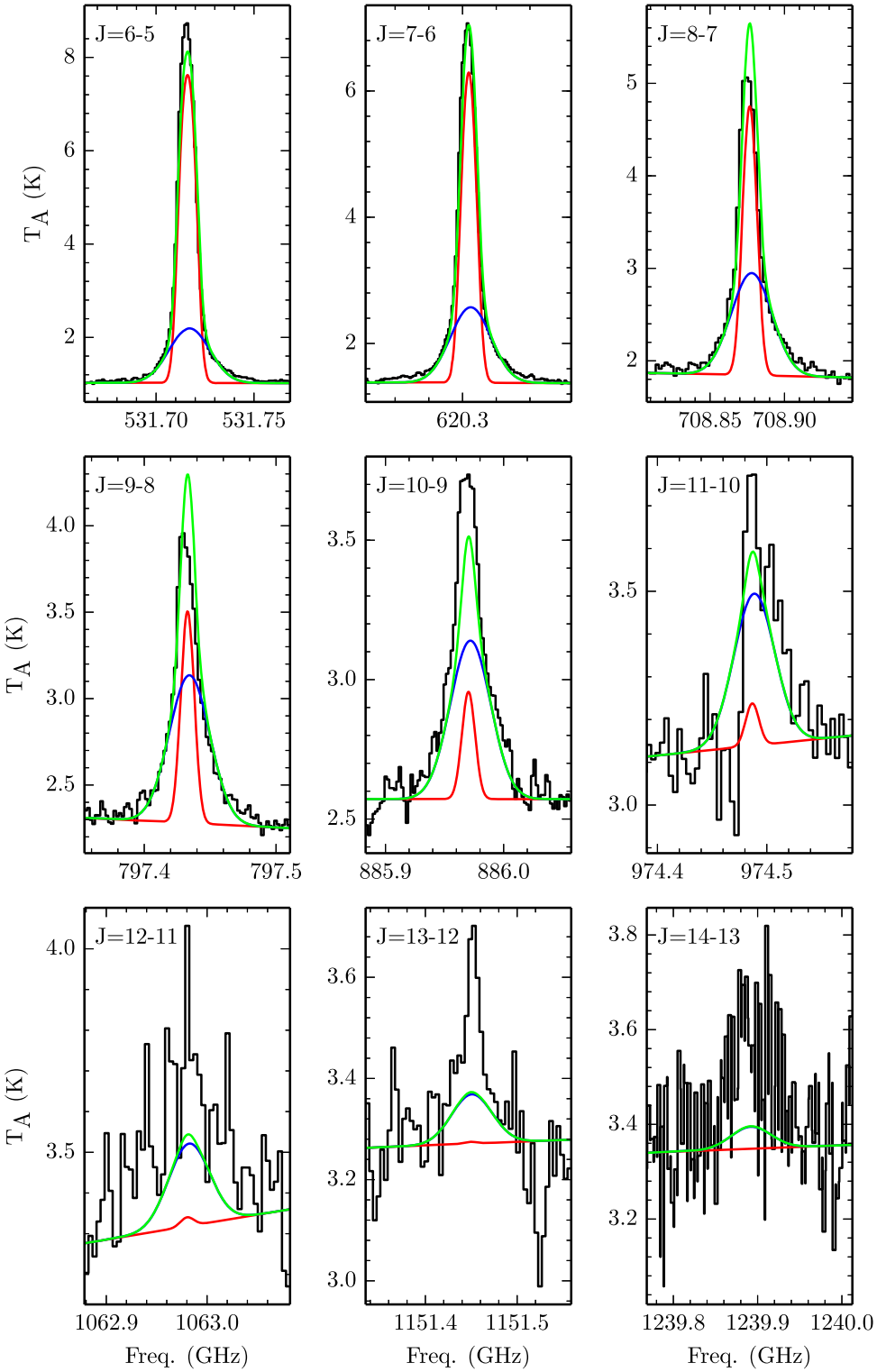

Figure 10. Two component LTE modeling for HCN. The black histogram shows the data. Models of the narrow and the broad components are shown by the red and blue lines respectively. The superposition of the two components is shown in green. LTE model parameters are provided in Table 6.

which clearly is subject to larger errors for weaker lines. This behavior is predicted by Porter et al. (2004) who show that the error in $V_{\rm LSR}$ and $\Delta V_{\rm FWHM}$ from Gaussian fitting increases with decreasing signal-to-noise. The green and the blue lines in Figures 11 and 12 denote, respectively, the 1σ and 3σ theoretical error envelope. These were calculated from Equation (A.1) in Porter et al. (2004) assuming $\langle \Delta V_{\rm FWHM} \rangle \sim 5\,{\rm km\,s^{-1}}$ and $T_{\rm rms} \sim 0.1$ K (typical values for methanol) and illustrate this effect quite clearly.

HIFI data obtained in beam switching mode generally provide quite a good measure of the continuum. Therefore, in each band, we have integrated the emission over the entire frequency range to obtain the line+continuum emission. Summation over the integrated intensities, listed in Table 4, of all the transitions in

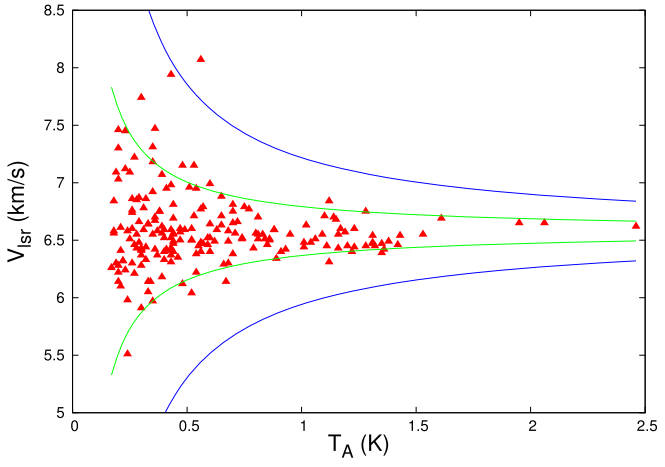

Figure 11. Plot of the measured V_{LSR} vs. T_A derived from independent Gaussian fits to each of the A-CH_3OH and E-CH_3OH transitions listed in Table 4. The green and blue lines are the 1σ and 3σ (respectively) theoretical error envelope for the V_{LSR} determined from Gaussian fitting of noisy lines predicted by Porter et al. (2004). Curves are calculated assuming $\langle \Delta V_{FWHM} \rangle \sim 5$ km s^{-1} and $T_{rms} \sim 0.1$ K (typical values for methanol).

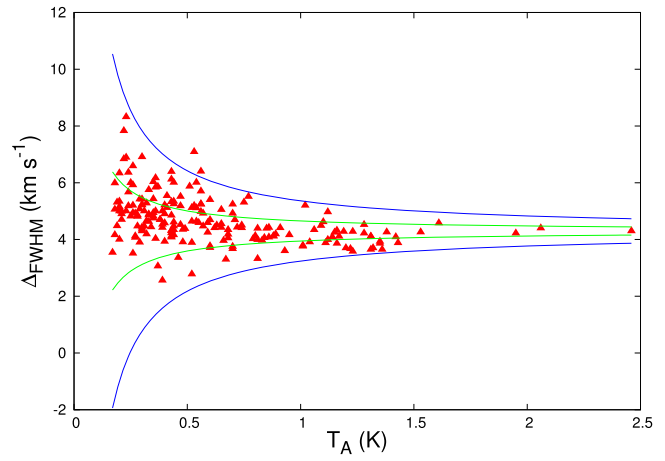

Figure 12. Plot of the measured ΔV_{FWHM} vs. T_A derived from independent Gaussian fits to each of the A-CH_3OH and E-CH_3OH transitions listed in Table 4. The green and blue lines are the 1σ and 3σ (respectively) theoretical error envelope for the Δ_{FWHM} determined from Gaussian fitting of noisy lines predicted by Porter et al. (2004). Curves are calculated assuming $\langle \Delta V_{FWHM} \rangle \sim 5$ km s^{-1} and $T_{rms} \sim 0.1$ K (typical values for methanol).

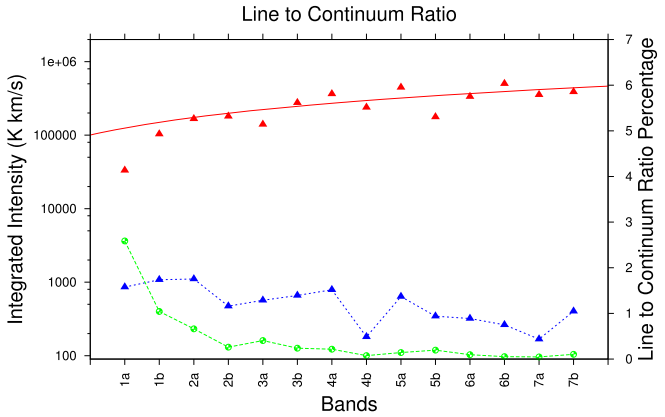

Figure 13. Plot of the continuum emission integrated over each band (red triangles), the integrated line emission in each band (blue triangles), and the line to continuum ratio percentage (green circles). The red line is a power-law fit to the continuum emission using a modified blackbody function (see the text for details).

each band provides the corresponding total line emission. Comparing the two provides the line to continuum ratio, which is interesting for the interpretation of broadband continuum images of star-forming regions. The advantage of our data is that the line and continuum emission are measured in the same beam with the same instrument and, therefore, there are no complications that arise from cross-calibration between different instruments or beam sizes. Figure 13 plots the band integrated continuum emission (red triangles), the integrated line emission in each band (blue triangles) and, on the right y-axis, the percentage line to continuum ratio (green circles). The figure shows that the line to continuum ratio is ~3%–1% in bands 1a–2a and drops to less than ~0.5% in the higher bands. These are both smaller than the ~10% seen in Orion-S in the 300 GHz band (Groesbeck 1995), suggesting that the line to continuum ratio generally decreases with increasing frequency. The dramatic drop in the line to continuum ratio between Band 1a to 2b is due to two factors. Over this frequency range, the continuum emission rises by a factor of a few while, at the same time, the number of spectral lines and their corresponding intensity drops by a factor of a few. The red line is a power-law fit to the red triangles using a modified blackbody in which the Planck function is multiplied by $\kappa_o(\nu/\nu_o)^\beta$, where κ_o is the dust mass opacity coefficient. The best fitted value for β is 1.0. This value is consistent with the behavior of dust in other studies of star-forming regions (e.g., Shetty et al. 2009).

3. RESULTS AND DISCUSSION

3.1. LTE Modeling

LTE modeling assumes that the gas is in Local Thermodynamic Equilibrium, meaning that the density is sufficiently high so that collisions dominate the excitation. The LTE modeling capability implemented in CASSIS has five input variables, N_t, T_{ex}, V_{LSR}, ΔV_{FWHM}, Ω, where N_t is the total column density, T_{ex} is temperature, and Ω is the size of the emitting region (which couples to the variable HIFI beam sizes to take into account beam dilution effects). Note that, by definition, under LTE conditions, the excitation temperature that determines the relative populations of the upper and the lower level of a spectral line, the rotation temperature that describes the populations of all the rotational levels of one species, and the gas kinetic temperature are all identical. Each combination of these variables produces a Gaussian model spectrum for each transition of the selected species. Note that, unlike the Gaussian fitting procedure, which fits the V_{LSR} and ΔV_{FWHM} to each line separately, for the LTE modeling, we obtain a single average value of V_{LSR} and ΔV_{FWHM} for all transitions of a given species.

In order to find the set of parameters that produce synthetic spectra that best fit the observed spectral line profiles, we used a Markov Chain Monte Carlo (MCMC) method implemented in CASSIS (e.g., Guan & Krone 2007). The MCMC method randomly picks a seed in the five-dimensional parameter space (which we call the X_0 state). Then it randomly chooses one of the nearest neighbors (called the X_1 state), as specified by a variable step size, which is calculated for each iteration. The χ^2 of the new state is calculated and if $p = \chi^2(X_0)/\chi^2(X_1) > 1$, then the new state is accepted. If $p = \chi^2(X_0)/\chi^2(X_1) < 1$, this new state might still be accepted with a certain acceptance probability. If the new state is rejected, the X_0 state will remain and another random nearby state will be picked as the X_1 state.

Table 5
LTE Modeling Results for Species Requiring One-component Fits

	N (cm^{-2})	T_{ex} (K)	ΔV_{FWHM} ($km\ s^{-1}$)	$\Delta\Omega$ ($''$)	V_{LSR} ($km\ s^{-1}$)
[C I]	$1.0 \pm 0.2 \times 10^{18}$	48.3 ± 8.8	4.2	64.9 ± 14.7	7.8
[C II]	1.4 to 1.9×10^{18}	200.0 to 500.0	4.3	90.0	8.4
CCH	$8.9 \pm 2.1 \times 10^{14}$	36.5 ± 5.9	4.1 ± 0.1	65.7 ± 12.1	7.2 ± 0.0
CH	$1.8 \pm 0.4 \times 10^{14}$	37.7 ± 15.2	4.2 ± 0.3	69.8 ± 8.1	8.0 ± 0.0
CH^+	2.9 to 4.2×10^{13}	30.0 to 300.0	4.6	90.0	8.0
CN	$2.6 \pm 1.3 \times 10^{14}$	29.1 ± 3.9	4.3 ± 0.1	67.6 ± 7.8	7.6
^{13}CO	$1.4 \pm 0.4 \times 10^{17}$	88.8 ± 14.4	4.2 ± 0.7	79.6 ± 7.8	7.1
$C^{18}O$	$3.5 \pm 0.5 \times 10^{16}$	61.9 ± 1.6	3.9 ± 0.0	69.3 ± 13.3	7.1
$C^{17}O$	$1.4 \pm 0.4 \times 10^{16}$	53.3 ± 1.9	3.6	64.7 ± 19.9	7.2 ± 0.0
$^{13}C^{18}O$	$8.1 \pm 1.6 \times 10^{14}$	54.3 ± 1.3	4.5	62.6 ± 12.0	7.1
DCN	$4.9 \pm 1.9 \times 10^{12}$	38.1 ± 5.4	6.1 ± 0.2	60.4 ± 15.4	7.0
DCO^+	$2.4 \pm 1.3 \times 10^{12}$	39.9 ± 2.3	3.0 ± 0.1	54.0 ± 15.3	6.7
H_2CS	$6.2 \pm 0.7 \times 10^{13}$	85.0 ± 2.8	4.5	68.0 ± 11.0	6.7
HCl	$1.6 \pm 0.6 \times 10^{14}$	32.2 ± 5.5	3.9 ± 0.1	52.5 ± 24.1	7.4
$H^{37}Cl$	$6.7 \pm 3.4 \times 10^{13}$	52.5 ± 15.6	3.7	53.3 ± 27.1	7.6
HNC	$2.4 \pm 0.3 \times 10^{13}$	28.2 ± 1.1	4.3 ± 0.1	67.2 ± 3.0	7.3
$H^{13}CO^+$	$7.1 \pm 1.8 \times 10^{12}$	39.7 ± 1.3	3.8 ± 0.0	58.6 ± 14.4	7.0
N_2H^+	$1.6 \pm 0.5 \times 10^{13}$	46.6 ± 1.9	2.6 ± 0.0	57.9 ± 17.2	6.3
NO	0.3 to 1.1×10^{16}	20.0 to 200.0	5.8	90.0	7.2
SO_2	$1.5 \pm 0.1 \times 10^{14}$	141.3 ± 8.4	6.7 ± 0.1	64.9 ± 9.6	7.5

Having a finite probability to accept a new position even if the χ^2 is worse, ensures that we do not converge directly to a local minimum, but instead forces better sampling of the full parameter space. The code runs with several initial random states, and usually, when the variance among different clusters of states is smaller than the variance of each cluster, it is assumed to have converged to the correct solution (Hastings 1970; Roberts et al. 1997). When the code approaches convergence, it calculates a number of models and χ^2 values in a tight cluster surrounding the "best" solution. This allows us to calculate a median value for each fitted parameter and its statistical standard deviation, which are listed in Table 5.

Despite the fact that we identify all transitions above 3σ, for our modeling, we only utilize transitions above 5σ, while neglecting the blended lines. However, when exploring the validity of our models, we also investigate frequency regions where potential transitions of the selected species exist in the molecular line databases, but were not detected above 3σ. This ensures that our models do not produce synthetic spectra where no transitions are actually observed. At the beginning of the procedure, we usually let all five parameters vary. However, we were frequently able to find good solutions for the V_{LSR}, and FWHM after the first convergence of the code. Therefore, on subsequent runs, we fixed the V_{LSR} and FWHM and allowed the other three parameters to vary. This significantly speeds up the computational time of subsequent runs. Once we obtain a good fit, we run the code 5 to 10 more times to ensure that different runs converge to the same solution within the error bars. In some cases, after running the code 5 to 10 times, the scatter of the converged solutions is larger than the standard deviation of any of the individual solutions. In this case, in Tables 5 and 6, we report the average of the multiple runs (i.e., we take the median value of each run and compute the average between runs) and the standard deviation of the solutions about this new average. In all cases, we let the source size (Ω) vary up to $90''$, twice that of the largest HIFI beam ($\sim 45''$). However, if the source size is larger than the largest beam, it is essentially unconstrained (though there is some sensitivity to source sizes that are larger than the beam since the beam is Gaussian in shape and not a tophat profile). In such cases, the source is simply considered to be extended in nature. Table 5 provides the results of our MCMC χ^2 fitting of the spectral lines listed in Table 4 (i.e., those with $S/N > 5\sigma$). Column 1 is the species, column 2 lists the median total column density of the species and the standard deviation, column 3 is the excitation temperature, column 4 is the FWHM line width, column 5 is the source size (Ω), and column 6 is the median LSR velocity. In cases where the error is not listed, the parameter was fixed in the MCMC fitting routine. Table 5 shows that the column density uncertainties range from 10% to 50%. To ensure that our assumption of LTE is valid, we ran the same MCMC fitting procedure using the non-LTE (RADEX) models implemented in CASSIS for a handful of species (N_2H^+, SO_2, ^{13}CO, and DCO^+). In all cases, the non-LTE column densities are consistent and within the reported error bars of the LTE models, as shown in Table 5. Given that the errors in Table 5 are the statistical uncertainties on the LTE solutions, to account for the possibility that LTE is not always a good approximation, we suggest that uncertainties on the high side of this range are probably appropriate.

Figure 9 provides an example of one-component modeling for ^{13}CO. The apparent shift in centroid velocity between the data (black histogram) and the LTE model (red Gaussian curve) is seen in a number of species and can also be seen by comparing the tabulated V_{LSR} listed in Tables 4 and 5. These apparent shifts of a few tenths of a $km\ s^{-1}$ are caused by the fact that the spectral lines are not perfectly Gaussian in shape; in some cases, this is possibly due to optical depth effects. In addition, the MCMC routine optimizes a number of free parameters to obtain the best overall physical model that fits all spectral lines simultaneously; as opposed to the Gaussian fitting routine, which simply fits a mathematical Gaussian profile to each spectral line separately. Thus, the median V_{LSR} and ΔV_{FWHM} determined from the LTE modeling may not perfectly match the actual V_{LSR} and ΔV_{FWHM} of any individual transition.

Table 6
LTE Modeling Results for Species Requiring Two Component Fits

	N_1 (cm^{-2})	T_{ex1} (K)	ΔV_{FWHM_1} (km s^{-1})	$\Delta\Omega_1$ ($''$)	V_{LSR1} (km s^{-1})	N_2 (cm^{-2})	T_{ex2} (K)	ΔV_{FWHM_2} (km s^{-1})	$\Delta\Omega_2$ ($''$)	V_{LSR2} (km s^{-1})
	Narrow Component					Broad Component				
CS	$6.5 \pm 1.9 \times 10^{14}$	36.5 ± 1.5	4.1	66.8 ± 10.8	7.2	$7.3 \pm 1.4 \times 10^{13}$	108.3 ± 2.4	9.5 ± 0.5	34.5 ± 8.2	7.0
^{13}CS[a]	$1.4 \pm 0.3 \times 10^{13}$	36.5	4.1	74.0 ± 13.6	7.2	$1.6 \pm 0.2 \times 10^{12}$	109.6 ± 1.3	9.5	34.5	7.0
$C^{34}S$[a]	$4.5 \pm 0.7 \times 10^{13}$	34.5	4.1	60.5 ± 8.9	7.2	$3.9 \pm 0.2 \times 10^{12}$	111.5 ± 3.5	9.5	34.5	7.0
o–H_2S	$1.0 \pm 0.2 \times 10^{15}$	24.5 ± 0.7	3.6	66.1 ± 14.1	7.0	$1.3 \pm 0.2 \times 10^{14}$	85.8 ± 18.3	8.8 ± 1.2	39.9 ± 8.1	7.2
p–H_2S	$9.4 \pm 1.5 \times 10^{14}$	24.3 ± 1.1	3.6	65.4 ± 13.5	7.0	$1.5 \pm 0.2 \times 10^{14}$	74.7 ± 9.9	7.4 ± 1.1	52.5 ± 10.5	7.1 ± 0.1
$H_2^{34}S$[a]	$3.2 \pm 0.6 \times 10^{13}$	25.1 ± 0.5	3.6	51.7 ± 7.7	7.0	$3.0 \pm 0.7 \times 10^{12}$	94.0 ± 15.1	9.0 ± 0.7	48.6 ± 10.0	7.2
o–H_2CO	$1.5 \pm 0.2 \times 10^{14}$	47.7 ± 4.3	4.0	69.3 ± 7.2	6.7	$3.8 \pm 0.6 \times 10^{13}$	153.6 ± 15.0	9.0 ± 0.3	47.7 ± 10.0	7.2 ± 0.2
p–H_2CO	$2.0 \pm 0.4 \times 10^{14}$	44.8 ± 3.0	4.0 ± 0.1	75.2 ± 10.7	6.7	$6.7 \pm 1.6 \times 10^{13}$	163.0 ± 27.2	9.0 ± 1.0	46.0 ± 9.3	7.3 ± 0.2
HCN	$2.2 \pm 0.4 \times 10^{14}$	34.3 ± 5.0	4.4	64.4 ± 6.5	7.2	$4.8 \pm 0.1 \times 10^{13}$	66.8 ± 5.2	13.4 ± 0.6	41.1 ± 6.2	6.6 ± 0.1
$H^{13}CN$	$5.1 \pm 0.7 \times 10^{12}$	30.5 ± 1.2	4.4	74.8 ± 7.4	7.2	$3.6 \pm 1.9 \times 10^{12}$	79.1 ± 7.8	11.0 ± 0.4	37.0 ± 10.8	6.6
HCO^+	$7.7 \pm 0.7 \times 10^{13}$	68.9 ± 1.8	4.3	74.8 ± 8.2	7.0	$1.5 \pm 0.4 \times 10^{13}$	69.5 ± 4.9	12.0 ± 0.8	40.1 ± 12.1	7.1 ± 0.1
NH_3 p & o	$1.4 \pm 0.3 \times 10^{14}$	20.0	4.2	80.3 ± 5.0	7.0	$8.4 \pm 5.4 \times 10^{13}$	35.8 ± 2.4	10.0	34.9 ± 11.2	7.2
SO	$1.0 \pm 0.4 \times 10^{15}$	33.7 ± 5.0	3.8 ± 0.5	60.2 ± 17.8	6.8 ± 0.2	$2.1 \pm 1.1 \times 10^{14}$	121.8 ± 13.6	10.7 ± 0.5	34.8 ± 8.9	7.2 ± 0.3

Note.
[a] Calculation based on the main isotopologue.

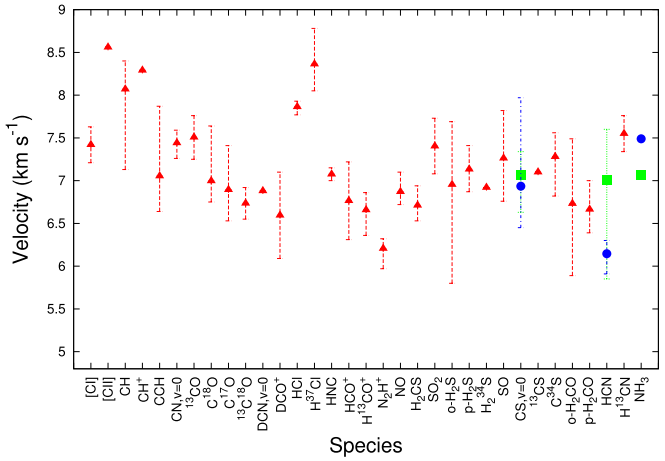

Figure 14. Mean $V_{\rm LSR}$ for each species derived from the Gaussian fits (Table 4). Red triangles indicate the mean $V_{\rm LSR}$ for species fit by a single Gaussian component. In cases requiring two component Gaussian fits, the narrow component is indicated by blue circle and the broad component is indicated by a green square. Error bars reflect the range in fitted $V_{\rm LSR}$ values provided in Table 4.

Although one-component modeling usually results in a remarkably good fit to the observations (e.g., $C^{18}O$, CH, CCH, etc), there are some cases in which a second (broad) component is necessary to properly reproduce the observations. This is independent of the broad-line wings seen in the transitions of some species that required a two component Gaussian fitting as mentioned in Section 2.3. In some cases, even species that were well fit by a single Gaussian component required two component LTE modeling, one with a narrow line width, and the other with a broad line. This is because, in these cases, there is no single combination of model parameters (notably $T_{\rm ex}$ and N_{tot}) that could reproduce the intensities of all transitions simultaneously. The two component LTE modeling implementation in CASSIS uses a two slab model; from the perspective of the observer, component 1 is the front slab and component 2 is the slab located behind it. The code allows component 1 to absorb emission from component 2. The results of the two component MCMC LTE modeling are listed in Table 6. Figure 10 provides an example of a species for which two component modeling was required. To see if this could be the result of non-LTE effects, we also attempted to model these species using the RADEX code (van der Tak et al. 2007) as implemented in CASSIS. For the RADEX modeling, we used the identical parameter range as for the LTE modeling. RADEX, however, invokes one additional free parameter, namely the H_2 volume density, which we allowed to range from 10^2 to 10^{10} cm^{-3}. In all cases, the RADEX modeling was unable to produce a good fit to all transitions unless a second physical component was included.

Note that ^{12}CO is not presented in either Tables 5 or 6 due to the presence of self-absorption from foreground material, which complicated the modeling procedure. We do, however, model the broad shock/outflow component separately for the analysis presented in Section 3.3.2.

3.2. Comments on Individual Species

The detected species listed in Table 2 can be related to a variety of physical processes that exist in the ISM, such as shocks, UV irradiation by nearby OB stars, and hot-core chemistry. In this section, we discuss some specific molecules in the context of these physical processes.

3.2.1. Tracers of UV Irradiation

Given the high UV flux in the Orion-S region ($\chi = 1.1 \times 10^5 \chi_0$; Herrmann et al. 1997), it is not surprising that we detect a wide variety of UV tracers.

[C I] and [C II]: [C I] and [C II] are the fine-structure lines of neutral atomic and singly ionized carbon. Both have been seen over large regions of the ISM. [C I] is known to trace PDRs at the UV illuminated surfaces of GMCs (Tielens & Hollenbach 1985; Plume et al. 1999; Papadopoulos et al. 2004), and [C II] is a tracer of the interface between the diffuse warm ionized medium and the outermost surface of GMCs (Velusamy et al. 2012). [C II] is also thought to be a tracer of CO "dark gas" (Langer et al. 2010). We have detected all [C I] and [C II] transitions accessible to HIFI, i.e., both of the [C I] ground-state fine-structure transitions: $^3P_1 \rightarrow {}^3P_0$ and $^3P_2 \rightarrow {}^3P_1$ ($V_{\rm LSR} \sim 7.5$ km s^{-1}), and the single [C II] transition: $^2P_{3/2} \rightarrow {}^2P_{1/2}$ ($V_{\rm LSR} \sim 8.6$ km s^{-1}), toward Orion-S. With only one transition of [C II], we modeled the column density assuming that the excitation temperature in the PDR was between 200 and 500 K. The velocity of [C II] is considerably different from the velocity of the dense, quiescent cloud component of Orion-S as traced by $C^{18}O$, CS, DCO^+, HCO^+, etc. (e.g., ~7 km s^{-1}; see Figure 14). This suggests that [C II] is tracing a kinematically distinct component of Orion-S; most likely photoevaporating material moving away from the molecular clump surfaces (e.g., Goicoechea et al. 2015). However, [C I] does not have a velocity that is dramatically different from the quiescent cloud component and is, in fact, similar to that of $C^{18}O$ (Figure 14). This is probably due to the fact that neutral atomic carbon exists slightly deeper in the cloud ($A_V > 3$–4), where it is still mixed with molecular material (see, e.g., Hollenbach & Tielens 1997; Mookerjea et al. 2012).

CH^+, CH, and CCH: CH^+, CH, and CCH are often associated with PDRs, with the former two also being tracers of "CO-dark molecular gas" (Gerin et al. 2010; Nagy et al. 2013). In addition, CH^+ and SH^+ can form via turbulent chemistry in the diffuse ISM (Godard et al. 2012). Transitions above 5σ detected toward Orion-S for these species are listed in Table 4. Enough transitions of CH and CCH were detected above 5σ that we could model the emission from these species (Table 5), both of which were well fit by 1 component models. For CH^+, we provide a range of column densities for a range of excitation temperatures between 30 and 200 K. From the Gaussian fits in Table 4, both CH and CH^+ have similar kinematics ($V_{\rm LSR} > 8.0$ km s^{-1}), whereas the CCH has $V_{\rm LSR} \sim 7.2$ km s^{-1} (see Figure 14). This suggests that CH and CH^+ trace the same region as the [C II] emission, i.e., the UV illuminated surface of the cloud, though possibly a deeper and denser region of the PDR, as suggested by Pan et al. (2001). CCH, which has a velocity closer to that of the quiescent gas, likely arises from deeper layers in the cloud (Nagy et al. 2015). The formation pathways for these species may help clarify these velocity differences. For example, CH^+ forms by an endothermic reaction: $C^+ + H_2 \rightarrow CH^+ + H$ (Federman et al. 1996). The formation of CH follows after a hydrogen abstraction reaction with CH^+ forming CH_2^+ and a subsequent dissociative recombination. Since these two species are closely linked to the C^+ abundance through one or two steps in the reaction

network, it makes sense that they would be linked physically and, therefore, kinematically. The formation of CCH, however, involves additional steps in the reaction chain, starting with the formation of $C_2H_2^+$ followed by dissociative recombination to form CCH (e.g., Wootten et al. 1980). Since this requires additional reactions involving molecular material, this species is probably more closely linked to the denser molecular gas.

SH^+ and CO^+: SH^+ and CO^+ are also species thought to trace regions with enhanced UV fields (Nagy et al. 2013). We detect two weak ($<5\sigma$) hyperfine components of SH^+ in Orion-S, which are too weak to be fitted or modeled but which, interestingly, are seen in emission rather than the usual absorption line profiles seen in the diffuse ISM (Godard et al. 2012). Although we do not report the Gaussian fit parameters of SH^+ or CO^+ due to the weakness of the transitions, an inspection of their lines suggests V_{LSR} of $\sim$8.5 km s^{-1}, which is virtually identical to the [C II] velocity. Although SH^+ can form via turbulent chemistry in the diffuse ISM, given the strength of the UV field in Orion-S, it is likely that the main formation pathway is $S^+ + H_2 \rightarrow SH^+ + H$. Therefore, like [C II], SH^+ probably also originates in the PDR at the surface of the cloud. The same is true of CO^+, which has a similar V_{LSR} (8.5 km s^{-1}) as SH^+ and [C II], and, like CH^+, forms directly from C^+ via the reaction $OH + C^+ \rightarrow CO^+ + H$.

CN and HCN: CN and HCN have both been detected in Orion-S. While both molecules are good tracers of warm dense gas, the CN/HCN abundance ratio is suggested to be an indirect measure of the UV field (e.g., Fuente et al. 1993); i.e., if the ratio is significantly larger than 1, then the UV field is thought to be enhanced. We have identified the $N = 5$–4, $N = 6$–5, and $N = 7$–6 transitions of CN above the 5σ noise level toward Orion-S and have modeled these transitions using a narrow component (see Table 5). The transitions of HCN ($J = 6$–5 to 13–12), however, exhibit the characteristic broad-line wings that required two component Gaussian fitting and LTE modeling (see Table 6). Figure 10 shows the LTE model fit to our HCN observations. Since the fits are constrained by the rms noise in each spectrum, the higher frequency transitions (which tend to have much larger noise) appear to be less well fit than the lower frequency/lower noise transitions. They are, however, still acceptable fits to the data within the given noise levels. Comparing the CN column density with the narrow component of HCN, we obtain a CN/HCN abundance ratio of 1.2 ± 0.6, indicating a moderately enhanced UV field. Given the high critical densities of these transitions ($\geqslant 10^8$ cm^{-3}) it is unlikely that they originate at the UV illuminated cloud surface. Instead, both their critical densities and the CN/HCN abundance ratio of 1.2 suggest that they arise deeper in the cloud (around $A_V > 5$; Fuente et al. 1993) and, therefore, are more closely associated with the dense molecular gas. This is also borne out by their velocities, which are similar to the dense, quiescent cloud component (Figure 14).

3.2.2. Complex Organic Molecules and Precursors

Complex organic molecules are often associated with hot-core chemistry. Unlike Orion-KL in which a plethora of complex organic molecules were detected (Crockett et al. 2014), in Orion-S, we only detect a handful of molecules that might be considered complex.

CH_3OH: methanol is an asymmetric top molecule, whose internal rotation results in two distinct symmetry species A–CH_3OH and E–CH_3OH. In total, we observed 359 methanol transitions above 3σ toward Orion-S, 170 A–CH_3OH, and 189 E–CH_3OH. 198 of the lines were above the 5σ noise level, 111 A–CH_3OH and 87 E–CH_3OH. While methanol is known to be a good temperature probe (e.g., Beuther et al. 2005; Wang et al. 2011), detailed modeling of methanol is beyond the scope of this paper and will be the subject of future work.

H_2CO: formaldehyde is another commonly used tracer of gas temperature (e.g., Mangum & Wootten 1993), in which the two hydrogen atom spins separate the molecule into distinct ortho and para species. Transitions of H_2CO above the 5σ noise level are listed in Table 4. We needed two component LTE modeling for both the ortho and para H_2CO molecules since one-component models could not simultaneously reproduce all observed transitions. The modeling (Table 6) results in low temperatures for the narrow component ($T_{ex} \sim 45$–50 K) and higher temperatures ($T_{ex} \sim 150$–165 K) for the broad component. The large line widths and the fact that the estimated source sizes are quite large ($>45''$) may indicate that the high-temperature H_2CO emission arises from shocks in the outflows rather than from a "hot-core" region. Ortho to para ratios in the narrow and broad components are 0.8 ± 0.1 and 0.6 ± 0.1 respectively. These low values are also consistent with our results for H_2S (see below). The spin temperatures associated with the ortho and para species are 7 ± 1 K and 6 ± 1 K respectively, suggesting that if formaldehyde formed under LTE conditions, the formation temperature was very low.

CH_3OCH_3: dimethyl ether is a complex molecule detected toward Orion-S. Since this molecule has no transition above 5σ, we only report it as a detection in Table 2.

The lack of complex organic molecules suggests that, if hot cores exist in Orion-S, they are still in their infancy and have not had time to either expand dynamically or develop chemically. This is not surprising given the very small size of the embedded submillimeter continuum sources detected in the region (Zapata et al. 2005). In addition, if these submillimeter continuum sources are indeed hot cores they are approximately 10 times smaller than the Orion-KL hot core. Therefore, the beam dilution in Orion-S would be 100 times worse. Thus, any transitions arising from the Orion-KL hot core that have an intensity of less than a few kelvin in the survey of Crockett et al. (2014) would be undetectable in our survey if they originate from the considerably smaller region in Orion-S. Alternatively, it is possible that Orion-S is not a massive star-forming region at all and, therefore, there are no hot cores in this region. Observations with higher spatial resolution or at lower frequencies (with associated lower excitation temperatures) would help address this issue by revealing the presence of more complex organics.

3.2.3. Pure Shock Tracers

SiO: SiO abundances can be enhanced by more than two orders of magnitude in hot and shocked regions (e.g., Iglesias & Silk 1978; Martin-Pintado et al. 1992) and SiO emission is often used as a tracer of molecular outflows since the SiO emission traces the outflow material itself, rather than the dense protostellar core (Martin-Pintado et al. 1992). This is believed to be due to Si-bearing dust grains being shattered by the outflow, followed by a rapid gas-phase reaction with free oxygen to produce SiO (e.g., Schilke et al. 1997b; Gusdorf et al. 2008a, 2008b). A number of outflows have already been identified in Orion-S by Zapata et al. (2006). In our data, although we could not identify any SiO emission above the 5σ

level, we have identified three SiO transitions above the 3σ level ($J = 12$–11, 13–12, 14–13, $v = 0$) at a velocity of $6.2\,\mathrm{km\,s^{-1}}$ (similar to the quiescent gas). With additional spectral smoothing (to a velocity resolution of $\sim 4\,\mathrm{km\,s^{-1}}$) it is clear that these transitions are real, with $\mathrm{S/N} > 5\sigma$. These transitions are quite broad ($\Delta V \sim 20$–$30\,\mathrm{km\,s^{-1}}$), which is reasonable considering the observed characteristics of the SiO outflows, as seen by Zapata et al. (2006). Given the existence of such high-J transitions with excitation energies above ~150 K, this indicates the presence of at least a small amount of hot shocked SiO in Orion-S.

3.2.4. Tracers of Quiescent Gas

CO, ^{13}CO, $C^{18}O$, $C^{17}O$, and $^{13}C^{18}O$: for all carbon monoxide isotopologues, excluding $^{12}C^{16}O$ itself, one-component Gaussian fitting and LTE modeling match the observations remarkably well. $^{12}C^{16}O$ itself, however, exhibits a broad-line wing (clearly tracing an outflow/shock) and, due to the presence of self-absorption, was not modeled. The existence of an outflow is not visible in any of the $^{12}C^{16}O$ isotopologue transitions due to their lower abundances. The LTE modeling of ^{13}CO is shown in Figure 9. For all $^{12}C^{16}O$ isotopologues (except $^{13}C^{18}O$), we see transitions from $J = 5$–4 to 11–10 above the 3σ level. For $^{13}C^{18}O$ the highest transition we detect above 3σ is $J = 7$–6. The higher J transitions are buried in the larger noise of the higher frequency HIFI bands. For $^{12}C^{16}O$, however, we detect lines up to $J = 16$–15. For the isotopologues, the typical V_{LSR} is approximately $7\,\mathrm{km\,s^{-1}}$, indicating that these species trace the quiescent gas in the cloud. The V_{LSR} of the main isotopologue, however, is often a bit higher than this, probably due to the Gaussian fits being skewed by the presence of self-absorption in the spectra, or due to the fact that, with its high opacity, $^{12}C^{16}O$ may be tracing a different physical region of the cloud. Interestingly, in Table 5, a correlation can be seen between the CO isotopologues and the derived excitation temperature; with the more optically thick species, which trace the cloud surface (e.g., ^{13}CO), having a higher temperature than the optically thin ones, which preferentially trace the interior (e.g., $^{13}C^{18}O$). This suggests that the external UV field is responsible for much of the heating in Orion-S (see also Tauber & Goldsmith 1990). This is different than the usual case of isolated star formation, in which the gas is predominantly heated internally by the process of gravitational collapse and the formation of an embedded protostar.

Deuterium-bearing Molecules: deuterated species are a subject of considerable interest in the ISM, since the D/H ratio in molecular clouds can be considerably enhanced over the cosmic value of $\sim 10^{-5}$. In Orion-S, we detect only a few deuterated species: DCN, DCO^+, and HDO, which all have velocities similar to that of the quiescent gas. Enhanced deuteration can occur because fractionation reactions involving deuterium are favored in low-temperature environments associated with pre-stellar cores, the resultant deuterated molecules can freeze onto grains, and then be released back into the gas phase when star-formation activity begins to heat the natal gas (e.g., Ceccarelli et al. 2007, p. 47). Thus, deuterated species, such as DCN and HDO, can trace the chemical history of the gas. In Orion-S, we found the DCN/HCN column density ratio to be 0.02 ± 0.01, suggesting considerable enhancement in cold gas. The DCO^+/HCO^+ column density ratio is 0.03 ± 0.02. While the DCO^+ abundance can be enhanced in cold gas via H_2D^+, Parise et al. (2009) have shown that deuteration can also occur in the gas phase of warm regions, like the Orion Bar via the CH_2D^+ ion. Although we detected three HDO transitions, it was the only species for which we were not able to find any models that converged to a good solution. Therefore, there is no way to give even a rough estimate for the D/H ratio in water.

N_2H^+: while N_2H^+, $J = 1$–0, is often associated with cold, dense gas, we detect N_2H^+ transitions from $J = 6$–5 to 10–9. LTE modeling indicates excitation temperatures of ~47 K, suggesting that even the dense gas in Orion-S is quite warm. Previous observations of CH_3C_2H in Orion-S (Bergin et al. 1994) confirm this idea. The V_{LSR} of N_2H^+ (Figure 14) also suggests that it originates from the quiescent gas. The upper limit for the column density of N_2D^+ with the same excitation condition as that found for N_2H^+ is $5 \times 10^{11}\,\mathrm{cm^{-2}}$. This provides a rough estimate of the D/H ratio of <0.03.

3.2.5. Tracers of Both Shocked and Quiescent Gas

As previously mentioned, there are a number of species, for which we had to invoke two component LTE modeling in order to fit the observed transitions (see Table 6). Narrow spectral components are usually associated with quiescent gas, whereas broader spectral components trace more dynamic gas that is often associated with shocks. This suggests that species listed in Table 6 can simultaneously exist in both quiescent and shocked gas components. This is not surprising, since Bachiller & Pérez Gutiérrez (1997) show that, in the bipolar outflow L1157, while some species are clearly quiescent gas tracers, many species exist in both components. Of these latter species, their abundances in the shocked gas are often an order of magnitude or more higher than their abundances in the quiescent gas. We will explore the issue of abundances further in Section 3.3.2. Here, however, we will briefly discuss some of the species listed in Table 6 as possible tracers of both shocked and quiescent gas.

H_2O: while H_2O is not listed in Table 6, it is an important molecule in the ISM and has been the subject of a number of important studies using the *Herschel Space Observatory* in both shocked and unshocked gas. Both the ortho and para forms of H_2O were detected in Orion-S, as well as one transition of o-$H_2^{18}O$. The H_2O transitions required two component Gaussian fitting due to the presence of a broad-line wing in the spectra (Table 4). The modeling of water is a complex affair and is beyond the scope of this paper. However, Choi et al. (2014) modeled the ortho and para $H_2^{18}O$ in Orion-S and found LTE column densities of $2 \times 10^{11}\,\mathrm{cm^{-2}}$ and $2 \times 10^{12}\,\mathrm{cm^{-2}}$, respectively, which suggests an ortho to para ratio of 0.1, indicating that it is unlikely that water formed under LTE conditions. Their non-LTE analysis of the data, however, brings the ratio up to a factor of two. Choi et al. (2014) also show that the ortho to para ratio is ~0.3 in the nearby Orion Bar. Both values are well below the usual value of three, which indicates a non-LTE formation mechanism for water in both Orion-S and the Bar, possibly due to photodesorption from dust grains.

H_2S and $H_2^{34}S$: H_2S is an asymmetric rotor that has ortho and para spin modifications. It is considered to be a tracer of high-temperature grain surface chemistry (e.g., Watson & Walmsley 1982). Similar to SO, despite the fact that we fit the H_2S transitions with a single Gaussian in Table 4, H_2S also required a second physical component in order to obtain a good

χ^2 fit from the LTE modeling process. As Table 6 shows, we modeled the H_2S emission from the ortho and para spin modifications separately. In both cases, the narrow component has a line width of ~3.6 km s^{-1}, a low excitation temperature (24 K), and is fairly extended (emission extending beyond the *Herschel* beam) whereas the broad component has a larger line width (~8 km s^{-1}), is warmer (~80 K), and yet is still fairly extended (>35″). The ortho to para ratio in the narrow component is 1.1 ± 0.3 and in the broad component is 0.9 ± 0.1 indicating a spin temperature of 9 ± 2 K. These values are consistent with those determined for H_2O in Orion-S by Choi et al. (2014) and for Formaldehyde (above). Similarly, this low ortho to para ratio suggests either a very low formation temperature for H_2S or that non-LTE effects had an important role in its formation. To model $H_2^{34}S$, we coupled its single ortho transition with those of the common isotopologue. The isotopic ratio is another possible free parameter in CASSIS, which assumes that the other parameters of both isotopologues are identical. The isotopic ratio converged to 31 ± 9. Note, however, that there is only one weak transition of $H_2^{34}S$ that we used to determine this ratio. For comparison, typical values for the $^{32}S/^{34}S$ ratio in galactic molecular clouds are $\sim 19 \pm 8$ (Lucas & Liszt 1998), which is consistent with the solar value of 23 (Anders & Grevesse 1989).

CS: CS is a well-known tracer of dense gas due to its high critical density (Plume et al. 1992). We observe many transitions of CS, from $J = 10$–9 to $J = 19$–18. Like CO, CS requires two components to be successfully fit by a Gaussian profile and modeled; one being narrow ($\Delta V_{\rm FWHM} \sim 4.1$ km s^{-1}), extended ($\Omega = 67''$), and cool ($T = 37$ K), and the other being broader ($\Delta V_{\rm FWHM} \sim 10$ km s^{-1}), moderately extended ($\Omega = 35''$), and warm ($T = 108$ K). The broad component is not seen in the spectra of the CS isotopologues but was needed to successfully model the transitions. ^{13}CS and C^{34}S were modeled in a fashion similar to that of $H_2^{34}S$ (i.e., the transitions of the isotopologues modeled simultaneously with those of the common isotope, and found to have an isotopic ratio of 46 ± 17 and 14 ± 5 respectively). The Gaussian fitted (Table 5) and modeled velocity (Table 6) of both components is ~7 km s^{-1}, suggesting that both components originate in the same material (Figure 14).

HCN: the transitions of HCN ($J = 6$–5 to 13–12) exhibit the characteristic broad-line wing that required both two component Gaussian fitting and LTE modeling (see Table 6). As is usual for other species, the broad component is hotter (67 K versus 34 K), broader (13.4 km s^{-1} versus 4.4 km s^{-1}), and less spatially extended (41″ versus 64″) than the narrow component. While the broad component's $V_{\rm LSR}$ is lower than that of narrow component (6.6 km s^{-1} versus 7.2 km s^{-1}) both are consistent with the systemic velocity of Orion-S (Figure 14).

HCO$^+$: HCO^+ is another well-known tracer of both dense molecular gas and outflows. We detected the $J = 6$–5 to $J = 13$–12 transitions of HCO^+ in Orion-S, which span a wide range of physical conditions ($E_{\rm up} = 90$ K, $n_{\rm crit} \sim 3.2 \times 10^7$ cm^{-3} to $E_{\rm up} = 389$ K, $n_{\rm crit} \sim 6.0 \times 10^8$ cm^{-3}). HCO^+ has some of the strongest lines seen in our survey of Orion-S. Despite the fact that we fit the HCO^+ transitions with a single Gaussian in Table 4, HCO^+ required a second physical component in order to obtain a good χ^2 fit from the LTE modeling process (see Table 6). Both components have a velocity of ~7 km s^{-1} and are fairly warm (~69 K), suggesting a common origin.

NH$_3$: we detect two transitions above the 5σ level in Orion-S: one in emission ($1_{0,0} - 0_{0,1}$) and one in absorption ($2_{1,1} - 1_{1,0}$). In fact, we detect three additional transitions of NH_3 (all in absorption), but since they were just below the 5σ level, we do not report them in Table 4. Modeling these transitions simultaneously requires two components: a cold ($T \sim 20$ K), quiescent ($\Delta V \sim 4.2$ km s^{-1}) layer of gas in front of a warmer ($T \sim 36$ K), broader ($\Delta V = 10$ km s^{-1}) component. The $V_{\rm LSR}$ values of both NH_3 components are consistent with the systemic velocity of the cloud (Figure 14). The presence of absorption lines provides additional evidence for the existence of two components in Orion-S (one warm and one cool). The fact that the low energy transition is seen in emission, whereas the higher energy transition is seen in absorption may be related to the beam size and the strength of the continuum. At 572 GHz, the continuum is weaker than it is at 1215 GHz (see Figure 13) and may be too beam-diluted to see absorption. However, at higher frequencies, the beam couples better to the source and absorption may become more prevalent. This suggests that NH_3 may not come from a high density, hot region, which is consistent with our conclusion that there are no hot cores in Orion-S.

SO$_2$: SO_2 is also often a tracer of shocks, since it can freeze onto grain mantles at early evolutionary times when the gas is cold and dense, and later be returned to the gas phase by shocks (e.g., Millar & Herbst 1990; Esplugues et al. 2013). Toward Orion-S, we detected a number of SO_2 transitions above the 5σ level (see Table 4). Given the fact that all the observed SO_2 lines are relatively weak, one-component modeling matches the observations remarkably well. LTE modeling for this species (Table 5) shows that the SO_2 is fairly warm ($T_{\rm ex} \sim 150$ K), broad ($\Delta V \sim 6.7$ km s^{-1}), and extended (~65″). The velocity of SO_2 is also similar to the velocity of the quiescent gas (Figure 14).

SO: in contrast with SO_2, and despite the fact that we fit the SO transitions with a single Gaussian in Table 4, SO required a second physical component in order to obtain a good χ^2 fit from the LTE modeling process (see Table 6). The narrow component has a line width of 3.8 km s^{-1}, a moderately low temperature (34 K), and is extended beyond the Herschel beam. Despite the fact that the broad component ($\Delta V_{\rm FWHM} = 11$ km s^{-1}) is much warmer (122 K), it is still quite extended in size (35″).

The large line widths (7–13 km s^{-1}), high temperatures (70–150 K), and extended size (>30″) determined for the second physical components of these species suggest that the embedded outflows seen in Orion-S (Schmid-Burgk et al. 1990; Ziurys et al. 1990; Zapata et al. 2005) have affected a large volume of the region both thermally and dynamically. Whether or not these shocks have affected the chemistry of the gas will be examined in Section 3.3.

3.3. Chemical Comparison with Orion-KL

One of the main goals of this project is to explore the chemical differences and similarities between Orion-S and Orion-KL. As mentioned in Section 1, a detailed comparison between the chemical abundances in Orion-S and Orion-KL is useful, since both regions presumably formed under similar conditions, but could have developed very different chemical abundances based on differences in their ages, densities,

Table 7
The Abundance of Species with Respect to H_2

Species	Narrow Comp wrt H_2	Broad Comp wrt H_2	Abundance Enhancement Factor
CCH	4.32×10^{-9}	...	...
CN	1.26×10^{-9}	...	...
$C^{17}O$	6.80×10^{-8}	...	...
$^{13}C^{18}O$	3.93×10^{-9}	...	...
DCN	2.38×10^{-11}	...	...
HCl	7.77×10^{-10}	...	...
$H^{37}Cl$	3.25×10^{-10}	...	...
HNC	1.17×10^{-10}	...	...
NO	3.40×10^{-8}	...	...
$H^{13}CO^+$	3.45×10^{-11}	...	...
H_2CS	3.01×10^{-10}	...	...
SO_2	7.29×10^{-10}	...	...
H_2S	9.42×10^{-9}	3.29×10^{-7}	35
$H_2^{34}S$	1.46×10^{-10}	3.41×10^{-9}	23
SO	4.86×10^{-9}	2.47×10^{-7}	51
^{13}CS	6.80×10^{-11}	1.88×10^{-9}	28
$C^{34}S$	2.19×10^{-10}	4.59×10^{-9}	21
NH_3	6.80×10^{-10}	9.88×10^{-8}	145
H_2CO	1.70×10^{-9}	1.24×10^{-7}	73

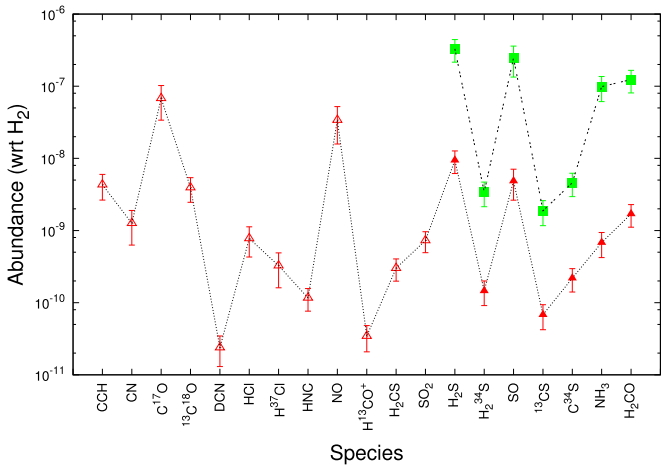

Figure 15. Abundance (with respect to H_2) of species listed in Tables 5 and 6. Open red triangles indicate the abundance ratio for species fitted by a single component LTE model in Orion-S. In cases requiring two component LTE models for the Orion-S data, the abundance ratio for the narrow component is indicated by solid red triangles and that for the broad component is indicated by solid green squares. Therefore, the dotted line connects species/components that likely trace quiescent gas, whereas the dashed line connects species/components that may trace shocked gas.

temperatures, radiation fields, etc. As part of the HEXOS survey, and in a direct analogue to our study, Crockett et al. (2014) have observed the same frequency range in Orion-KL using the same instrument. Therefore, we have a perfectly matched database with which to compare our results. In this section, we will compare the chemistries of these two regions. All of the Orion-KL data are taken from the HEXOS survey of this region as listed in Crockett et al. (2014) using the column densities derived from their XCLASS LTE modeling of the data.

3.3.1. Chemical Abundances in Orion-S

Our LTE modeling produces column densities but, to obtain chemical abundances, we must scale each column density by

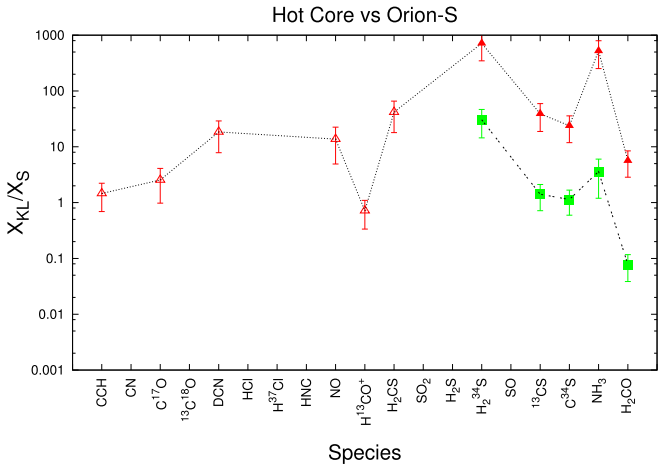

Figure 16. Comparison of the abundances of species detected in the Orion-KL Hot Core to those in Orion-S as given by Equation (1) in Section 3.3.2. Symbols are the same as described in Figure 15.

the H_2 column density, which is not known directly. Therefore, we use $C^{18}O$ as a proxy for the H_2 column density. The $C^{18}O$ transitions we observe in Orion-S are optically thin and have only a single narrow component (Table 4) that is well fit by a column density of $3.5 \times 10^{16}\,cm^{-2}$ (Table 5). To convert this to an H_2 column density, we use a $C^{18}O$:H_2 conversion factor of 1.7×10^{-7} (Goldsmith et al. 1997) to obtain $N_{H_2} = 2.1 \times 10^{23}\,cm^{-2}$.

Other species have been modeled using both a narrow and broad component (Table 6), the latter is possibly indicative of gas affected by shock. To compute the chemical abundances in the broad component of species listed in Table 6, we need an estimate of the $C^{18}O$ column density specifically present in this broad component. Since the broad component is too optically thin to be detected in $C^{18}O$ or even ^{13}CO, we rely on ^{12}CO instead for this purpose. In this case, we attempt to model the broad (i.e., line wing) component of our observed ^{12}CO lines by fitting three Gaussian components to each transition. The first two Gaussians fit the "main" component of the asymmetric CO profile (see Table 4) and the third fits the outflow ($\Delta V \sim 18\,km\,s^{-1}$). This third component is then modeled via our LTE procedure to estimate the physical parameters of the ^{12}CO outflow ($T_{ex} \sim 200\,K$; $N(CO) \sim 7.1 \times 10^{16}\,cm^{-2}$; $\Omega > 30''$). Dividing this column density by the canonical ^{12}CO:$C^{18}O$ abundance ratio of 500:1 provides a $C^{18}O$ column density of $1.4 \times 10^{14}\,cm^{-2}$ for the broad component in Orion-S, which is a factor of ~250 smaller than the $C^{18}O$ column density in the narrow component as measured by directly modeling our $C^{18}O$ observations. Using the same $C^{18}O$:H_2 scaling relationship as above, we obtain $N_{H_2} = 8.2 \times 10^{20}\,cm^{-2}$.

Therefore, dividing the modeled column densities of the broad components of the species in Table 6 by $8.2 \times 10^{20}\,cm^{-2}$ gives the abundance (with respect to H_2) of all species in Orion-S that are possibly affected by shocks. Dividing the modeled column densities of the rest of the species in Table 5, as well as the narrow component of the species in Table 6, by $2.1 \times 10^{23}\,cm^{-2}$ gives the abundance (with respect to H_2) of all species in Orion-S that likely originate in quiescent gas. The results are provided in Table 7 and illustrated in Figure 15, which clearly show that in the broad component (green squares) the abundances are enhanced

by a factor of 10–100 with respect to the narrow component (red triangles). Abundance enhancements of this magnitude indicate classic shock behavior (Bachiller & Pérez Gutiérrez 1997). This suggests that shock chemistry is playing an important role in Orion-S.

3.3.2. Species Common to Both Orion-KL and Orion-S

Crockett et al. (2014) detected ~13,000 lines from 39 different molecules (79 species if one includes all the isotopologues). This is considerably more than the 685 lines from 52 species (including isotopologues) that we have detected in Orion-S. In addition, the lines in Orion-KL are typically an order of magnitude stronger than those seen in Orion-S. A more interesting comparison, however, is to examine the abundances of species common to the two sources.

Crockett et al. (2014) produce column densities for many of the detected species in Orion-KL. To compare with the chemical abundances in Orion-S (Section 3.3.1), we must also scale by the H_2 column density in Orion-KL. For Orion-KL, we use the $C^{18}O$ column densities derived by Plume et al. (2012) as a proxy, which breaks down the results for each of the four known kinematic components: the Hot Core ($V_{LSR} \sim 4$–6 and $\Delta V \sim 7$–12 km s^{-1}), the Plateau ($V_{LSR} \sim 7$–11 and $\Delta V_{LSR} \geqslant 20$ km s^{-1}), the Compact Ridge ($V_{LSR} \sim 7$–9 and $\Delta V \sim 3$–6 km s^{-1}), and the Extended Ridge ($V_{LSR} \sim 8$–10 and $\Delta V \sim 2$–4 km s^{-1}) (Blake et al. 1987). The H_2 column density can then be produced using the same $C^{18}O$:H_2 conversion factor of 1.7×10^{-7}.

Producing abundances in this way does depend on the assumptions regarding the $C^{18}O$:H_2 abundance ratio. However, by dividing the abundance of a given species in Orion-KL by the abundance of the same species in Orion-S, we eliminate the $C^{18}O$:H_2 abundance ratio altogether and are essentially normalizing to the $C^{18}O$ column density in each region. This does, of course, assume that $C^{18}O$ abundances are the same in both sources, which may be reasonable based upon similarities between the observed $C^{18}O$:$C^{17}O$ ratios (e.g., 2.5 in Orion-S, 3.0 in the Hot Core, 6.5 in the Compact Ridge, 3.5 in the Plateau, and 2.3 in the Extended Ridge). These ratios are also consistent with those found by Ladd (2004).

Therefore, we are essentially creating the following ratio.

$$\frac{X_{KL}}{X_S} = \frac{\left(\frac{N_i}{N_{C^{18}O}}\right)_{KL}}{\left(\frac{N_i}{N_{C^{18}O}}\right)_S} \quad (1)$$

where N_i is the column density of species i and $N_{C^{18}O}$ is the column density of $C^{18}O$. The subscripts KL and S refer to this ratio in Orion-KL and Orion-S respectively. Given the four distinct kinematic components of Orion-KL, we create this ratio for the Hot Core (HC), the Plateau (P), the Compact Ridge (CR), and the Extended Ridge (ER) separately and, again, use different values for the $C^{18}O$ abundance in Orion-S depending on whether the species in question has a narrow or broad spectral line profile.

Figure 16 shows the comparison between Orion-S and the Orion-KL Hot Core. Note that, by common use, the term "hot core" refers to a dense, warm region surrounding a central high-mass protostellar object that dominates its energetics (Kurtz et al. 2000, p. 299). It has been argued that the eponymous hot core in the Orion-KL region does not fulfill this criterion (Zapata et al. 2011). Rather, these authors suggest that this region is instead powered by the aftermath of the explosion caused by a stellar merger event (Bally & Zinnecker 2005). Regardless of this, in the present paper, we are comparing the chemical abundances of Orion-S with those in what is

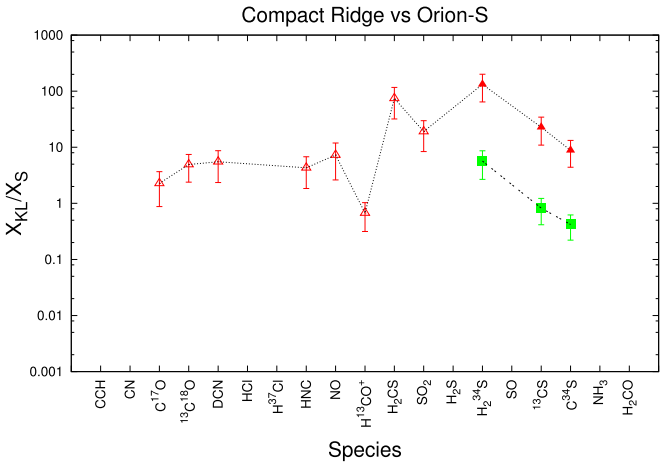

Figure 17. Same as for Figure 16 except for the Orion-KL Compact Ridge.

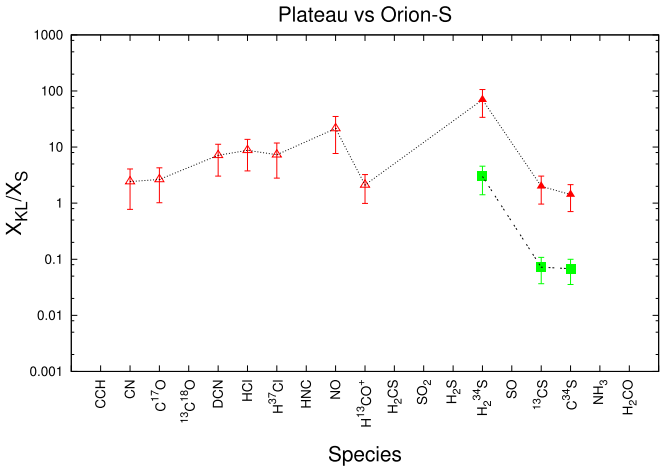

Figure 18. Same as for Figure 16 except for the Orion-KL Plateau.

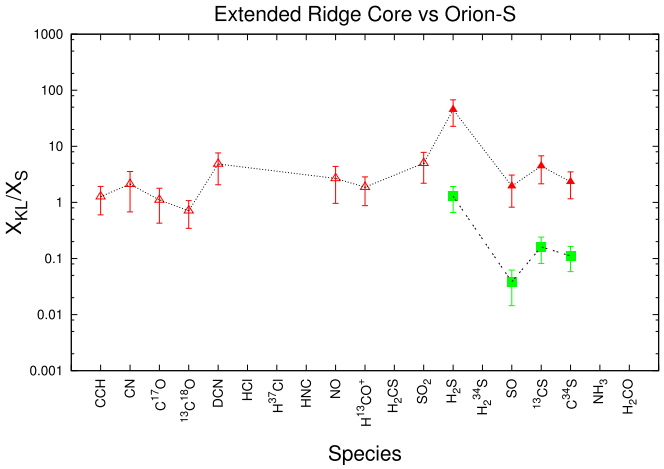

Figure 19. Same as for Figure 16 except for the Orion-KL Extended Ridge.

traditionally referred to as the "hot-core" component of Orion KL. The *x*-axis indicates the species and the *y*-axis shows the ratio as calculated from Equation (1). Open red triangles indicate molecules for which one-component LTE models in Orion-S were sufficient. In cases where we required two components to model the Orion-S data, the solid red triangles indicate the ratio for the narrow component and the solid green squares indicate the ratio for the broad component. The dotted line connects species/components that likely trace quiescent gas, whereas the dashed line connects species that have a broad component. Not all species detected and modeled in Orion-S are represented in this figure. This is due to the fact that Crockett et al. (2014) did not model all their detected species (notably the atomic species), nor did they provide column densities for species in which the lines were optically thick (e.g., CO, ^{13}CO, HCO$^+$, CS) in Orion-KL. Note also that not every species listed in Figure 16 has a symbol associated with it (e.g., CN, HCl, SO, etc.). This is because emissions from these species were not attributed to the HC, but rather to one or more of the other kinematic components in Orion-KL. Error bars are calculated from the statistical uncertainties determined from our LTE modeling of Orion-S (∼10%–50%; see Tables 5 and 6) and with the assumption of 10% error bars of the reported column densities in Orion-KL Crockett et al. (2014), which includes the effects of calibration errors, pointing errors, etc. However, to account for the possibility that LTE is not a good approximation in either Orion-S or Orion-KL, we add an additional 40% error to the column densities. This value is based on a comparison of LTE versus non-LTE column density calculations for the Orion-KL Extended Ridge (Crockett et al. 2014).

An inspection of Figure 16 clearly shows that the abundances of species in the Orion-KL HC are significantly higher than those in the narrow component of Orion-S (dotted line in Figure 16). Except for CCH, C^{17}O, and H^{13}CO$^+$, the abundances in the HC are $\gtrsim$10 times larger than those in Orion-S. Examining the abundance ratios in the narrow component, we obtain $\left\langle \frac{X_{\rm KL}}{X_{\rm S}} \right\rangle = 135$ (SD = 260), where SD is the standard deviation about the mean. The large standard deviation simply reflects the enormous scatter in the ratios (note that the *y*-axis in Figure 16 is on the log scale). Although still not a good match, the disagreement is smaller for species that have a broad component, (dashed line in Figure 16). In this case, we obtain $\left\langle \frac{X_{\rm KL}}{X_{\rm S}} \right\rangle = 6$ (SD = 12). Given the lack of complex molecules noted in Section 3.2.2 and the poor match in the abundances between the Orion-KL HC and Orion-S, this suggests that the gas detected in this study of Orion-S does not originate in a hot core.

Figure 17 shows that the abundances of species in the Orion-KL CR are also higher than those in the narrow component of Orion-S ($\left\langle \frac{X_{\rm KL}}{X_{\rm S}} \right\rangle = 23$; SD = 45) but the agreement is better than it is for the HC. Again, the match is better to the broad component ($\left\langle \frac{X_{\rm KL}}{X_{\rm S}} \right\rangle = 1$; SD = 2) of the two component fits in Orion-S (dashed line) than it is to the narrow component.

Figure 18 shows the comparison between Orion-S and the Orion-KL Plateau region. The match between abundances here is clearly better than it is for the HC or the CR with $\left\langle \frac{X_{\rm KL}}{X_{\rm S}} \right\rangle = 14$ (SD = 22) for the narrow component (dotted line) and 1 (SD = 2) for the broad component (dashed line). Note that, although

Table 8
Column Density Upper Limit for Species in Orion-KL Not Detected in Orion-S

Species	$N_{t,T_{\rm ex}=40\ {\rm K}}$	$N_{t,T_{\rm ex}=80\ {\rm K}}$	E_u
$^{15}NH_3$	7.0×10^{11}	3.0×10^{12}	700
^{29}SiO	2.0×10^{12}	1.0×10^{12}	700
^{30}SiO	3.0×10^{12}	2.0×10^{12}	300
C_2H_3CN	N/A	N/A	300
C_2H_5CN	N/A	N/A	···
C_2H_5OH	N/A	N/A	···
$C^{33}S$	6.0×10^{12}	4.0×10^{12}	700
CH_2DOH	6.0×10^{13}	6.0×10^{13}	300
CH_2NH	7.0×10^{12}	2.0×10^{13}	300
$CH_3^{13}CN$	3.0×10^{14}	2.0×10^{13}	700
CH_3CN	7.0×10^{14}	5.0×10^{13}	700
CH_3CN, $v_8 = 1$	N/A		700
$^{13}CH_3CN$	4.0×10^{14}	2.0×10^{13}	700
CH_3OCHO	2.0×10^{15}	2.0×10^{15}	300
CH_3OD	N/A	N/A	700
$^{13}CH_3OH$	N/A	N/A	300
D_2O	5.0×10^{11}	2.0×10^{12}	300
$H_2^{13}CO$	1.5×10^{15}	1.5×10^{14}	700
$H_2^{17}O$	5.0×10^{11}	1.5×10^{12}	300
H_2CCO	1.5×10^{15}	2.0×10^{14}	700
H_2O, v_2	N/A	N/A	700
$H^{13}CN$, $v_2 = 1$	N/A	N/A	700
HC_3N	2.0×10^{17}	5.0×10^{14}	700
HC_3N, v = 0	4.0×10^{17}	6.0×10^{14}	700
HCN, $v_2 = 1$	N/A	N/A	700
HCN, $v_2 = 2$	N/A	N/A	700
$HD^{18}O$	5.0×10^{11}	3.0×10^{12}	300
HDCO	7.0×10^{12}	9.0×10^{12}	300
$HN^{13}C$	8.0×10^{11}	1.0×10^{12}	300
$HN^{13}CO$	5.0×10^{12}	1.0×10^{13}	300
HNC, $v_2 = 1$	N/A	N/A	700
HNCO	5.0×10^{12}	1.0×10^{13}	300
NH_2CHO	3.0×10^{13}	3.0×10^{13}	700
NH_2D	4.0×10^{12}	8.0×10^{12}	300
NH_3, v_2	N/A	N/A	700
NS	1.5×10^{13}	1.0×10^{13}	300
O_2	2.0×10^{17}	4.0×10^{17}	700
OCS	3.0×10^{17}	3.0×10^{15}	700
OD	1.0×10^{14}	1.5×10^{13}	700
OH	3.0×10^{15}	1.5×10^{14}	300
SiS	9.0×10^{14}	6.0×10^{13}	700
SO_2, $v_2 = 2$	N/A	N/A	700
^{33}SO	3.0×10^{13}	1.5×10^{13}	700
^{34}SO	5.0×10^{13}	2.0×10^{13}	300
$^{33}SO_2$	2.0×10^{13}	4.0×10^{13}	300
$^{34}SO_2$	1.5×10^{13}	3.0×10^{13}	200

Table 9
Column Density Upper Limit for Unmodeled Species in Orion-S

Species	$N_{t,T_{\rm ex}=40\ {\rm K}}$	$N_{t,T_{\rm ex}=80\ {\rm K}}$
CH_3OCH_3	1.5×10^{14}	3×10^{14}
CO^+	2×10^{12}	1.5×10^{12}
$H_2^{18}O$	2×10^{12}	3×10^{12}
$HC^{15}N$	1×10^{12}	2×10^{12}
HCS^+	2.5×10^{13}	1×10^{13}
NH_2	7×10^{12}	1×10^{13}
SH^+	4×10^{12}	7×10^{12}
SiO	1×10^{13}	4×10^{12}

SO and SO_2 are often associated with shocked gas, they do not appear in Figure 18. This is because these molecules were optically thick and Crockett et al. (2014) did not provide column densities.

The best agreement with molecular abundances in the narrow component of Orion-S is with the Extended Ridge of Orion-KL (Figure 19), where we obtain $\left\langle \frac{X_{KL}}{X_S} \right\rangle = 7$ (SD = 14). For the broad component (dashed line) we obtain $\left\langle \frac{X_{KL}}{X_S} \right\rangle = 0.3$ (SD = 0.5).

Given that the best match to the abundances in the narrow component of Orion-S is the ER of Orion-KL, it seems as though these species/components do indeed trace quiescent gas. In particular, it probably is the same gas out of which both star-forming regions have been formed. The broad component of Orion-S, however, seems better matched to the CR and Plateau of Orion-KL. Figures 16 to 19 only have a few broad component points and, therefore, it is difficult to make any strong statistical arguments based on these data alone. However, this evidence along with the chemical abundance analysis presented in Section 3.3.1 provide fairly strong support for the idea that shocks have also had an influence on the chemistry of Orion-S.

3.3.3. Species Detected in Orion-KL but Not in Orion-S

It is well known that Orion-KL has an incredibly rich molecular chemistry (e.g., Schilke et al. 1997a; Comito et al. 2005; Tercero et al. 2005; Leurini et al. 2006; Olofsson et al. 2007; Persson et al. 2007). However, it is possible that the species that were detected in Orion-KL, but not in Orion-S, exist in the latter source, but at levels too weak to be detected. Some of these species might be observable with ALMA at lower frequencies. In this section, we explore this possibility by providing upper limits for the abundances of all the species detected in Orion-KL by Crockett et al. (2014) but not detected in Orion-S.

Modeling was accomplished by fixing T_{ex}, ΔV_{FWHM}, Ω, and V_{LSR} and finding the column density that produced transitions for which the intensities were $<3\sigma$ across all the HEXOS bands. Since we were able to model all of our species using, at most, two components, we determine two different column density upper limits: one assuming that the undetected emission arises from the narrow component and assuming that it originates in the broad component. For the narrow component, we used fixed values of $T_{ex} = 40$ K, $\Delta V_{FWHM} = 4$ km s^{-1}, $\Omega = 60''$, and $V_{LSR} = 7.1$, which were found to be typical for the narrow component (see Tables 5 and 6). For the broad component, we used fixed values of $T_{ex} = 80$ K, $\Delta V_{FWHM} = 8$ km s^{-1}, $\Omega = 40''$, and $V_{LSR} = 7.1$, which were found to be typical for the broad component (see Table 6). Results are listed in Table 8. Column 1 is the species name, column 2 is the upper limit total column density assuming the gas arises in the narrow component, column 3 is the upper limit total column density assuming the gas originates in the broad component, and column 4 lists the maximum upper state energy for the model (i.e., no transitions with $E > E_{up}$ were modeled). Different values of E_{up} were used for different molecules to keep the number of modeled transitions to a reasonable value.

There are also a number of species that we detected (S/N $> 3\sigma$) but did not model since their S/Ns were $<5\sigma$. Using the same assumptions as for the undetected species, we provide upper limits for the abundances for these species in Table 9. The column density limits listed in Table 9 are approximately an order of magnitude or more smaller than the column densities of the same species detected in Orion-KL (Crockett et al. 2014).

A possible question is whether the species listed in Table 8 could actually exist in Orion-S even though they are undetected. We inspect the excitation conditions of these species, examining E_{up} of all possible transitions, to determine whether they are detectable given the reported noise of the HIFI bands. A portion of these species have E_{up} much greater than 500 K (e.g., H_2O v_2, $H^{13}CN$ $v_2 = 1$, HC_3N, HC_3N $v = 0$, HCN $v_2 = 1$, HCN $v_2 = 2$, OCS, etc.). Based on the analysis done in this paper, Orion-S can barely excite species with $E_{up} > 500$ K. Therefore, transitions of these species would not be observed above the noise, even if they were present. In addition, there are some complex organic species with transition of $E_{up} < 100$ K which we also did not detect (e.g., CH_2NH, CH_2DOH, CH_2NH, CH_3OCHO, etc.). This is not surprising given the absence of hot-core chemistry in Orion-S.

4. SUMMARY AND CONCLUSION

We have presented results from a comprehensive spectral survey toward Orion South, taken with the HIFI instrument on board the *Herschel Space Observatory* covering the frequency range of 480 to 1900 GHz with a resolution of 1.1 MHz. We detected 685 spectral lines with S/Ns $> 3\sigma$ originating from 52 different molecular and atomic species. Using the CASSIS spectral line analysis software package, we modeled each of the detected species assuming conditions of Local Thermodynamic Equilibrium. Based on this modeling, we found evidence for three different cloud components: a cool ($T_{ex} \sim 20$–40 K), spatially extended ($>60''$), and quiescent ($\Delta V_{FWHM} \sim 4$ km s^{-1}) component; a warmer ($T_{ex} \sim 80$–100 K), less spatially extended ($\sim 30''$), and more dynamic ($\Delta V_{FWHM} \sim 8$ km s^{-1}) component, which is likely affected by embedded outflows; and a kinematically distinct region dominated by emission from species that trace UV irradiation. Indirect evidence to support the existence of the first two components can be inferred from McMullin et al. (1993) who mapped the region in a few spectral lines (SiO, $H^{13}CO^+$, SO_2, CH_3OH, and HC_3N) with the BIMA array. Their $H^{13}CO^+$ and HC_3N data confirm the existence of a fairly extended ($\sim 1'$) quiescent (FWHM ~ 3 km s^{-1}) component, whereas the SO_2 and CH_3OH data reveal a smaller emitting region ($\sim 20''$) of warm gas (~ 75 K). While the spectra for the latter two species are too weak to determine line widths, their SiO data reveal a similarly small region (offset by only a few arc seconds from the SO_2 and CH_3OH emission peaks) with broad-line widths (~ 7 km s^{-1}). In addition, McMullin et al. (1993) reports column densities of SO_2 and $H^{13}CO^+$ of $<2 \times 10^{-10}$ and 4×10^{-11}, respectively, which compare favorably to the values reported in Table 7. Finally, while there are no higher resolution observations to confirm the existence of the third component (i.e., the UV irradiated region), since CO^+ is only ever detected in PDRs, its presence in our data strongly suggests that such a component must exist.

We also presented a comprehensive chemical abundance comparison between Orion-KL and Orion-S; two star-forming regions that potentially formed from the same natal molecular gas but are at different evolutionary stages. Based on a paucity of complex molecules in Orion-S, we found little chemical evidence for the existence of a significant "hot-core"

component. This is likely due to the fact that the hot cores associated with the embedded star formation have either not had sufficient time to develop chemically or are simply too small for their line emission to be detected in the large *Herschel* beam, or Orion-S is not a massive star-forming region and hot cores massive enough to produce their characteristic rich spectra simply do not exist. The presence of a number of UV tracers such as [C II], [C I], CH, CH^+, SH^+, and CO^+, and the fact that transitions of these species have velocities that are 1–1.5 km s^{-1}, higher than those of the quiescent gas, suggest that these species arise from a kinematically distinct PDR; most likely the UV illuminated surface of the cloud. The best match to the chemical abundances in the cooler, quiescent gas in Orion-S is with the quiescent extended ridge of Orion-KL, indicating that most of the gas in Orion-S is still quiescent as well, and relatively unaffected by higher temperature or UV driven chemistry. The best agreement with the warmer, broad component of Orion-S is with the Orion-KL Plateau and Compact Ridge regions, suggesting that shocks have had an influence on the overall chemistry in Orion-S.

HIFI was designed and built by a consortium of institutes and university departments from across Europe, Canada, and the United States under the leadership of the SRON Netherlands Institute for Space Research, Groningen, The Netherlands and with major contributions from Germany, France, and the US. Consortium members are Canada: CSA, U. Waterloo; France: CESR, LAB, LERMA, IRAM; Germany: KOSMA, MPIfR, MPS; Ireland, NUI Maynooth; Italy: ASI, IFSI-INAF, Osservatorio Astrofisico di Arcetri- INAF; Netherlands: SRON, TUD; Poland: CAMK, CBK; Spain: Observatorio Astronmico Nacional (IGN), Centro de Astrobiologa (CSIC-INTA). Sweden: Chalmers University of Technology—MC2, RSS & GARD; Onsala Space Observatory; Swedish National Space Board, Stockholm University—Stockholm Observatory; Switzerland: ETH Zurich, FHNW; USA: Caltech, JPL, NHSC. We also need to acknowledge the support by the Deutsche Forschungsgemeinschaft (DFG) via the collaborative research grant SFB 956, project C1 & C3, as well as the ERC and the Spanish MINECO for funding support under grants ERC-2013-Syg-610256 and AYA2012-32032. Support for this work was provided, in part, by a National Sciences and Engineering Research Council of Canada (NSERC) grant to R. Plume and K. Tahani and by NASA through an award issued by JPL/Caltech. This work was carried out in part at the Jet Propulsion Laboratory, which is operated for NASA by the California Institute of Technology.

Facility: Herschel.

REFERENCES

Anders, E., & Grevesse, N. 1989, GeCoA, 53, 197
Bachiller, R., & Pérez Gutiérrez, M. 1997, ApJL, 487, L93
Bally, J., O'Dell, C. R., & McCaughrean, M. J. 2000, AJ, 119, 2919
Bally, J., & Zinnecker, H. 2005, AJ, 129, 2281
Bergin, E. A., Goldsmith, P. F., Snell, R. L., & Ungerechts, H. 1994, ApJ, 431, 674
Bergin, E. A., Phillips, T. G., Comito, C., et al. 2010, A&A, 521, L20
Beuther, H., Zhang, Q., Greenhill, L. J., et al. 2005, ApJ, 632, 355
Blake, G. A., Sutton, E. C., Masson, C. R., & Phillips, T. G. 1987, ApJ, 315, 621
Ceccarelli, C., Caselli, P., Herbst, E., Tielens, A. G. G. M., & Caux, E. 2007, in Protostars and Planets V, ed. B. Reipurth, D. Jewitt, & K. Keil (Tucson, AZ: Univ. Arizona Press), 47
Ceccarelli, C., Hollenbach, D. J., & Tielens, A. G. G. M. 1996, ApJ, 471, 400
Choi, Y., van der Tak, F. F. S., Bergin, E. A., & Plume, R. 2014, A&A, 572, L10
Comito, C., & Schilke, P. 2002, A&A, 395, 357
Comito, C., Schilke, P., Phillips, T. G., et al. 2005, ApJS, 156, 127
Crockett, N. R., Bergin, E. A., Neill, J. L., et al. 2014, ApJ, 787, 112
Crockett, N. R., Bergin, E. A., Wang, S., et al. 2010, A&A, 521, L21
de Graauw, T., Helmich, F. P., Phillips, T. G., et al. 2010, A&A, 518, L6
Draine, B. T., & Bertoldi, F. 1996, ApJ, 468, 269
Esplugues, G. B., Tercero, B., Cernicharo, J., et al. 2013, A&A, 556, A143
Federman, S. R., Rawlings, J. M. C., Taylor, S. D., & Williams, D. A. 1996, MNRAS, 279, L41
Fuente, A., Martin-Pintado, J., Cernicharo, J., & Bachiller, R. 1993, A&A, 276, 473
Furlan, E., Hartmann, L., Calvet, N., et al. 2006, ApJS, 165, 568
Garrod, R. T., & Herbst, E. 2006, A&A, 457, 927
Garrod, R. T., Weaver, S. L. W., & Herbst, E. 2008, ApJ, 682, 283
Gerin, M., de Luca, M., Goicoechea, J. R., et al. 2010, A&A, 521, L16
Godard, B., Falgarone, E., Gerin, M., et al. 2012, A&A, 540, A87
Goicoechea, J. R., Teyssier, D., Etxaluze, M., et al. 2015, ApJ, 812, 75
Goldsmith, P. F., Bergin, E. A., & Lis, D. C. 1997, ApJ, 491, 615
Goldsmith, P. F., & Langer, W. D. 1978, ApJ, 222, 881
Groesbeck, T. D. 1995, PhD thesis, California Institute of Technology
Guan, Y., & Krone, S. M. 2007, arXiv:math/0703021
Gusdorf, A., Cabrit, S., Flower, D. R., & Pineau Des Forêts, G. 2008a, A&A, 482, 809
Gusdorf, A., Pineau Des Forêts, G., Cabrit, S., & Flower, D. R. 2008b, A&A, 490, 695
Hastings, W. K. 1970, ArRMA, 38, 308
Herbst, E., & van Dishoeck, E. F. 2009, ARA&A, 47, 427
Herrmann, F., Madden, S. C., Nikola, T., et al. 1997, ApJ, 481, 343
Hollenbach, D. J., & Tielens, A. G. G. M. 1997, ARA&A, 35, 179
Iglesias, E. R., & Silk, J. 1978, ApJ, 226, 851
Kama, M., López-Sepulcre, A., Dominik, C., et al. 2013, A&A, 556, A57
Kaźmierczak-Barthel, M., Semenov, D. A., van der Tak, F. F. S., Chavarría, L., & van der Wiel, M. H. D. 2015, A&A, 574, A71
Kurtz, S., Cesaroni, R., Churchwell, E., Hofner, P., & Walmsley, C. M. 2000, in Protostars and Planets IV, ed. V. Mannings, A. Boss, & S. Russell (Tucson: Univ. Arizona Press), 299
Ladd, E. F. 2004, ApJ, 610, 320
Langer, W. D., Velusamy, T., Pineda, J. L., et al. 2010, A&A, 521, L17
Leurini, S., Rolffs, R., Thorwirth, S., et al. 2006, A&A, 454, L47
Lucas, R., & Liszt, H. 1998, A&A, 337, 246
Mangum, J. G., & Wootten, A. 1993, ApJS, 89, 123
Mangum, J. G., Wootten, A., & Plambeck, R. L. 1993, ApJ, 409, 282
Martin-Pintado, J., Bachiller, R., & Fuente, A. 1992, A&A, 254, 315
McMullin, J. P., Mundy, L. G., & Blake, G. A. 1993, ApJ, 405, 599
Menten, K. M., Reid, M. J., Forbrich, J., & Brunthaler, A. 2007, A&A, 474, 515
Menten, K. M., & Wyrowski, F. 2011, STMP, 241, 27
Mezger, P. G., Zylka, R., & Wink, J. E. 1990, A&A, 228, 95
Millar, T. J., & Herbst, E. 1990, A&A, 231, 466
Mookerjea, B., Ossenkopf, V., Ricken, O., et al. 2012, A&A, 542, L17
Müeller, M., Jellema, W., Olberg, M., Moreno, R., & Teyssier, D. 2014, The HIFI Beam: Release #1 Release Note for Astromers, 1.1, 1 (http://herschel.esac.esa.int/twiki/pub/Public/HifiCalibrationWeb/HifiBeamReleaseNote_Sep2014.pdf)
Müller, H. S. P., Schlöder, F., Stutzki, J., & Winnewisser, G. 2005, JMoSt, 742, 215
Nagy, Z., Ossenkopf, V., Van der Tak, F. F. S., et al. 2015, A&A, 578, A124
Nagy, Z., Van der Tak, F. F. S., Ossenkopf, V., et al. 2013, A&A, 550, A96
Neill, J. L., Bergin, E. A., Lis, D. C., et al. 2014, ApJ, 789, 8
Nummelin, A., Bergman, P., Hjalmarson, Å., et al. 1998, ApJS, 117, 427
O'Dell, C. R., & Harris, J. A. 2010, AJ, 140, 985
Olofsson, A. O. H., Persson, C. M., Koning, N., et al. 2007, A&A, 476, 791
Ott, S. 2010, in ASP Conf. Ser. 434, Astronomical Data Analysis Software and Systems XIX, ed. Y. Mizumoto, K.-I. Morita, & M. Ohishi (San Francisco, CA: ASP), 139
Pan, K., Federman, S. R., & Welty, D. E. 2001, ApJL, 558, L105
Papadopoulos, P. P., Thi, W.-F., & Viti, S. 2004, MNRAS, 351, 147
Parise, B., Leurini, S., Schilke, P., et al. 2009, A&A, 508, 737
Pearson, J. C., Drouin, B. J., & Pickett, H. M. 2005, in IAU Symp. 235, Galaxy Evolution across the Hubble Time, ed. F. Combes & J. Palous (New York: Cambridge Univ. Press), 270
Persson, C. M., Olofsson, A. O. H., Koning, N., et al. 2007, A&A, 476, 807

Pilbratt, G. L., Riedinger, J. R., Passvogel, T., et al. 2010, A&A, 518, L1
Plume, R., Bergin, E. A., Phillips, T. G., et al. 2012, ApJ, 744, 28
Plume, R., Jaffe, D. T., & Evans, N. J., II 1992, ApJS, 78, 505
Plume, R., Jaffe, D. T., Tatematsu, K., Evans, N. J., II, & Keene, J. 1999, ApJ, 512, 768
Porter, J. M., Oudmaijer, R. D., & Baines, D. 2004, A&A, 428, 327
Roberts, G. O., Gelman, A., & Gilks, W. R. 1997, The Annals of Applied Probability, 7, 110
Roelfsema, P. R., Helmich, F. P., Teyssier, D., et al. 2012, A&A, 537, 17
Schilke, P., Benford, D. J., Hunter, T. R., Lis, D. C., & Phillips, T. G. 2001, ApJS, 132, 281
Schilke, P., Groesbeck, T. D., Blake, G. A., & Phillips, T. G. 1997a, ApJS, 108, 301
Schilke, P., Walmsley, C. M., Pineau des Forets, G., & Flower, D. R. 1997b, A&A, 321, 293
Schmid-Burgk, J., Guesten, R., Mauersberger, R., Schulz, A., & Wilson, T. L. 1990, ApJL, 362, L25
Shetty, R., Kauffmann, J., Schnee, S., Goodman, A. A., & Ercolano, B. 2009, ApJ, 696, 2234
Tauber, J. A., & Goldsmith, P. F. 1990, ApJL, 356, L63
Tercero, B., Cernicharo, J., & Pardo, J. R. 2005, in IAU Symp. 235, 203
Tercero, B., Cernicharo, J., Pardo, J. R., & Goicoechea, J. R. 2010, A&A, 517, A96
Tielens, A. G. G. M., & Hollenbach, D. 1985, Icar, 61, 40
van der Tak, F. F. S., Black, J. H., Schöier, F. L., Jansen, D. J., & van Dishoeck, E. F. 2007, A&A, 468, 627
Velusamy, T., Langer, W. D., Pineda, J. L., & Goldsmith, P. F. 2012, A&A, 541, L10
Wang, S., Bergin, E. A., Crockett, N. R., et al. 2011, A&A, 527, 95
Watson, W. D., & Walmsley, C. M. 1982, in Regions of Recent Star Formation, ed. R. S. Roger & P. E. Dewdney (Dordrecht: Reidel, Holland), 357
Williams, J. P., Bergin, E. A., Caselli, P., Myers, P. C., & Plume, R. 1998, ApJ, 503, 689
Wootten, A., Bozyan, E. P., Garrett, D. B., Loren, R. B., & Snell, R. L. 1980, ApJ, 239, 844
Zapata, L. A., Ho, P. T. P., Rodríguez, L. F., et al. 2006, ApJ, 653, 398
Zapata, L. A., Rodríguez, L. F., Ho, P. T. P., et al. 2005, ApJL, 630, L85
Zapata, L. A., Schmid-Burgk, J., & Menten, K. M. 2011, A&A, 529, A24
Zernickel, A., Schilke, P., Schmiedeke, A., et al. 2012, A&A, 546, A87
Ziurys, L. M., Wilson, T. L., & Mauersberger, R. 1990, ApJL, 356, L25